University of California
Santa Barbara

Cavity Polarization Tuning for Enhanced Quantum Dot Interactions

A dissertation submitted in partial satisfaction
of the requirements for the degree

Doctor of Philosophy
in
Physics

by

Johnathon Andrew Frey

Committee in charge:

Professor Dirk Bouwmeester, Chair
Professor Cenke Xu
Professor John Bowers

December 2019

The Dissertation of Johnathon Andrew Frey is approved.

Professor Cenke Xu

Professor John Bowers

Professor Dirk Bouwmeester, Committee Chair

December 2019

Cavity Polarization Tuning for Enhanced Quantum Dot Interactions

by

Johnathon Andrew Frey

Acknowledgements

There are many people whom I would like to thank. First, I would be nowhere without the support of my advisors. Dirk Bouwmeester has been my primary advisor throughout graduate school. He has continually supported me, even though at times there were doubts about finishing the PhD. I have gained a wealth of knowledge as a result, and I believe it will help me in the future. Wolfgang Löffler has played a role of an advisor on a closer level than that of a principal investigator. He has been crucial in the development of my own laboratory skills. Most important I think, he has taught me how to maintain an extreme level of rigor, which is necessary for scientific work. I must further thank Jesse Berezovsky, who was the first to introduce me to physics research. I would not have succeeded without the skills I developed in his lab at Case Western, and my research interests are still partly shaped by my experience there.

I am fortunate to have been able to work alongside some very talented people in Santa Barbara and Leiden. In particular, Henk Snijders has been the primary student in Leiden on the quantum dot project during my stay. If not for him, many of our results would not have happened. I have learned a great amount from his work. Justin Norman has been the grower in Santa Barbara, and he has worked tirelessly on the epitaxy machines to produce quality material. As the machines are not always well-behaved, this is a challenging task. In addition to those directly working on my project, I would like to thank my other colleagues in the group who have made the experience enjoyable, and have been able to help on occasion with related problems. In no particular order, they are: Eric Langman, Matthew Weaver, Joe Swearngin, and Fernando Luna.

A number of undergraduates have worked with me in the lab, and they have been critical in my understanding and development of my devices. I would like to thank Aaron Kerr, Benton Miller, Danielle Woods, Joey Bush, and Ian Hedgepeth. In addition

to helping me expand my knowledge, they have brought joy and motivation to the lab, and I wish them the best of luck as they begin their scientific careers.

I have spent a lot of time in the UCSB cleanroom. The cleanroom work generally has a big learning curve, and things rarely work on first attempts. I have the entire cleanroom staff and community to thank for my success. I have been able to function well, realizing I am in an environment where there is always someone around you who knows something you don't, and that those people are generally willing to share their knowledge. The staff at UCSB are extremely hard-working and knowledgeable. I want to thank, in particular, Brian Thibeault and Demis John for their support in developing good process recipes. Amongst the other staff members, Tony Bosch has been extremely helpful. I have interacted with him a lot, especially with the oxidation process.

Personally, there are many people whom I would like to thank for helping me get through this program. Those I have lived with for five years in the same house, Kevin, Blake, James, Nikita, Rohan, and Toshi, have all made life enjoyable, and I would not have finished without them. The last half year with Emily and Chris has been very enjoyable as well. I have been a member of the UCSB Triathlon Team for six years. This group has been critical in keeping me sane throughout the program. Triathlon has been my primary escape from graduate school. There are too many people to list here, but I am thankful for all of them who have helped me throughout my stay. I am happy to move on from UCSB, not only with my professional development, but also with what I have gained from triathlon.

Curriculum Vitæ

Johnathon Andrew Frey

Education

2019	Ph.D. in Physics (Expected), University of California, Santa Barbara.
2016	M.A. in Physics, University of California, Santa Barbara.
2013	B.S.E. in Engineering Physics, Case Western Reserve University.

Publications

H. J. Snijders, D. N. L. Kok, M. F. van de Stolpe, J. A. Frey, J. Norman, A. C. Gossard, J. E. Bowers, M. P. van Exter, D. Bouwmeester, and W. Löffler, *Polarized quantum dot cavity-QED and single photons, arXiv*:1811.1057 (2018).

J. A. Frey, H. J. Snijders, J. Norman, A. C. Gossard, J. E. Bowers, W. Löffler, and D. Bouwmeester, *Electro-optic polarization tuning of microcavities with a single quantum dot, Optics Letters* **43** 4280 (2018).

H. J. Snijders, J. A. Frey, J. Norman, H. Flayac, V. Savona, A. C. Gossard, J. E. Bowers, M. P. van Exter, D. Bouwmeester, and W. Löffler, *Observation of the Unconventional Photon Blockade, Physical Review Letters* **121** 043601 (2018).

H. J. Snijders, J. A. Frey, J. Norman, V. Post, A. C. Gossard, J. E. Bowers, M. P. van Exter, W. Löffler, and D. Bouwmeester, *Fiber-Coupled Cavity-QED Source of Identical Single Photons, Physical Review Applied* **9** 031002 (2018).

H. J. Snijders, J. A. Frey, J. Norman, M. P. Bakker, E. C. Langman, A. C. Gossard, J. E. Bowers, M. P. van Exter, D. Bouwmeester, and W. Löffler, *Purification of a single-photon nonlinearity, Nature Communications* **7** 12578 (2016).

R. Badea, J. A. Frey, and J. Berezovsky, *Magneto-optical imaging of vortex domain deformation in pinning sites, Journal of Magnetism and Magnetic Materials* **381** 463 (2015).

J. A. Frey and J. Berezovsky, *Frequency-domain optical probing of coherent spins in nanocrystal quantum dots, Optics Express* **20** 20011 (2012).

Abstract

Cavity Polarization Tuning for Enhanced Quantum Dot Interactions

by

Johnathon Andrew Frey

Cavity enhanced interactions of light and matter have promising applications in quantum information technology. In particular, semiconductor quantum dots are extremely good candidates for single photon sources. Quantum dots have strong optical properties and can be directly embedded into photonic devices. Micropillar cavities with embedded quantum dots can be grown and fabricated, all with the use of mature semiconductor technology. Typically, microcavities are fabricated with a finite polarization mode splitting. Such splitting is detrimental in most applications, including the generation of single photons. The mechanisms that produce birefringence in semiconductor micropillar cavities are discussed in detail, and methods to eliminate such effects are discussed. A fine tuning method is presented, which is used to independently tune the cavity polarization splitting and quantum dot resonance. The fine tuning method makes use of the linear electro-optic effect to alter the birefringence of a single mirror. With high resolution reflection spectroscopy, the dynamics of a quantum dot in a polarization degenerate cavity are studied. Interactions are discussed, both in the context of classical, and quantum mechanical interactions.

Contents

Chapter 1

Introduction

1.1 Motivation

The field of quantum optics has proven to be an immensely rich field within physics. Part of the reason it is so powerful is that the amount of energy of a single photon at optical frequencies, described as a quantum excitation of a harmonic oscillator, is much greater than $k_b T$ at room temperature. Therefore, experiments are hardly affected by thermal excitations. Further, photons do not interact with themselves, and interact weakly with matter. Therefore, they exhibit extremely long lifetimes.

Fundamental tests of quantum mechanics have been conducted using photons. Among the most notable is the violation of Bell's inequalities in Einstein-Podolsky-Rosen types of experiments. Such experiments have been performed with polarization entangled photons, both from atomic cascades [1, 2, 3], and spontaneous parametric down-conversion [4, 5]. In recent years, the prospect of quantum computing and quantum communication based on photonic systems has led to a huge research effort [6].

Due to the fact that photons interact with their environment so weakly, they do not suffer from decoherence. This property makes photons good candidates for qubits. The

downside of their non-interacting nature is that it is difficult to build photonic quantum gates. The difficulty in forcing photons to interact has been the major roadblock to photonic quantum computing. However, breakthroughs have been achieved, which suggest linear optics as a viable path to quantum computing. In particular, the Knill, Laflamme, and Milburn, KLM, scheme showed that quantum gates can be implemented with *single photon sources* using linear optics and single photon detectors [7]. The scheme essentially relegates the strong optical non-linearities needed to perform quantum computation to the sources and detectors. Raussendorf and Briegel, around the same time, proposed a "one-way quantum computer" [8]. Initially not proposed for photonic circuits, the proposal suggested the use of multi-qubit entangled states called cluster states. With the initial state prepared, computation is performed by single particle measurements. The cluster state proposal was further extended to the photonics platform and suggested to reduce the resource overhead of the original KLM scheme [9].

Rudolph published an extremely optimistic article on the state of photonic quantum computation using silicon based photonic circuits [10]. The technology of silicon photonics is in a very mature state. Low-loss silicon nitride circuits have been implemented with over 20 integrated Mach-Zehnder interferometers per square cm [11]. Integrated photonic circuits have been developed, for example, demonstrating quantum transport simulations [12], and simulations on molecular dynamics [13]. Additional reviews on quantum information processing with integrated photonic circuits can be found in References [14, 15]. Single photon detectors, based on superconducting nanowires, have further been developed to detect photons with $> 90\%$ efficiency [16, 17].

Much of the work in photonic quantum information has been performed with down-converted photons. There are, however, downsides to the method, which has motivated the effort to find new single photon sources. As it is inherently a non-linear process, the brightness depends on the intensity of the exciting light. The incident power can be

increased to observe more frequent events. However, higher order terms in the down-conversion process become non-negligible with increasing power, limiting the purity of the source. It has been argued that multi-photon emission events are the primary limiting factor in photonic quantum computing [18].

The work detailed in this thesis concerns the generation of quantum states of light, generated from quantum dots in micropillar cavities. Quantum dots have been studied intensively for their optical properties, and ability to be directly embedded into photonic devices. Their optical properties are a direct consequence of quantum confinement. The ubiquitous phenomenon has important consequences in many applications. Behaving as single *artificial atoms*, quantum dots have provided a new, and technologically critical, platform for physics previously relegated to atomic systems. Light from a single quantum dot is inherently quantum, producing only one photon per lifetime of its excited state. This aspect has motivated work on using quantum dots as single photon sources. In a quantum dot, a single photon can be created on demand in a single cavity mode. The probability of creating two or more photons is greatly reduced compared to down conversion.

1.2 Overview of Single Photon Sources

Antibunching is observed by performing a Hanbury-Brown Twiss experiment, where photons are incident on a beam splitter and time correlations of photon detections on both output ports are recorded. Antibunched light will produce zero coincidence events when there is zero time delay between detectors. Observing antibunching in a Hanbury-Brown Twiss experiment has historically been challenging due to the relatively low photon counts in such an experiment. Because photonic interactions with matter are relatively weak, detecting photons from a single emitter is a challenging task. Detectors with good

quantum efficiency, as well as efficient means to excite and collect light are needed. The desired light must also be sufficiently filtered from stray sources of background light. Collection efficiency is greatly improved by embedding the emitter inside a cavity. Cavities also provide a means to increase the interaction strength with an exciting light field. In a cavity, photons make multiple round trips, and effectively increase the absorption cross section of the emitter [19].

Antibunching in resonance fluorescence has been observed since the experiments with cold atoms performed by Kimble et. al. [20], and improved by Short and Mandel [21]. In a landmark experiment, Sodium atoms were excited on resonance with an atomic transition, and the light was collected with optics, which collect perpendicular to the excitation beam. The collected photons were sent to a Hanbury-Brown Twiss setup, which revealed significant antibunching. Two key aspects of the experiment performed by Kimble are: atoms are excited resonantly, and there is a method to properly filter the excitation light from the photons emitted from the atom. Antibunching stems from the fact that the cavity contains only one atom at a time. A second order correlation function, $g^{(2)}(t)$, quantifying the amount of antibunching, down to 0.5 was measured. At zero time, $g^{(2)}(0) < 1$ is evidence of antibunched light.

This thesis is focused on correlated photons from cavity-enhanced quantum dots. The advances in epitaxy, controlled monolayer growth of crystalline material, have enabled the growth of extremely high quality semiconductor heterostructures. The field of quantum optics has, therefore, been able to expand into the realm of integrated photonics. By isolating a single quantum dot, antibunching can be observed. Making use of the surrounding semiconductor, excitation is perhaps most easily done by electrically injecting carriers into the dot. Electrical injection has been performed on isolated quantum dots [22], and for quantum dots enhanced in optical microcavities [23]. One can also use non-resonant optical excitation, first performed by the Yamamoto group without [24],

and with a microcavity [25], and by Michler et. al. in a microdisk [26]. A single photon source with an oxide-aperture microcavity, following closely the technology of vertical emitting lasers, was demonstrated by Strauf et. al. [27]. Micropillar oxide-aperture cavities are used throughout this thesis.

With electrical and non-resonant excitation methods, background light is well separated from the quantum dot light. Isolating a single dot, and increasing collection efficiency, can be achieved with various levels of processing. Microcavities can be fabricated around a quantum dot, which enhance the interaction strength with the cavity field. Resonant experiments, though, are much harder to perform because spectral filtering is not available. Isolation of the quantum dot light in resonance fluorescence experiments can be done by exciting through the side of a device [28, 29]. Fluorescence is then collected in a separate optical mode than the mode of the exciting light.

Besides filtering through a separate spatial mode, polarization is the most standard method of filtering light from resonantly excited quantum dots. Typically, a linearly polarized excitation beam is used to excite the system. A polarizer, which is crossed 90° with the incident light, must be used to extinguish the exciting light. Polarization rotated light, induced by a quantum dot, is allowed through the polarizer. Neutral quantum dots always exhibit some degree of fine structure splitting between linearly polarized transitions [30]. Therefore, the polarization of incident linearly polarized light can be rotated if it is not perfectly aligned with one of the quantum dot axes.

Resonant excitation provides the cleanest method of exciting a quantum dot. As the excitation light is further off resonance, the carriers need more pathways to relax to the quantum dot ground state. The relaxation process introduces timing jitter. Additional power needed for excitation will lead to more carriers around the dot. The extra carriers introduce charge noise and spectral diffusion. Therefore, non-resonant excitation is undesirable for producing subsequent *indistinguishable* photons.

The introduction of microcavities leads to the field of cavity quantum electrodynamics. Microcavities can be fabricated well enough to observe Purcell enhancement, where the excited state emission rate increases. The strong coupling regime is obtained in the case that the coupling strength to a single emitter is much greater than the cavity decay and excited state decay rates. The regime is described by coherent interactions of emitted photons, which stay in the cavity long enough to interact with the emitter multiple times. The states of the system in the strong coupling regime are described by polaritons.

The photon blockade method provides a promising avenue towards reliable single photon sources. The polariton splitting in the strong coupling regime displays a non-linear dependence on the number of photons, allowing only single photon transitions to be transmitted. The photon blockade effect was first demonstrated in an atomic system with optically cooled Caesium [31, 32], and repeated with quantum dots in photonic crystals [33]. A cross polarization method is still typically used for these experiments, and the method relies strictly on the strong coupling regime to be effective. For semiconductor systems, strong coupling with a microcavity is extremely difficult to achieve. It is still possible, with perfect in-coupling to the cavity, for the cavity itself to spatially filter all excitation light [34]. However, this method is also extremely demanding.

A perfect single photon source is defined by its ability to produce one, and only one, photon in a well defined temporal and spatial mode. The purity, usually described by the second order correlation function, should be zero for zero time delay, i.e. $g^{(2)}(0) = 0$. Quantum information applications, further, greatly rely on the production of indistinguishable photons. A number of systems have been developed for single photon generation [35]. Most rely on the use of non-resonant excitation, or resonant excitation with a post-selection polarizer. In elliptical cavities, resonant excitation without a polarizer has been demonstrated, but this method sacrifices the ability to choose, arbitrarily, the excitation angle [14].

1.3 Microcavity Quantum Dot Single Photon Sources

The system presented in this thesis is a single quantum dot coupled to a microcavity. Longitudinal confinement of the cavity is provided by two distributed Bragg reflectors (DBRs), and transverse confinement is provided by an oxide aperture. The device is shown schematically in Figure 1.1. Figure 1.1 (a) shows the experimental procedure for producing single photons. Resonant excitation and emission of photons from the quantum dot results in antibunched light. The incident light is polarized at the input. In order to filter the resonant excitation beam, a polarizer at the output, oriented 90° with the incident light, is used. Photons, which are rotated by the quantum dot, are allowed through the back polarizer.

Figure 1.1 (b) is a schematic of the microcavity device. The two DBR mirrors form a planar Fabry-Perot cavity. Embedded in the cavity region is an oxide aperture, which confines the light field in the transverse direction. Contact layers, represented by green and red, provide electrical control of the quantum dot energy. The contact layers are embedded in the device around the cavity region. Isolated mesas must either be contacted from the top and bottom of the device directly, or through subsequent processing steps, which route wires to a bonding pad on the device. Etched *vias*, or trenches, allow convenient electrical access to the microcavity region. Figure 1.1 (c) is a microscope image of a fabricated device. The open mesa design provides electrical channels to the cavity without directly contacting the mesa. With this design, multiple cavities can be fabricated in an array, which can all be contacted with one bonding pad. A scanning electron microscope (SEM) image of a cavity is included showing the etched trenches, which expose the oxide layer.

The lifetime of an excited state in an atom or quantum dot is typically calculated

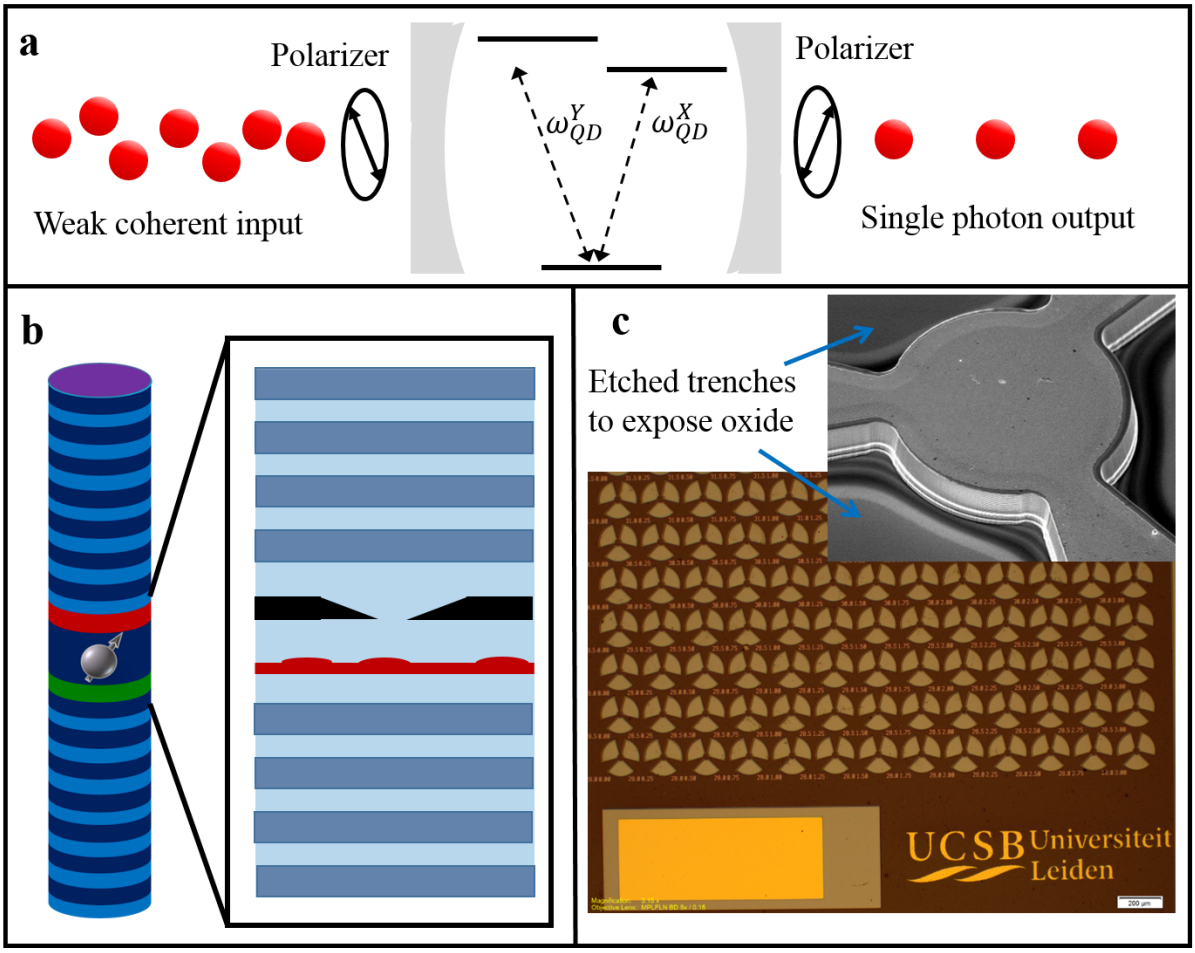

Figure 1.1: Overview of the microcavity-quantum dot device. Resonant excitation with pre and post-selection is shown in (a). Quantum dot induced polarization rotations produce antibunched light on the output of the back polarizer when crossed 90° with the incident polarization. In (b), a schematic device is shown. Two DBRs form a planar Fabry-Perot. The n and p-doped contact layers are embedded near the cavity region. The zoom in shows the oxide aperture and layer of quantum dots. An array of cavities, with a three fold open cavity design, is shown in (c), along with an SEM image of a single cavity.

through first order perturbation theory with the electric dipole approximation [36]. The inclusion of the emitter in an optical cavity modifies the optical density of states, and the transition rate is modified. The effect was first described by Purcell [37]. For a transition on resonance with a cavity of mode volume, V, and quality factor, Q, the lifetime is reduced by

$$F = \frac{3Q\lambda^3\epsilon_0}{4\pi^2 V\epsilon_M}. \tag{1.1}$$

F is called the Purcell factor. λ is the wavelength of the light, ϵ_0 is the free space dielectric constant, and ϵ_M is the dielectric constant of the material. Lifetime measurements revealing Purcell enhancement of quantum dot emission were first performed by Gerard et. al. [38]. Measurements on dots outside of cavities reveal that the lifetime is strongly dependent on the charge state, and exhibits variation according to the size of the dot [39, 40, 41]. For neutral dots, lifetimes of $\sim$1 ns are typical, and Purcell factors close to $\sim$10 with state of the art microcavity fabrication can be observed. Charge noise, spin noise, and magnetic noise can introduce pure dephasing [42, 43].

1.4 Polarization Entanglement and Other Methods

The work in this thesis is centered around neutral exciton transitions. Different mechanisms exist in quantum dots, which are profoundly important for photonic quantum information. Such details go beyond the scope of this work. Nevertheless, a brief overview of important processes is given.

Through the bi-exciton decay of a quantum dot, polarization entangled photons can be obtained directly [44, 45]. The Coulomb repulsion between the single and bi-exciton splits the two emissions in energy. The energy difference is useful, providing a relatively strong virtual state for resonant two photon absorption to the bi-exciton state [46, 47].

The emission cascade, then, proceeds through the single exciton. The energy of the exciting state can be filtered spectrally. So long as the fine structure splitting of the single exciton is small, the cascade process produces polarization entangled photons.

The Coulomb repulsion presents an additional challenge for fabricating microcavities, as would be necessary to use the bi-exciton as a deterministic entangled photon source. A cavity must be bi-modal to support the two emission energies of the cascaded photons. It is possible to fabricate high quality bi-modal cavities, but fine tuning two quantum dot resonances to each mode is a challenge. Advances towards cavity enhanced bi-exciton generation include coupled micropillar cavities [48] and circular Bragg gratings [49].

Two photon absorption and emission using the single exciton has been proposed [50]. Two photon process from the single exciton provide the benefit of being able to select the virtual state, through which one photon decays, with the cavity alone. Spectral filtering can isolate the exciting light. The cross section of these transitions is extremely small, and without additional symmetry breaking mechanisms like an applied electric field, the optical selection rules do not allow two photon transitions. To date this method has not yet been successfully implemented.

A different two color excitation scheme has been developed where a chirped pulse is split into two pulses, which average but do not overlap the resonance frequency of the cavity-quantum dot system [51]. The method, again, enables spectral filtering of resonantly excited dot light. To implement the scheme, though, the quality factor of the cavity is kept relatively low compared to state of the art cavities.

1.5 Outline of Thesis

The thesis is organized as follows. In Chapter 2 the necessary principles in quantum optics are outlined, from second quantization of the electromagnetic field to the

Jaynes-Cummings Hamiltonian. Discussion of antibunching and two-photon interference is included, with results from our quantum dot-cavity system. The properties of the quantum dot devices, which are grown by the Bowers group at the UCSB epitaxy lab, are discussed in Chapter 3, as well as measurements of single quantum dots via micro-photoluminescence and reflection spectroscopy. The primary contributions of this thesis are from the fabrication of polarization degenerate microcavities. Chapter 4 discusses the design and fabrication of the microcavities. The issues of birefringence and cavity polarization mode splitting, which must be overcome, are detailed in this chapter. Restoration of polarization mode splitting via an electro-optic tuning method is presented in Chapter 5. Chapter 6 presents quantum optics phenomena, which are studied using polarization degenerate, or near polarization degenerate cavities. The results in this chapter are the result of a close collaboration with the quantum optics group at Leiden University. Two results are presented: strongly correlated photons, and Unconventional Photon Blockade.

Chapter 2

Quantum Optics

In this chapter, the relevant topics within quantum optics are briefly presented. First, the second quantization of electromagnetic waves is introduced, followed by a discussion of quantum coherence functions and coherent states of radiation. Next, quantum interference at a beam splitter is introduced, which is an important property for quantum computing with linear optics. Finally, the complete quantum description of interactions of a quantum dot (or a general two level system) with light in an optical cavity, i. e. the Jaynes-Cummings model, is explained. The discussion includes results with and without dissipative interactions. Many textbooks cover the topics presented. In particular, the textbook by Gerry and Knight is closely followed here [52].

2.1 Quantum States of Light

Second quantization of the electromagnetic field follows from identifying the quantum harmonic oscillator, described by the Hamiltonian,

$$\hat{H} = \frac{1}{2}\left(\hat{p}^2 + \omega^2 \hat{q}^2\right), \tag{2.1}$$

with a single optical mode of the radiation field. The operators $\hat{q}$ and $\hat{p}$ are related to the integrated energy associated with electric and magnetic fields in the mode. In terms of creation, $\hat{a}^\dagger$, and annihilation, $\hat{a}$ operators, the harmonic oscillator Hamiltonian takes the form

$$\hat{H} = \hbar\omega \left(\hat{a}^\dagger \hat{a} + \frac{1}{2} \right), \tag{2.2}$$

and the operators, $\hat{a}^\dagger$ and $\hat{a}$ satisfy the commutation relation $\left[\hat{a},\, \hat{a}^\dagger\right] = 1$.

The eigenstates of the Hamiltonian in Equation 2.2 are photon number states, $|n\rangle$, or Fock states. The operator $\hat{a}^\dagger\hat{a}$ is called the number operator, and its eigenvalues are the number of photons, n, in the field. The action of $\hat{a}^\dagger$ and $\hat{a}$ on an arbitrary state are given by $\hat{a}\,|n\rangle = \sqrt{n}\,|n-1\rangle$, and $\hat{a}^\dagger\,|n\rangle = \sqrt{n+1}\,|n+1\rangle$. For a single optical mode, the states $|n\rangle$ form a complete orthonormal basis. It turns out pure number states are extremely non-classical. General states are given by a superposition of number states.

2.2 Second Order Coherence

In an average measurement of power, such as that of a standard photodiode, only an average rate of photon events is recorded. The information on photon statistics must be revealed through measurements of the correlation functions. The theory of photon coherent states and quantum correlation functions can be mainly attributed to the work of Glauber [53, 54], who sought out a quantum formulation of optics in terms of correlations of photon measurements in different spatial or temporal modes. The work of Hanbury-Brown and Twiss, was the first to present an experiment, which measures correlations in intensity, or photon numbers [55, 56].

The normalized second order correlation function, $g^2(\tau)$, is defined as

$$g^{(2)}(\tau) = \frac{\langle I(t)\, I(t+\tau)\rangle}{\langle I(t)\rangle^2}, \tag{2.3}$$

where $I(t)$ and $I(t+\tau)$ are intensities at times t and $t+\tau$. To derive a quantum mechanical formulation of Equation 2.3, the electric field can be separated into its positive and negative frequency components, E^+ and E^-, corresponding to absorption and emission processes. These are directly related to the operators $\hat{a}^\dagger$ and $\hat{a}$. Information on the field is only obtained through measurements, which destroy the state. Glauber noted that the action of a perfect photodetector is represented only by the positive frequency component of the field, or $\hat{a}$, which alone is not Hermitian. The photodetector, after absorbing a photon from the field, makes a transition from one state to another, and is assumed to be immediately read out and reset to its initial state.

Correlations in time are of primary interest here, although the theory is applicable to both spatial and time correlations. The rate of coincidences on two detectors, which detect photons at times t and $t+\tau$, is

$$G^{(2)}(t, t+\tau) = \left\langle E^-(t)\, E^-(t+\tau)\, E^+(t+\tau)\, E^+(t)\right\rangle, \tag{2.4}$$

which is normalized according to

$$g^{(2)}(t, t+\tau) = \frac{\langle E^-(t)\, E^-(t+\tau)\, E^+(t+\tau)\, E^+(t)\rangle}{\langle E^-(t)\, E^+(t)\rangle \langle E^-(t+\tau)\, E^+(t+\tau)\rangle} \tag{2.5}$$

A field is second order coherent if $g^{(2)}(t, t+\tau) = 1$.

A single mode traveling wave, retaining only the time dependence, is written as

$$E = E^+ + E^- = i\sqrt{\frac{\hbar\omega}{2\epsilon_0 V}}\left(\hat{a}e^{-i\omega t} + \hat{a}^\dagger e^{+i\omega t}\right), \tag{2.6}$$

where ω is the frequency of the light, ϵ_0 is the free space dielectric constant, and V is the mode volume. Equation 2.5 can be evaluated for the single mode field of Equation 2.6, and yields

$$g^{(2)}(\tau) = 1 + \frac{\left\langle (\Delta\hat{n})^2 \right\rangle - \langle \hat{n} \rangle}{\langle \hat{n} \rangle^2}. \tag{2.7}$$

The notation is simplified on the left hand side. The result shows that for a single mode field, the second order correlation function must be independent of time. If it happens that $\left\langle (\Delta\hat{n})^2 \right\rangle < \langle \hat{n} \rangle$, then $g^{(2)}(\tau) < 1$, which is evident of sub-Poissanian statistics. Such is a completely quantum phenomenon. It can be shown further that multimode and thermal fields take on a values in the range $1 < g^{(2)}(\tau) < 2$ [52].

From Equation 2.5, it is evident that one way of defining a field to be completely second order coherent is by requiring the numerator factorize according to

$$\left\langle E^-(t) E^-(t+\tau) E^+(t+\tau) E^+(t) \right\rangle = \left\langle E^-(t) E^+(t) \right\rangle \left\langle E^-(t+\tau) E^+(t+\tau) \right\rangle. \tag{2.8}$$

This condition is exactly satisfied for eigenstates of the annihilation operator, $\hat{a}$. Definite eigenstates exist for $\hat{a}$ with complex eigenvalues, as $\hat{a}$ is not Hermitian. The solution to the eigenvalue problem, $\hat{a}|\Psi\rangle = \alpha|\Psi\rangle$, is given by

$$|\Psi\rangle = \exp\left(-\frac{1}{2}|\alpha|^2\right) \sum_{n=0}^{\infty} \frac{\alpha^n}{\sqrt{n!}} |n\rangle. \tag{2.9}$$

It can be shown that the quantity $|\alpha|^2$ is the mean photon number of the field. Taking the expectation value of the photon number operator $\hat{n} = \hat{a}^\dagger \hat{a}$, the mean photon number can be evaluated

$$\langle \Psi | \hat{n} | \Psi \rangle = \exp\left(-|\alpha|^2\right) \sum_{n=1}^{\infty} \frac{|\alpha|^{2n}}{(n-1)!} = \exp\left(-|\alpha|^2\right) |\alpha|^2 \sum_{n=0}^{\infty} \frac{|\alpha|^{2n}}{n!}. \tag{2.10}$$

With the definition of the exponential, Equation 2.10 becomes

$$\langle \Psi \left| \hat{n} \right| \Psi \rangle = |\alpha|^2 . \tag{2.11}$$

The variance, $\Delta n^2 = \langle \Psi \left| \hat{n}^2 \right| \Psi \rangle$-$\langle \Psi \left| \hat{n} \right| \Psi \rangle^2$, can also be calculated. Following the same procedure,

$$\left\langle \Psi \left| \hat{n}^2 \right| \Psi \right\rangle = |\alpha|^2 \langle \Psi \left| \hat{n} \right| \Psi \rangle + |\alpha|^2 = |\alpha|^4 + |\alpha|^2 . \tag{2.12}$$

Equation 2.12 leads to

$$\Delta n^2 = |\alpha|^2 . \tag{2.13}$$

The variance of a coherent state is the mean photon number. The result is exactly the result from standard Poissanian statistics. Indeed, the amplitude coefficients describing the coherent state define precisely a Poisson distribution

$$|\langle n \left| \Psi \right\rangle|^2 = \exp\left(- |\alpha|^2\right) \frac{|\alpha|^{2n}}{n!}. \tag{2.14}$$

A field is said to be antibunched if there is a zero probability of observing two photons at the same time (or within a finite time interval). Antibunching is the desirable property for single photon sources. Antibunching necessarily requires $g^{(2)}(0) < g^{(2)}(\tau)$, which cannot be fulfilled by a single mode field of the form of Equation 2.6. Zou and Mandel specifically pointed out that sub-Poissanian statistics and antibunching are separate phenomenon, although both purely quantum mechanical [57]. This distinction will be revisited in Chapter 6.

Antibunched light fields are represented by $g^{(2)}(0) < 1$, and is only possible if light is quantized. For time intervals greater than the lifetime of the quantum dot, the second order correlation function should approach one. Bunching, $g^{(2)}(\tau) > 1$, can be present

away from zero time delay. In the strong coupling regime, discussed in the proceeding sections, Rabi oscillations are visible in the $g^{(2)}(\tau)$ function [58, 59], evident of an enhanced probability of observing a second photon emission after a time of a single Rabi cycle. The result is explained by stimulated emission of photons from the cavity. As the strict condition for strong coupling is hard to achieve for quantum dots, *deterministic* single photons are typically generated with a time varying excitation. By exciting the system with a pulse of temporal width and repetition time smaller than the lifetime of the quantum dot, single photons can be created in a well-defined temporal bin.

Such is the case in Figure 2.1. The cavity-quantum dot sample is excited with a pulsed laser with a repetition rate of 12.5 ns. There is a lack of coincidences at zero time delay. The pulse width, 20 psec, is shorter than the Purcell enhanced lifetime, 100 psec, of the quantum dot. A second photon can only arrive during the next pulse. A $g^{(2)}(0) = 0.037 \pm 0.012$ is obtained. The presented device is a resonantly pumped fiber coupled device, as described in Reference [60].

2.3 Path Entanglement and Hong-Ou-Mandel

Consider a 50:50 lossless beam splitter. The reflection and transmission of the beam splitter is described by the complex reflection and transmission coefficients, $r = \frac{i}{\sqrt{2}}$ and $t = \frac{1}{\sqrt{2}}$. The complex electric field amplitudes, e_i, are related to each other from the following unitary transformation

$$\begin{aligned} e_2 &= \frac{1}{\sqrt{2}} e_0 + \frac{i}{\sqrt{2}} e_1 \\ e_3 &= \frac{i}{\sqrt{2}} e_0 + \frac{1}{\sqrt{2}} e_1. \end{aligned} \tag{2.15}$$

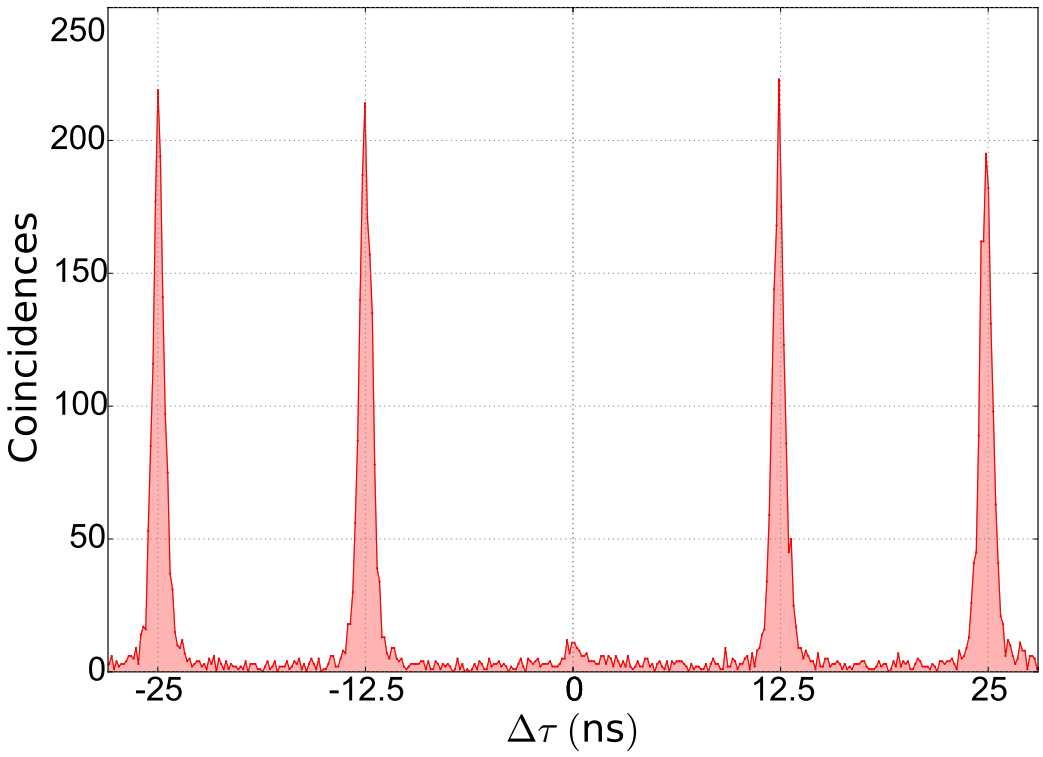

Figure 2.1: Measurement of $g^2(\tau)$ of a quantum dot embedded in a microcavity. The cavity-quantum dot system is pumped by a resonant pulsed laser with a 12.5 ns repetition rate. The lack of coincidences at $\Delta\tau = 0$ is indicative of antibunched light. The data has been published in Reference [60].

The field transformations are quantized by replacing the electric field with $\hat{a}_i$, where the subscripts denote the port of the beam splitter. In line with deriving the correlation functions, the positive frequency component of the field is kept.

$$\begin{aligned} \hat{a}_2 &= \frac{1}{\sqrt{2}} \left(\hat{a}_0 + i\hat{a}_1 \right) \\ \hat{a}_3 &= \frac{1}{\sqrt{2}} \left(i\hat{a}_0 + \hat{a}_1 \right). \end{aligned} \tag{2.16}$$

The time dependence has been dropped in Equation 2.16, ignoring path delays leading to or after the beam splitter. The adjoint of Equation 2.16 yields the transformation for $\hat{a}_i^\dagger$

$$\begin{aligned} \hat{a}_2^\dagger &= \frac{1}{\sqrt{2}} \left(\hat{a}_0^\dagger - i\hat{a}_1^\dagger \right) \\ \hat{a}_3^\dagger &= \frac{1}{\sqrt{2}} \left(-i\hat{a}_0^\dagger + \hat{a}_1^\dagger \right). \end{aligned} \tag{2.17}$$

An arbitrary state at the input port is described by appropriate operations on the vacuum state of the combined Hilbert space of both inputs, $|0\rangle_0 |0\rangle_1$. For example, a single photon incident on both input ports is $\hat{a}_0^\dagger \hat{a}_1^\dagger |0\rangle_0 |0\rangle_1$. Performing the transformation, then, leads to the output states of the beam splitter

$$\hat{a}_0^\dagger \hat{a}_1^\dagger |0\rangle_0 |0\rangle_1 = \frac{1}{2} \left(\hat{a}_2^\dagger + i\hat{a}_3^\dagger \right) \left(i\hat{a}_2^\dagger + \hat{a}_3^\dagger \right) |0\rangle_2 |0\rangle_3 = \frac{i}{\sqrt{2}} \left(|2\rangle_2 |0\rangle_3 + |0\rangle_2 |2\rangle_3 \right). \tag{2.18}$$

The above result shows that if two photons are incident on both sides of a beam splitter, there is a zero probability of observing a single photon in both output ports. The result is purely quantum mechanical. Extending the procedure, equal number photon states can be shown to always bunch at a beam splitter, creating so called N00N states. When two detectors are placed at both outputs of a beam splitter receiving single photons, then the detectors will never register a coincidence. The experiment was first performed by Hong,

Ou, and Mandel [61]. A different take on the experiment was subsequently performed by Shih and Alley [62], which utilized the polarization states of photons incident on a polarizing beam splitter.

The result of the experiment is typically rationalized according to the bosonic nature of photons, which leads to a preference for photons to bunch. The result of Equation 2.18 relies on the photons incident on the beam splitter being indistinguishable. In both experiments above, it was observed that quantum interference occurs in the case that photons arrive at the beam splitter at the same time. A time difference gives the photons a distinguishable property. In other words, it reduces the wave function overlap of the two photons.

The experiment of Pittman et. al. investigated whether photons need to be incident on a beam splitter at precisely the same time to exhibit interference [63]. Photons were directed to a polarizing beam splitter in a Shih and Alley-type experiment. The photons were purposefully made to arrive at different times. A time delay loop after the beam splitter was inserted to compensate for the different arrival times. The detectors, therefore, could not reveal this time difference. The experiment showed that photons arriving at different times on the beam splitter still bunch.

Hong Ou Mandel interference from a microcavity-quantum dot system is presented in Figure 2.2. The repetition rate of the pulsed laser is 12.5 nsec, which is not readily tunable. To measure the indistinguishability of subsequent photons, the pulse is split into two pulses by a Michelson interferometer with two retroreflectors. A fiber based Mach-Zehnder interferometer, with a path delay of 5.2 nsec between the arms, is introduced before the detectors. The pulse time difference can be fine-tuned to match the path difference in the Mach-Zehnder. The experiment allows photons emitted by two pulses to interfere on the last beam splitter. The coincidences in Figure 2.2 indicate a lack of coincidence counts when photons arrive at the same time. An indistinguishability of 0.9

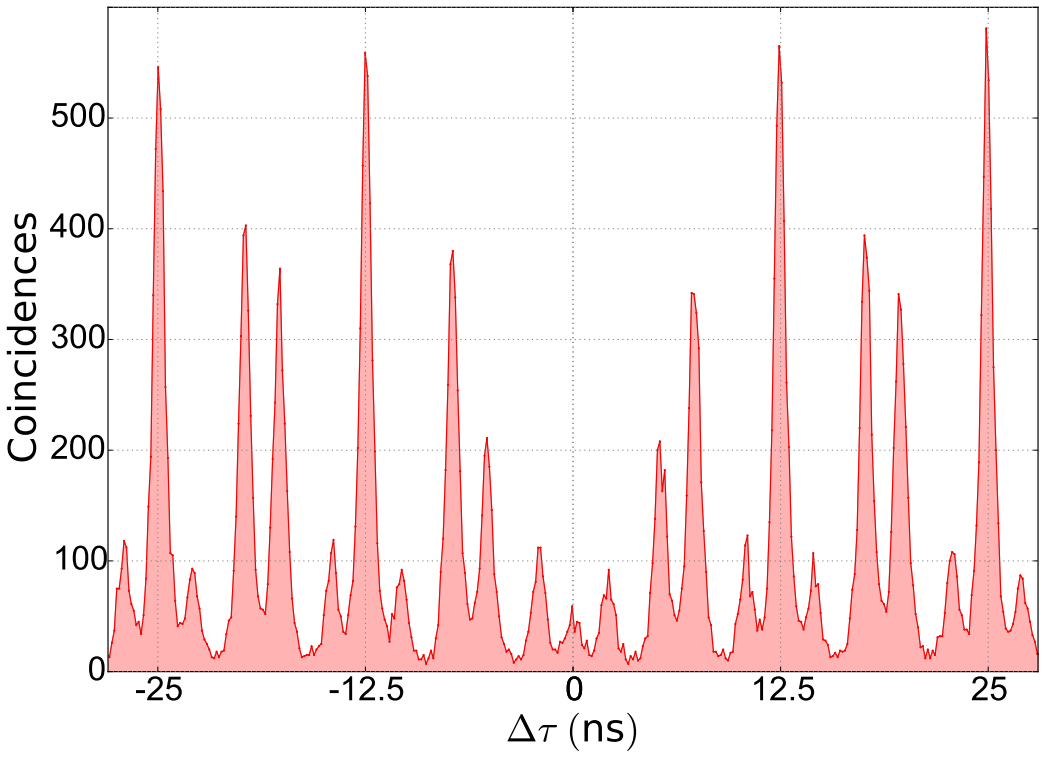

Figure 2.2: Indistinguishability measurement between subsequent photons produced from a cavity-enhanced quantum dot. The cavity-quantum dot system is pumped by a resonant pulsed laser with a 12.5 nsec repetition rate. Emitted photons enter a Mach-Zehnder interferometer, with one path including a 5.2 nsec delay. The original pulse is split into two pulses, fine tuned to match the Mach-Zehnder delay with a Michelson interferometer including a translational mirror in one arm. Coincidences are measured between two detectors after the last beam splitter. The low peak at zero time delay is evidence of bunching. The data has been published in Reference [60].

± 0.05 is obtained. As in Figure 2.1, the sample is a fiber coupled, resonantly pumped quantum dot [60].

The general action of a beam splitter on a photon state creates an entanged state between two paths. Following the procedure of Equation 2.18, a single photon incident on a beam splitter transforms as

$$\hat{a}_0^\dagger \left|0\right\rangle_0 \left|0\right\rangle_1 = \frac{1}{\sqrt{2}} \left|1\right\rangle_2 \left|0\right\rangle_3 + \frac{i}{\sqrt{2}} \left|0\right\rangle_2 \left|1\right\rangle_3 . \tag{2.19}$$

The state represented in Equation 2.19 is one of the maximally entangled Bell states, usually denoted $|\Psi^+\rangle$. A detection in one path, immediately places the other in the vacuum state. Path entanglement plays a critical role when cascading optics, such as in a Mach-Zehnder interferometer. Applying the unitary transformation to both beam splitters, it can be shown that a photon entering through one port, can only leave through a single port. The result is identical to classical wavelike interference, and is observed despite the fact that photons may enter the interferometer one at a time. Grangier et. al. verified this property with single photons from an atomic source [64]. Where as path entanglement of single photons can be reduced to a classical interpretation, Hong Ou Mandel interference is a distinctively quantum phenomenon, and plays a crucial role in quantum information processing.

2.4 Jaynes-Cummings Hamiltonian

Consider the quantized electric field

$$E = \sqrt{\frac{\hbar\omega}{\epsilon_0 V}} \left(\hat{a} + \hat{a}^\dagger\right) . \tag{2.20}$$

Equation 2.20 is the quantized field of a single cavity mode, i.e. a standing wave. Note the time dependence is dropped compared to Equation 2.6. The position dependence is further dropped for simplicity, and it is assumed the atom or quantum dot is located at a field anti-node.

Following classical correspondence, the atomic transitions are treated as atomic dipoles. The dipole approximation allows the use of the atomic transition operators, which are identical to the Pauli spin operators defined by the commutation relations

$$[\hat{\sigma}_+, \hat{\sigma}_-] = \hat{\sigma}_3 \tag{2.21}$$

$$[\hat{\sigma}_3, \hat{\sigma}_\pm] = \pm 2\hat{\sigma}_\pm. \tag{2.22}$$

The interaction Hamiltonian of a dipole in an electric field is given by

$$\hat{H}_{Int} = -\hat{d} \cdot \hat{E}, \tag{2.23}$$

where d is the dipole moment of the transition. The dipole moment, determined by the shape and size of the quantum dots, is large in the transverse plane of the growth. The transitions are linear, separated by the electron-hole exchange interaction [30]. In general, quantum dots tend not to align with one particular crystal axis [65]. The interaction of Equation 2.23 is given by

$$\hat{H}_{Int} = \hbar g \left(\hat{\sigma}_+ + \hat{\sigma}_-\right)\left(\hat{a} + \hat{a}^\dagger\right), \tag{2.24}$$

where the coupling strength g is defined as

$$g = -d\sqrt{\frac{\hbar\omega}{\epsilon_0 V}} \tag{2.25}$$

Expanding the operators in Equation 2.24 reveals there are non-energy conserving terms. It turns out the introduction of the rotating wave approximation eliminates these terms. Generally, this approximation is adopted. Including the free energy terms of the cavity field and the atom, the Jaynes-Cummings Hamiltonian is [66]

$$\hat{H} = \frac{1}{2}\hbar\omega_0\hat{\sigma}_3 + \hbar\omega\hat{a}^\dagger\hat{a} + \hbar g\left(\hat{\sigma}_+\hat{a} + \hat{\sigma}_-\hat{a}^\dagger\right). \tag{2.26}$$

The first term in Equation 2.26 is the energy of the atom with frequency ω_0. There are two eigenvalues, corresponding to the ground and excited states of the atom. The second term is the energy of the photons in the cavity, which is given by the number of photons in the cavity. The eigenstates with $g = 0$ are called the bare states, $|n\rangle|e\rangle$ and $|n+1\rangle|g\rangle$.

With non-zero g, the bare states are coupled. The eigenstates of the full Jaynes-Cummings Hamiltonian are known as the dressed states. It can be verified that the operators $(\hat{\sigma}_+\hat{\sigma}_- + \hat{\sigma}_-\hat{\sigma}_+)$and $\left(\hat{a}^\dagger\hat{a} + \hat{\sigma}_+\hat{\sigma}_-\right)$ are constants. The Hamiltonian in the interaction picture can be written

$$\hat{H} = \hbar\left(\omega_0 - \omega\right)\hat{\sigma}_+\hat{\sigma}_- + \hbar g\left(\hat{\sigma}_+\hat{a} + \hat{\sigma}_-\hat{a}^\dagger\right). \tag{2.27}$$

The dressed states can be solved for with the interaction term,

$$|n+\rangle = \sin\left(\frac{\Phi_n}{2}\right)|n+1\rangle|g\rangle + \cos\left(\frac{\Phi_n}{2}\right)|n\rangle|e\rangle, \tag{2.28}$$

and

$$|n-\rangle = -\cos\left(\frac{\Phi_n}{2}\right)|n+1\rangle\,|g\rangle + \sin\left(\frac{\Phi_n}{2}\right)|n\rangle\,|e\rangle\,. \tag{2.29}$$

The angle, Φ_n, is defined by

$$\Phi_n = \tan^{-1}\left(\frac{2g\sqrt{n+1}}{\omega_0-\omega}\right). \tag{2.30}$$

The states in Equations 2.28 and 2.29 represent the excitations of the coupled two level-cavity system. The corresponding eigenvalues are given by

$$E_{\pm}(n) = \left(n+\frac{1}{2}\right)\hbar\omega \pm \frac{1}{2}\hbar\sqrt{(\omega-\omega_0)^2 + 4g^2(n+1)}, \tag{2.31}$$

which shows that the energy splitting of the dressed states are photon number dependent. The number dependent dressing of states is a property, which only arises in the fully quantum mechanical description of atom-field interactions. A number of purely quantum mechanical phenomena arise from the Jaynes-Cummings Hamiltonian. Many textbooks cover the Jaynes-Cummings model, and a detailed review is given by Shore and Knight [67].

The equations of motion are typically calculated in the Heisenberg picture. It is important to note that a semi-classical approximation is often used. What is usually of interest is the expectation value of an operator. Consider two operators $\hat{A}$, and $\hat{B}$, and the operator defined by the product $\hat{A}\hat{B}$. The semi-classical approximation ignores quantum correlations in the expectation value such that $\left\langle \hat{A}\hat{B}\right\rangle = \left\langle \hat{A}\right\rangle\left\langle \hat{B}\right\rangle$ [68]. In the semi-classical approximation, the equations of motion for the expectation values of the operators, $\dot{\hat{\sigma}}_3$, $\dot{\hat{a}}$ and $\dot{\hat{\sigma}}_+$, are given by

$$\left\langle \dot{\hat{\sigma}}_3\right\rangle = -2ig\left(\langle\hat{a}\rangle\langle\hat{\sigma}_+\rangle - \left\langle\hat{a}^\dagger\right\rangle\langle\hat{\sigma}_-\rangle\right), \tag{2.32}$$

$$\left\langle \dot{\hat{a}} \right\rangle = -i \left(\omega \left\langle \hat{a} \right\rangle + g \left\langle \hat{\sigma}_- \right\rangle \right), \tag{2.33}$$

$$\left\langle \dot{\hat{\sigma}}_+ \right\rangle = i\omega_0 \left\langle \hat{\sigma}_+ \right\rangle - ig \left\langle \hat{a}^\dagger \right\rangle \left\langle \hat{\sigma}_3 \right\rangle. \tag{2.34}$$

It was encountered in the framework of measuring the second order coherence, and is universal in quantum mechanics, that a measurement must be performed to reveal any information about the system. The Jaynes-Cummings model constitutes a highly idealized system, which is completely isolated from the outside world. Therefore, in practice, it is impossible to realize the exact Jaynes-Cummings model. The introduction of cavity loss and atomic decay rates must come into play. Where the Jaynes-Cummings Hamiltonian still shines is where the atom-cavity coupling greatly exceeds the losses in the system. This condition is known as the strong coupling regime, which is difficult to achieve with semiconductor microcavities. Current progress, however, has pushed close to this limit.

A completely coherent Hamiltonian can be formulated by representing the outside system as a collection of harmonic oscillators. The reflection and transmission can be solved with input output theory [69]. This type of problem was studied in the context of semiconductor microcavities [70, 71]. It is typically assumed that the semi-classical assumption gives a good approximation of the dynamics. The weak excitation limit is also typically assumed, where $\langle \hat{\sigma}_3 \rangle = -\frac{1}{2}$. The reflection of a cavity-quantum dot system with these assumptions can be solved for [72, 73, 74]

$$r = 1 - \eta_{in} \frac{1}{1 - i\Delta + \frac{2C}{1 - i\Delta'}}, \tag{2.35}$$

where $\Delta = \frac{2(\omega_l - \omega)}{\kappa}$ and $\Delta' = \frac{(\omega_l - \omega_0)}{\gamma}$. ω_l is the laser frequency, κ is the cavity loss rate,

and γ is the spontaneous emission rate. η_{in} is the coupling efficiency. The cooperativity is given by $C = \frac{g^2}{\kappa\gamma}$. Equation 2.35 describes a Lorentzian cavity dip, superimposed with an additional Lorentzian peak inside of the cavity at the quantum dot resonance. Off resonance, the lineshape can exhibit a Fano pattern [75].

Even if the system is not in the strong coupling regime, a single atom, or quantum dot, strongly coupled to a cavity mode can reverse the reflection/transmission of a cavity. Waks and Vuckovic pointed out that the condition for observing a strong non-linearity is that there exist a Purcell factor $F > 1$, where the cavity mode volume is small enough to shorten the emitter lifetime on resonance with the cavity [71].

Figure 2.3 shows a calculated reflection spectrum of a cavity enhanced quantum dot in the weak excitation regime. A qualitative interpretation is given by the fact that radiating modes are restricted to the cavity mode, funneling the fluorescence into the cavity. In the calculation $g = 2$ GHz, $\gamma = 0.1$ GHz, and $\kappa = 8$ GHz. The coupling efficiency, η_{in}, is set to one. The calculation represents a symmetrical cavity, with perfect in-coupling, allowing the reflection dip to reach zero. The experimental values represent optimistic, but realistic, values. The cooperativity is in the regime where polariton splitting is barely resolvable. Therefore, the peak appears wider than the emitter lifetime because of the appearance of the dressed states. With more loss, and weaker coupling, the width of the peak would more closely reflect the radiative lifetime of the dot.

2.5 Dissipative Interactions

The above section outlines the basic semi-classical theory of interactions of a quantum dot and a single cavity mode field. Because measurements are made from observable quantities outside the cavity, the Jaynes-Cummings Hamiltonian isn't complete in describing the system. Further, losses in the system play a fundamental role. The general

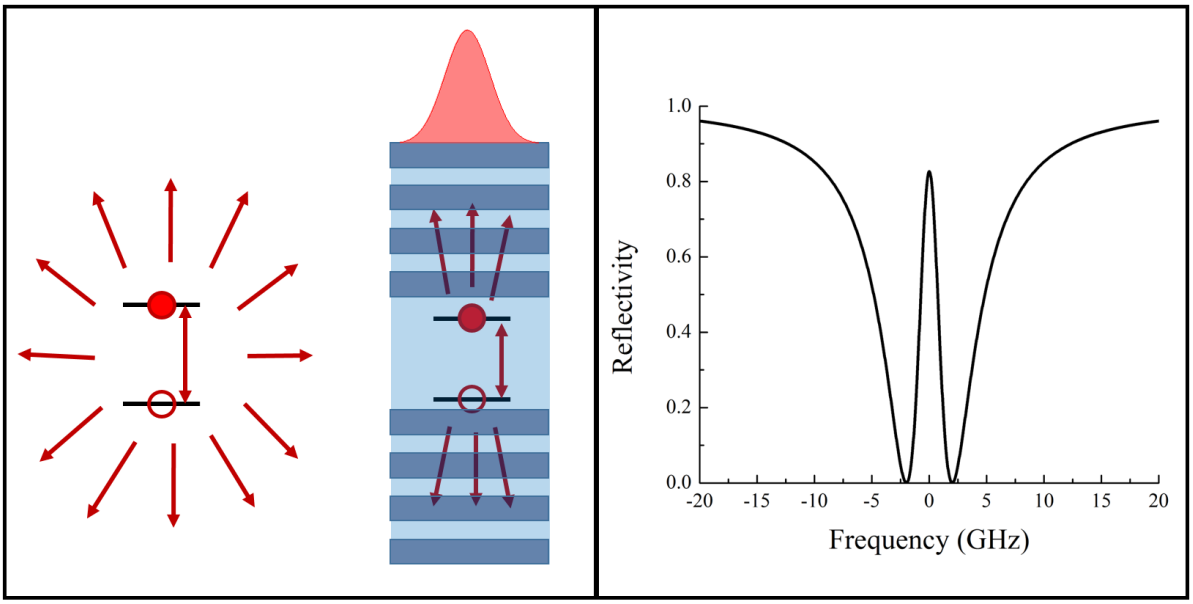

Figure 2.3: (Left) Diagram indicating the effect of constricting emission of a single emitter to a single cavity mode. (Right) calculated spectrum, with reasonable experimental values, of a Purcell enhanced quantum dot in a microcavity. $g = 2$ GHz, $\gamma = 0.1$ GHz, and $\kappa = 8$ GHz.

Hamiltonian for a system and a reservoir is represented by

$$\hat{H} = \hat{H}_S + \hat{H}_R + \hat{H}_{SR}. \tag{2.36}$$

$\hat{H}_S$ is the system Hamiltonian, $\hat{H}_R$ is the reservoir Hamiltonian, and $\hat{H}_{SR}$ is the interaction between the system and the reservoir. $\hat{H}_S$ is the standard Jaynes-Cummings Hamiltonian, $\hat{H}_R$ is a collection of harmonic oscillators, and $\hat{H}_{SR}$ are the interaction terms coupling photons from outside to inside the cavity. A quantum master equation can be derived for the system, which is left to the literature [76]. The Markovian approximation is used for the work in this thesis, which neglects coherent interactions between the system and the reservoir.

Operators describing gain or loss, in general, are non-Hermitian. States prepared in a pure state do not generally remain so, and so the density operator, $\hat{\rho}$, must be used to

describe dynamics of the system. The density operator can be defined by

$$\hat{\rho} = \sum_i p_i \left|\psi_i\right\rangle \left\langle\psi_i\right|, \tag{2.37}$$

for a mixed state. p_i is the probability of being in the state $|\psi_i\rangle$. The time evolution of the density operator is the von Neumann equation

$$\dot{\hat{\rho}} = \frac{i}{\hbar}\left[\hat{\rho}, \hat{H}\right]. \tag{2.38}$$

Equation 2.38 is also written in terms of the Liouvillian superoperator, $\mathcal{L}$

$$i\hbar\dot{\hat{\rho}} = \mathcal{L}\hat{\rho}. \tag{2.39}$$

The expectation value of an operator is given by

$$\left\langle \hat{A} \right\rangle = \mathrm{Tr}\left[\hat{\rho}\hat{A}\right]. \tag{2.40}$$

Including a coherent drive, the Jaynes-Cummings model in a frame rotating at the drive frequency is given by [77]

$$\hat{H} = \frac{1}{2}\hbar\left(\omega_l - \omega_0\right)\hat{\sigma}_+\hat{\sigma}_- + \hbar\left(\omega_l - \omega\right)\hat{a}^\dagger\hat{a} + i\hbar g\left(\hat{\sigma}_+\hat{a} + \hat{\sigma}_-\hat{a}^\dagger\right) + i\hbar\eta\left(\hat{a}^\dagger - \hat{a}\right). \tag{2.41}$$

η is the strength of the electric field. At optical frequencies, thermal excitations from the reservoir are negligible. The relevant relaxation mechanisms are spontaneous emission of the atom, the cavity decay rate, and dephasing mechanisms. With the Markovian

assumption the density matrix evolution is given by

$$\frac{d\hat{\rho}}{dt} = -\left[\hat{H}, \hat{\rho}\right] + \frac{\kappa}{2}\hat{D}\left[\hat{a}\right]\hat{\rho} + \frac{\gamma}{2}\hat{D}\left[\hat{\sigma_+}\right]\hat{\rho} + \frac{\gamma^*}{2}\hat{D}\left[\hat{\sigma}_3\right]\hat{\rho}. \tag{2.42}$$

Excluding dephasing, including the assumptions that quantum correlations can be neglected, and setting the quantum dot expectation value to the ground state energy, the semi-classical formula can be found for the annihilation operator. There is a package for Python, QUTIP, used for numerically solving Equation 2.42 [78, 79], when these assumptions do not apply. The general dynamics of the system are either solved through numerically computing the coupled differential equations, or through implementing a Monte Carlo simulation of quantum jumps.

2.6 Classical Polarized Equations

The quantum dot-cavity interaction can be put into a completely classical context. The problem is precisely that of two coupled cavities, separated by a weakly reflecting mirror. The weak mirror, in this case, is a layer of quantum dots. It is easy to see, through a coupled mode analysis, that the coupling of two cavities results in mode splitting of the isolated cavity modes [80]. The general applicability of coupled mode theory motivates the use of describing the quantum dot-microcavity system in completely classical terms.

The classical transmission can be derived, in a slightly ad-hoc manner, by assigning a Lorentzian spectral dependence to the leaky mirror representing the quantum dots. Further, the classical approach is easily extendable to the case of polarized cavities and quantum dot transitions. The transmission of the polarized system can be derived in the

form [81, 82, 74]

$$t_{2x2} = \eta_{out} \left[I_{2x2} - \begin{pmatrix} i\Delta_H & 0 \\ 0 & i\Delta_V \end{pmatrix} + R_{-\theta_{QD}} X R_{\theta_{QD}} \right]^{-1} . \tag{2.43}$$

η_{out} is the out-coupling efficiency. The parameters Δ and Δ' describe the round trip phase for the cavity and the quantum dot respectively. $\Delta = 2\frac{\omega_l - \omega_c}{\kappa}$ and $\Delta' = 2\frac{\omega_l - \omega_c}{\gamma}$. X here describes the general interaction of the quantum dot with the light field. $R_{\theta_{QD}}$ is the standard two level rotation matrix, and θ_{QD} is the angle between the quantum dot and the excitation light. X is diagonal in the cavity basis for the linearly polarized neutral quantum dot

$$X = \begin{pmatrix} \phi_H & 0 \\ 0 & \phi_V \end{pmatrix}, \tag{2.44}$$

where $\phi_i = \frac{2C_i}{1-\Delta_i'}$, and C_i is the cooperativity used in Equation 2.3.

The amount of single photon light extracted from resonant excitation and post-selection can be derived by including a polarizer in detection. Information on photon statistics necessarily disappears in a classical description. In the simple cross polarization case, though, the quantum dot light can be completely separated from the coherent drive light, and treated as a perfect antibunched source. No single photon light occurs in the limit that the quantum dot is excited exactly along its axis, or if the quantum dot displays zero fine structure splitting, as no polarization rotation can be induced.

Although, not grounded in rigorous assumptions, the classical model reproduces exactly the semi-classical formalism in the limit of weak excitation. Effects, such as saturation and pure dephasing are not present in either case. The classical formalism is particularly useful to describe the polarization rotations induced by a linearly polarized quantum dot, and has the advantage of being very easy to work with. The classical

model agrees with experiments on polarization tomography, which have been suggested to be a benchmark for studying deviations from the semi-classical behavior [43].

2.7 Conclusion

The theory in this chapter sets the stage for understanding the generation of single photon sources and the quantum dynamics of quantum dots interacting with bi-modal cavities. Single photon sources for quantum information processing must be perfectly pure, possesing a $g^{(2)}(0) = 0$. Subsequent photons must also be indistinguishible, such that the photons display Hong-Ou-Mandel interference at a beam splitter. In a polarization degenerate cavity, with certain assumptions, the quantum dot behaves as a single photon polarization rotator. Single photons can be generated in cross polarization, then, as the coherent drive is blocked and antibunched quantum dot light is allowed through. Such a description can be modeled well with completely classical dynamics. A complete description of single photon generation, though, must be computed with the Jaynes-Cummings Hamiltonian including loss. Interesting physical phenomenon arise in the quantum description. These phenomenon are discussed in Chapter 6.

Chapter 3

Quantum Dot Properties and Characterization

The consequences of quantum confinement of electronic states in semiconductors are critical in optics applications. As a result, quantum dots have been intensively studied. Quantum dots are primarily produced by direct lithography, self-assembly during semiconductor growth, and colloidal chemistry. The quantum dots in this thesis are self-assembled InGaAs/GaAs quantum dots grown by molecular beam epitaxy (MBE). This chapter presents the basic theory of optical transitions in quantum dots, and the optical characterization experiments at UCSB used to investigate the electronic states of excitons in quantum dots.

3.1 Optical Transitions in Semiconductors

From Bloch's theorem, the wavefunctions of electrons and holes in a periodic potential can be calculated. The result is the formation of bands of quasi-continuous states. In semiconductors, a band gap forms, where there is an energy range of forbidden electronic

states. Transitions occur from the initially filled valence band to the empty conduction band. The angular momentum of the carriers in the bands comes from the addition of the orbital angular momentum and the spin. The conduction band originates from s-like atomic states with zero orbital angular momentum, $\ell = 0$. Electrons, with spin $s = \frac{1}{2}$, therefore, carry a total angular momentum quantum number, $j = \ell + s = \frac{1}{2}$, and angular momentum projection, $m = \pm\frac{1}{2}$. The valence band model, developed by Kane [83], has three bands. Valence bands arise from atomic p-shell states, with an orbital component $\ell = 1$. Therefore, carriers have $j = \frac{3}{2}$, and m can take on the values $m = \pm\frac{3}{2}$ and $m = \pm\frac{1}{2}$. The valence band states are degenerate in a bulk crystal at the Γ point, with crystal momentum $k = 0$. This ignores a small spin splitting from the lack of inversion symmetry in the crystal. The split off band, carrying $m = \pm\frac{1}{2}$, is separated from the direct band edge by the spin-orbit coupling.

Direct band gap materials, such as GaAs and InGaAs, have conduction band minimum and valence band maximum overlapping in k-space. The direct gap allows for efficient emission of photons because electrons and holes can recombine without the need of phonons to conserve angular momentum. It is typically sufficient to consider transitions around this direct gap, around the Γ point. The band structure at this point is parabolic to a good approximation. The bands are represented in Figure 3.1 (a). The heavy holes have $m = \pm\frac{3}{2}$, and the light holes have $m = \pm\frac{1}{2}$. Heavy holes have a greater effective mass, therefore they display less curvature. The degeneracy of the heavy holes and light holes is lifted in quantum confined structures: wells, wires, and dots. The confinement energy is inversely proportional to mass; the difference in the effective masses of the heavy holes and light holes means the light holes are pushed further away from the band edge. Ground state transitions occur from the heavy hole band to the conduction band in the absence of strain related effects.

Through hetero-epitaxy, sequences of different materials can be deposited on top of

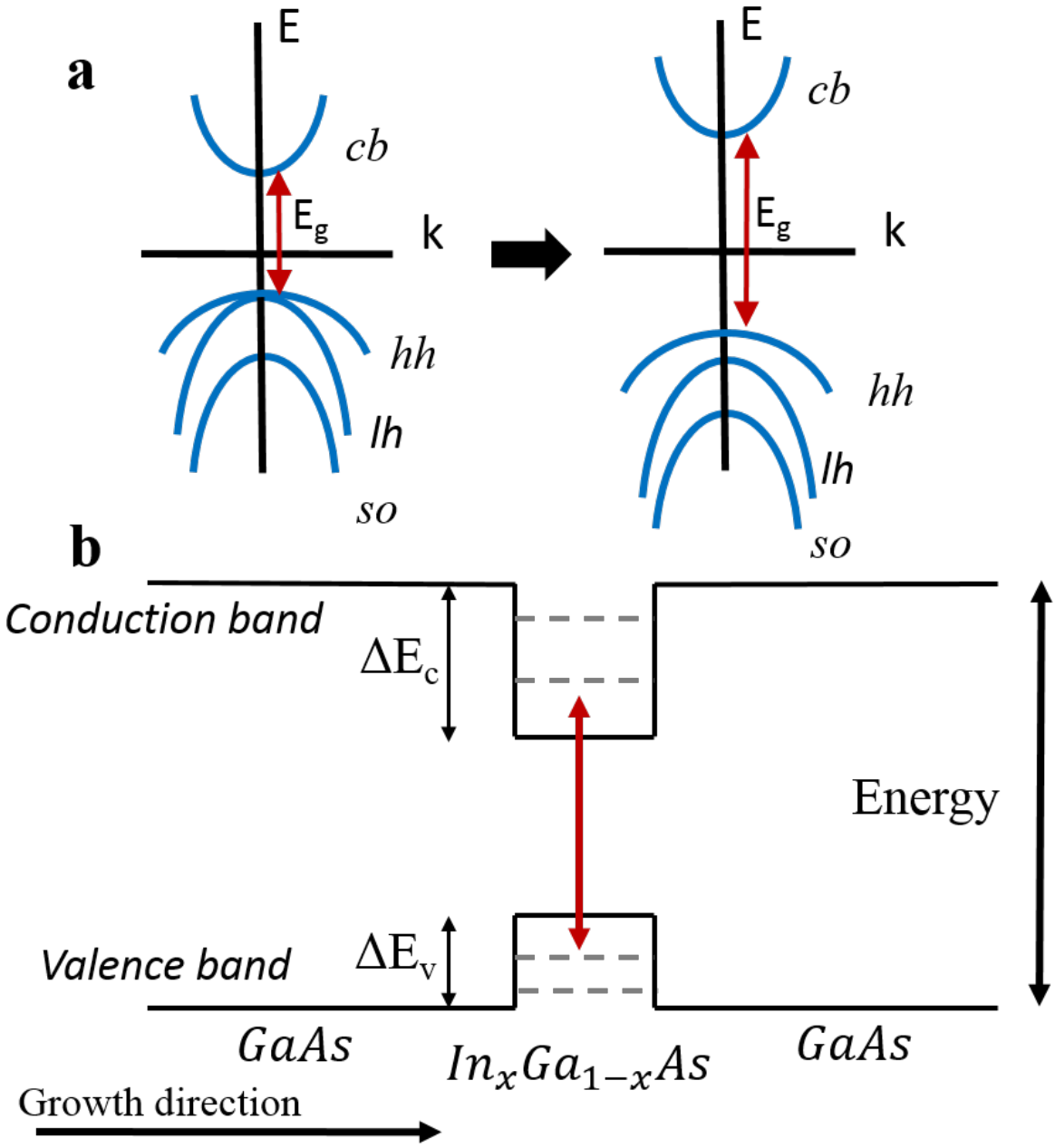

Figure 3.1: (a) Electron energy dispersion diagram around the Γ point in III-V direct gap materials. Quantum confinement (right) lifts the degeneracy between the heavy holes and the light holes. The ground state transitions occur from the heavy holes to the conduction band. (b) One dimensional cross section of the band diagram of an InGaAs quantum dot. The band gap of InGaAs is less than GaAs, exhibiting type I band alignment.

each other without introducing crystal defects. The band gap of a device can be spatially tuned. Because of the different band gaps, interfaces between different materials produce an electrostatic potential. The theory for determining band gaps is well formulated, as it involves properties of bulk crystals. The method of calculating exact band lineups, however, is not always straightforward. The simplest method is Andersons's rule, for which the conduction band offset is calculated directly from the difference in electron affinities of the two materials [84]. Essentially, the materials near the interface are assumed to exhibit their bulk properties. One can also derive a first principles calculation of band offsets [85, 86].

In one dimension, the band diagram for an InGaAs quantum dot is shown in Figure 3.1 (b). Exact values of the alloy can vary depending on growth conditions. Thermal annealing can also lead to intermixing of the alloys at the interface. The band diagram is type I, whereby both electrons and holes are confined in the quantum dot. Gray lines indicate quantum confined levels.

The energy splitting of the heavy holes and light holes is large enough so that the light holes can be neglected in most experiments. The optical ground state transitions of a neutral quantum dot, in the circular polarization basis, are shown in Figure 3.2. Four electron-hole spin orientations are allowed. $m_{total} = \pm 2$ when the spins are aligned, and $m_{total} = \pm 1$ when the spins are anti-aligned, where m_{total} is the total angular momentum of the electron-hole pair, or exciton. To preserve angular momentum, optical transitions are allowed to the states with anti-aligned spins. These states are called the bright states. Excitons prepared in a dark state must interact with the environment to flip one of its spins before a radiative transition is allowed. Therefore, excitons in this configuration typically exhibit longer lifetimes. Stranski-Krastanov growth typically yields quantum dots with non-symmetric shapes. The degeneracy of the neutral bright states is therefore lifted by the electron-hole exchange interaction [30]. The two transitions are linearly

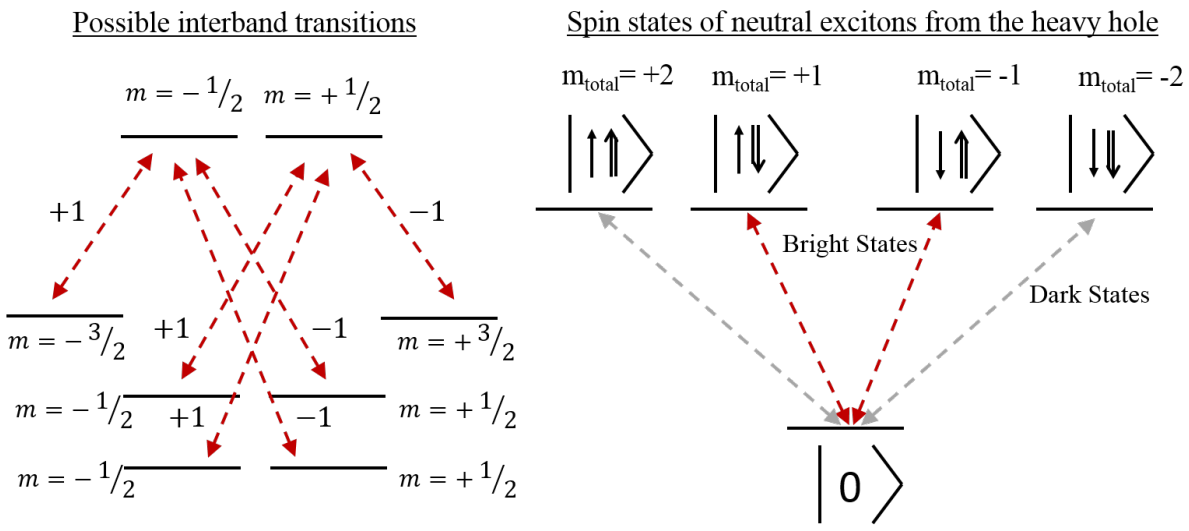

Figure 3.2: Circularly polarized ground state transitions of a neutral quantum dot. The left picture displays the allowed transitions in the band structure. Ground state transitions are from the heavy hole band. The ket notation in the right picture displays the possible exciton spin states from the ground state transitions. The bright states result in electron and hole spins anti-aligned in order to conserve angular momentum.

polarized with their dipole moment transverse to the growth direction.

3.2 Quantum Dot Growth

Three hetero-epitaxy growth modes are possible: Frank-van der Merve (layer-by-layer), Volmer-Weber (island), and Stranski-Krastanov (wetting layer and island). The growth mode is determined by the energy costs due to strain and surface energy. Materials with the same crystal structure, and similar lattice constants, can be grown without strain induced in the new deposited layers. Lattice matched materials generally grow in the Frank-van der Merve mode. These materials can be grown relatively freely, and resulting films can be made very thick. For lattice mis-matched materials, strain develops, causing a tendency for the deposited material to form clusters. In the high strain situation, Volmer-Weber type growth results, where the deposited material immediately nucleates

into clusters. An intermediate situation is the Stranski-Krastanov mode. In Stranski-Krastanov, the deposited material reduces surface energy by forming a wetting layer of only a few monolayers thick. Nucleation of clusters results after the formation of the wetting layer.

InAs exhibits a lattice constant $\sim 7\%$ larger than GaAs [87], making layer-by-layer growth of InAs on GaAs extremely unfavorable. The Stranski-Krastanov mode of growth is energetically favorable instead. Quantum dots nucleate into lens shaped clusters after the initial wetting layer. A typical atomic force microscope image is displayed in Figure 3.3 (a). Quantum dot density can be controlled by tuning the indium flux during growth. From the atomic force microscope image, a density of $\sim 200\frac{1}{\mu m^2}$ can be deduced for this particular growth.

The quantum dots are grown through MBE at a growth temperature of around 500°C. The substrate temperature is used to tune the resonance frequency of the quantum dots. Atomic diffusion on the surface is faster at higher temperatures, resulting in bigger quantum dots, which fluoresce at longer wavelengths. Increasing the temperature further results in desorption of atoms, giving smaller, shorter wavelength quantum dots. The pattern is demonstrated in Figure 3.3 (b), which shows the photoluminescence spectrum of four quantum dot calibration samples. The quantum dot distribution is centered at 1020 nm. The dots typically have a wide size distribution, giving a wide distribution of emission wavelengths. The next peak towards higher energy is the quantum well peak from the wetting layer. On the far left, the tail of the GaAs band gap emission is visible. Additional growth details can be found in Appendix A of Reference [88].

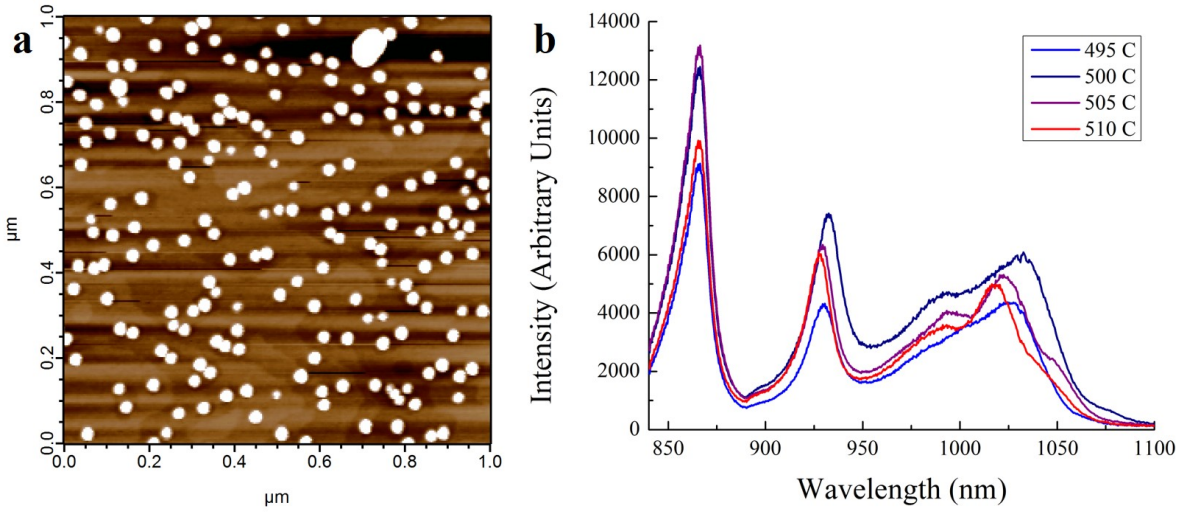

Figure 3.3: (a) Atomic force microscope image of a typical quantum dot sample without a microcavity. (b) Temperature calibration performed at room temperature via photoluminescence.

3.3 UCSB Optical Setup

Experiments are conducted at UC Santa Barbara (UCSB) and Leiden University. The optical setup at UCSB is detailed below. Properties of the samples are probed either by photoluminescence or reflection. Photoluminescence from quantum dots is measured from exciting the sample optically, with a laser of energy greater than the GaAs band gap. Electronic states of quantum dots can be identified from carrier relaxation into the quantum dot levels. Reflection measurements are performed on microcavities, outlined in Section 1.3, in order to isolate single quantum dots. High resolution is obtained by resonantly exciting the system with a narrow linewidth laser. Individual quantum dots can be identified through Purcell enhancement in the cavities.

Quantization energies are on the order of ~ 10 meV, therefore, carriers can be thermally excited at room temperature. To prevent this, samples are loaded into a cryostat and cooled to 6K. The cryostat houses a *cold objective*, which is positioned directly above the sample. The cold objective design provides extreme long-term stability; samples do

not drift after being cooled down. Without a cold objective, the sample must be placed close to a window, and a long working distance objective must be used to focus light on to the sample. Lab temperature fluctuations can affect the alignment of the objective with the sample in the later case. Samples are mounted on thermally conducting substrates. Copper, alumina, and AlN are typically used. More details of the packaging process are given in Appendix A. Wires soldered to the packaged device are connected to sockets inside of the cryostat, which also provide electrical access to the thermometers and piezo stages (Attocube).

3.3.1 Photoluminescence Measurements

The photoluminescence experiment is shown in Figure 3.4. Fiber coupled light sources are collimated with 10X objectives. The objectives are all mounted on Elliot stages to optimize in/out-coupling to and from the fibers. Light is directed through a periscope above the cryostat window, and directed downwards. Excitation and collection occurs through the same microscope objective. The photoluminescence is picked off by a dichroic beam splitter and filtered from excitation light with a long pass filter. The light is then coupled to a collection fiber. A spectrum of the emitted light is obtained by passing the light through a 1.25 m long grating spectrometer (SPEX1250M), and the output is imaged on a liquid nitrogen cooled charge coupled device (CCD). A spectral resolution of 12 pm can be obtained over a 15 nm window. Longer windows are obtained by stitching multiple spectra together.

An ensemble photoluminescence measurement on a sample of quantum dots, which are not embedded in a device, is presented in Figure 3.5 (a). The sample is a single layer of InGaAs quantum dots in GaAs. The sample is pumped with a continuous wave Titanium Sapphire laser (MSquared Solstice), outputting a wavelength of 780 nm. The

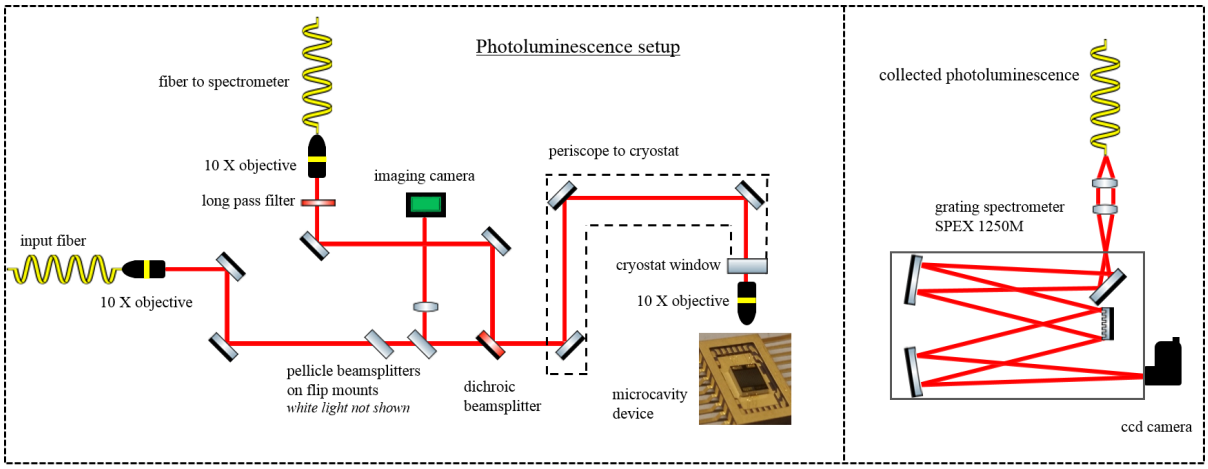

Figure 3.4: Optical setup for photoluminescence characterization. On the left is the optical setup. Photoluminescece is collected with a dichroic beam splitter, further filtered from the excitation laser with a long pass filter before entering a fiber. The collection fiber is sent to a grating spectrometer and CCD camera.

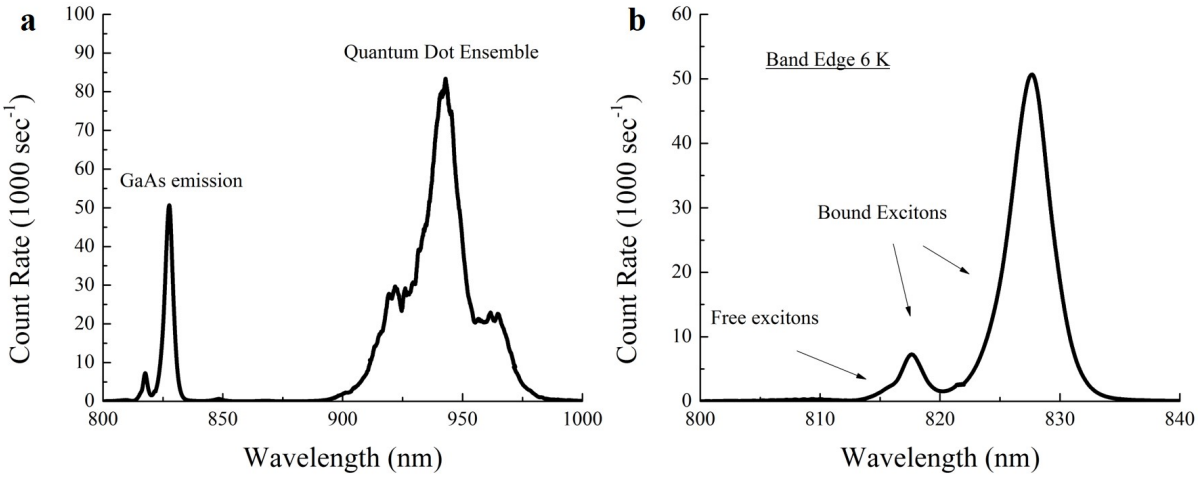

Figure 3.5: Photoluminescence measurement performed on an ensemble of quantum dots at 6K. (a) Measurement with 20 μW from 800 nm to 1000 nm displaying the quantum dot distribution. (b) A zoom in on the band edge. The GaAs band gap is located at 815 nm. The two peaks close to the band edge emerge at low temperatures from the formation of bound states at background donor and acceptor atoms.

excitation power at the objective is 20 μW. Photoluminescence is collected, after being filtered with a dichroic beam splitter, into a multimode fiber. The multimode fiber is used to avoid spectral artifacts over the broad range of wavelengths. The quantum dots shift to a center wavelength of 940 nm after being cooled, the target wavelength for microcavities. The distribution is far from a normal distribution, with small peaks on both sides of the center. It is not uncommon for dots to nucleate without a perfect normal distribution. Bimodal distributions are commonly reported. The peak on the high energy side could be a set of small dots, or the emergence of the p-shell. The power is kept low to avoid p-shell emission, however, the finite relaxation time could lead to a small amount of emitted light even at low power.

The band edge is analyzed closer in Figure 3.5 (b). At 6 K, the GaAs band gap is at 815 nm. Free exciton emission can be observed at energies above the band gap. The spectrum around the band edge can exhibit interesting features from the formation of bound excitons. There is a finite level of background donors and acceptors, leading to strong bound exciton transitions. Two peaks emerge in the photoluminescence spectrum around the band edge from donor bound and acceptor bound excitons, which fluoresce strongly compared to free excitons due to their spatial localization. The bound exciton emission disappears when warming up, as the thermal energy becomes greater than the exciton binding energy.

The power dependence of the quantum dot photoluminescence is studied further on the ensemble measurement. The three dimensional confinement results in atomic like energy levels, labelled s, p, d... [89]. The normalized intensity with varying power of the ensemble is shown in Figure 3.6, demonstrating the onset of the higher principal quantum number states. Three extra peaks emerge at high powers, which is attributed to the filling of the p and d shells, and finally the wetting layer. The radiative lifetime of these states is longer than the cascade to the s-shell, therefore requiring high power to

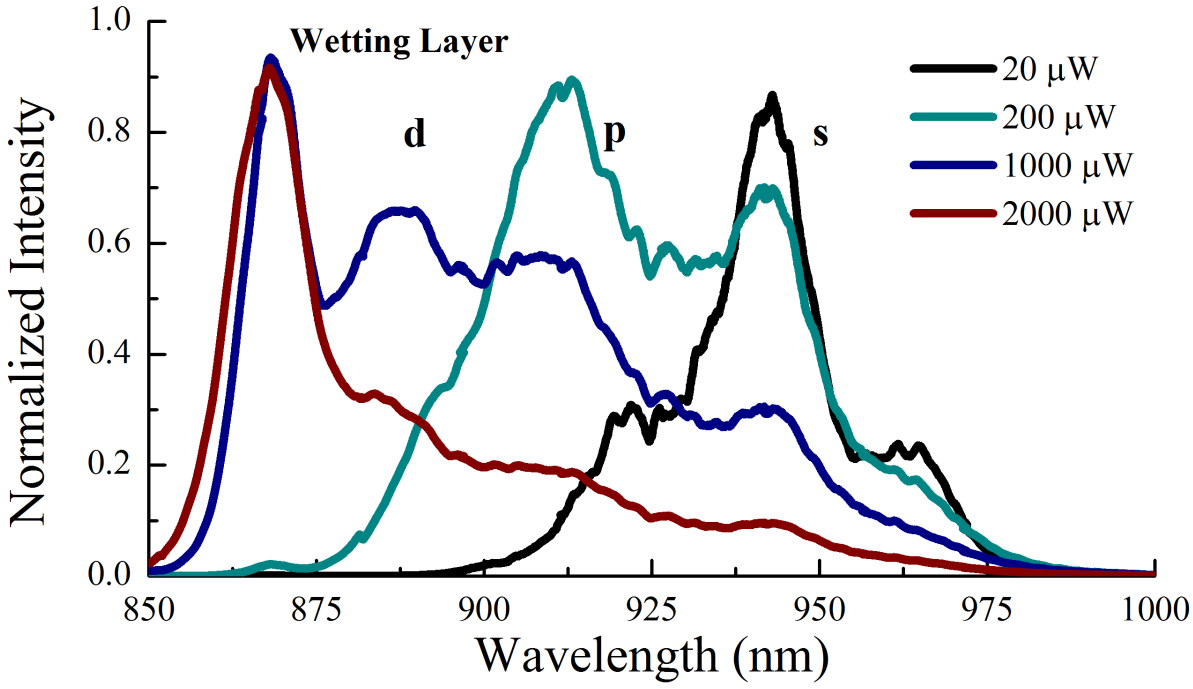

Figure 3.6: Power dependence of photoluminescence from an ensemble of quantum dots at 6K. Four states can be identified from 20 μW to 2000 μW, attributed to the filling of states from the s, p, and d-shells, and finally the wetting layer.

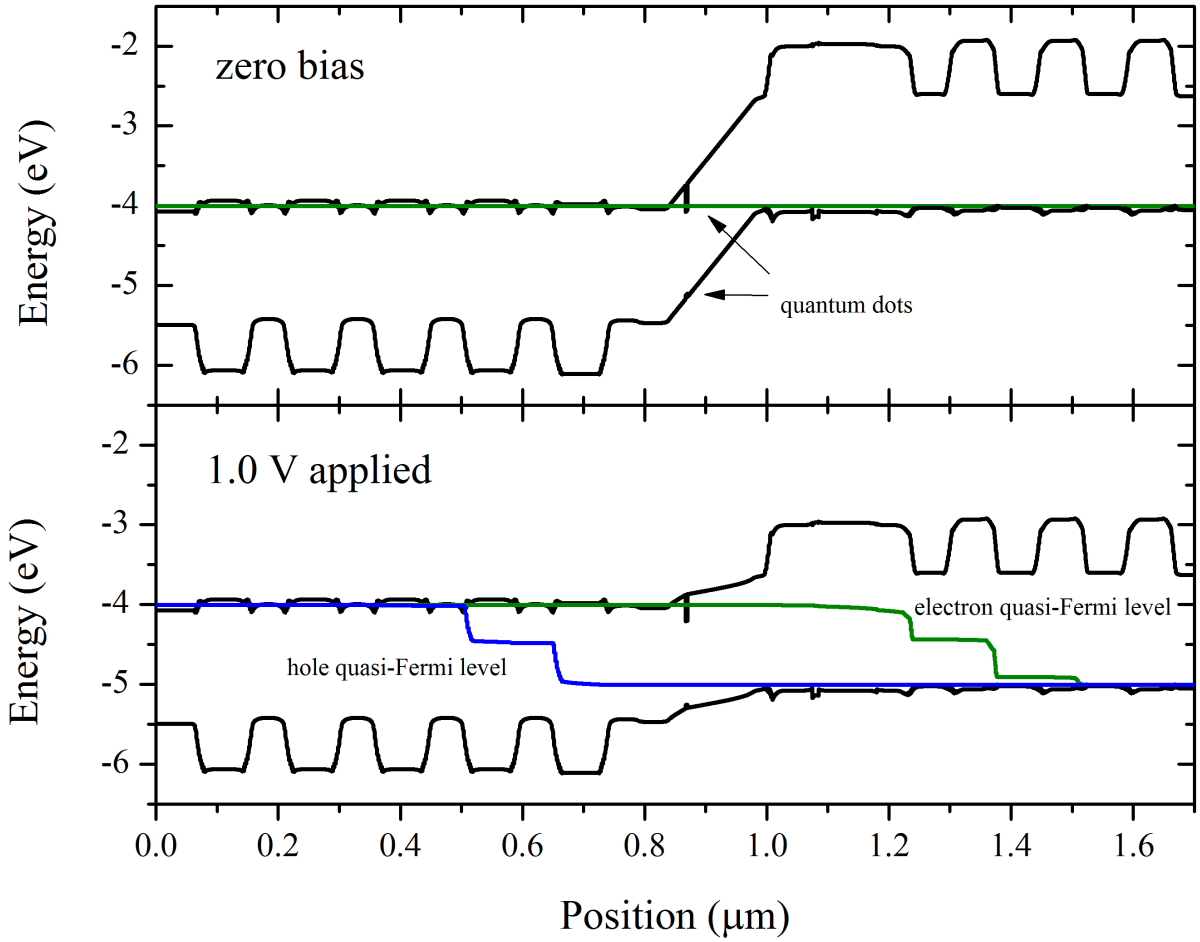

Figure 3.7: Band diagram of a microcavity device. With a bias applied, the bands are flattened. The quasi-Fermi levels for the electrons and holes are modified with an applied bias.

observe them with photoluminescence [90].

In a device, quantum dots are embedded in a p-i-n junction. As a result, there is an initial built-in electric field, and the bands in the intrinsic region are tilted. As a voltage is applied to the device, the resonance frequency of the quantum dots tune through the quantum confined Stark effect. An electric field polarizes the exciton in the dot, producing a Stark shift leading to a reduction in energy at high field [91]. Around the cavity region, between n and p-doped contacts, the band diagram is shown in Figure 3.7. The band diagram is simulated using SimWindows. The top diagram is the zero

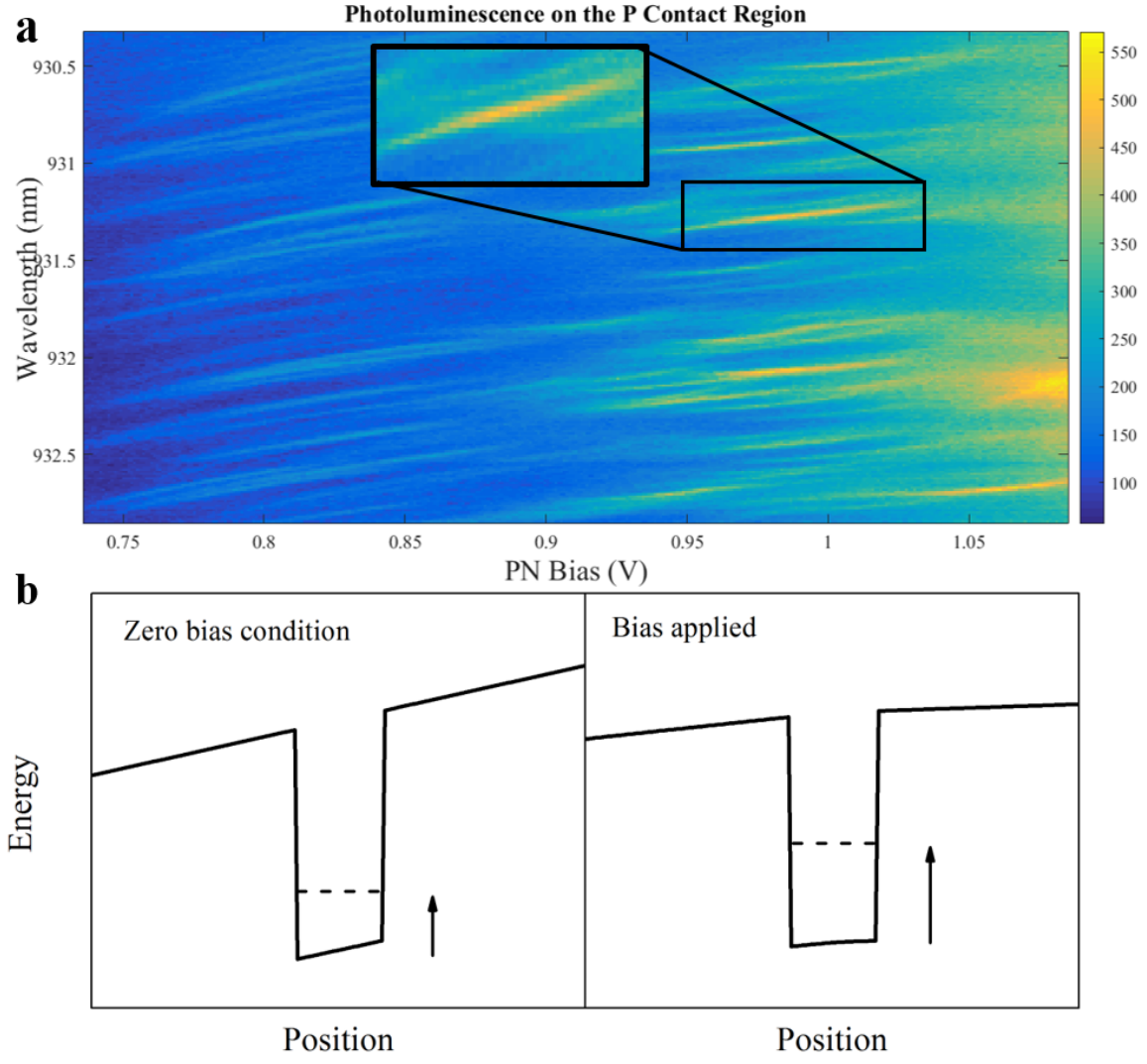

Figure 3.8: Quantum confined Stark tuning of quantum dots in a p-i-n device. At low powers, individual dots can be identified. Quantum dots are visible from 0.75 V to 1.1 V. At 0.9 V, the transition from the neutral state to the singly-charged state is apparent. Above 1.1 V, strong background luminescence is visible.

bias condition, showing the tilting of the bands in the intrinsic region from the built-in electric field. The bottom diagram shows the simulation with 1.0 V applied to the device in forward bias. The electric field at forward bias is reduced, resulting in flatter bands. The quasi-Fermi levels of the electrons and holes are shown in green and blue respectively. Biasing the device splits the levels in the intrinsic region; the electron level lies closer to the conduction band while the hole level lies closer to the valence band.

In Figure 3.8, the photoluminescence spectra is measured for dots in an electrically tunable device. The top mirror is etched away, exposing the p contact. Light is incident on this region. Multiple dots can be identified, along with their tuning behavior. Typically, a high density of dots is grown, which makes identifying isolated dots difficult. By pumping at low powers, nevertheless, individual dots can be resolved. The sample is excited with a few nW, with a 635 nm Fabry-Perot laser. In a p-i-n device, carriers rapidly tunnel out of the quantum dots from the built-in electric field. The bands must be flattened to trap carriers long enough to recombine. In this sample, this voltage occurs at above 0.75 V, where individual dots can be identified. Their energy is shifted higher as the voltage is increased, which is expected from the quantum confined Stark effect.

As the bias on the device increases, the quantum dot can be occupied with electrons or holes. The quantum dots are positioned close to the n contact. From Figure 3.7, it is apparent the electron Fermi level can reach the confined electron states of the quantum dot. The separate set of transitions above 0.9 V is attributed to charging of the dots with a single electron. An energy shift is observed due to the Coulomb blockade. Eventually, tunneling of carriers, and high currents through the device, cause the transitions to disappear, and strong background luminescence is observed. If positioned closer to the p-doped region, holes will be trapped in the quantum dot. Electron and hole spins in quantum dots have important applications in quantum information, which are beyond the scope of this work. A review is given by Warburton [92].

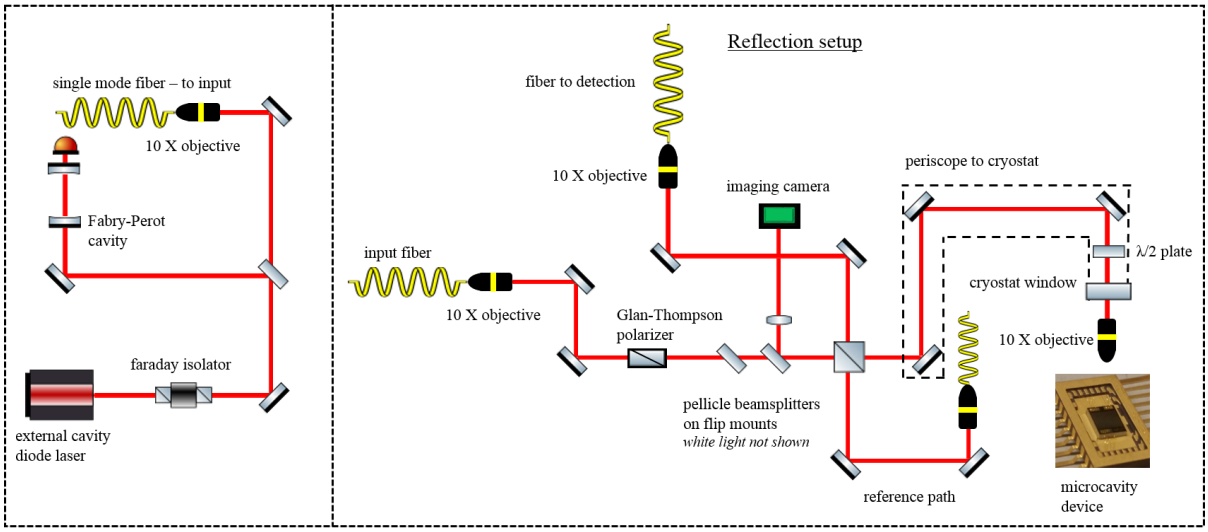

Figure 3.9: Optical setup for reflection measurements on microcavities. The laser is shown on the left. The frequency tuning is calibrated with a Fabry-Perot interferometer. The light is coupled to a single mode fiber and sent to the experiment shown on the right. Light is collected in single mode fibers, for both the reflection signal and the laser reference at the beam splitter. Fiber coupled detectors measure the collected light.

3.3.2 Reflection Measurements

Figure 3.9 shows the optical setup configured to perform resonant reflection measurements. A narrow linewidth tunable laser is needed. An external cavity diode laser is often used. The scanning range can be calibrated with a 1.5 GHz Fabry-Perot cavity. The light is polarized with a Glan-Thompson polarizer. The polarizer must be aligned horizontal or vertical to the table, as the periscope will introduce significant polarization rotations if the incoming light does not align exactly in s or p orientations of the mirrors. The periscope optics are aligned to keep reflections at a 90° angle. A $\frac{\lambda}{2}$ waveplate is placed directly above the cryostat window to rotate the exciting polarization. Reflected light is collected, after being separated by a 90:10 beam splitter, in a single mode fiber and directed to a silicon avalanche photodiode. The first reflection from the beam splitter is collected into a fiber and used as a reference to monitor the laser.

As the quantum dot resonance is tuned through the cavity, the reflection spectrum

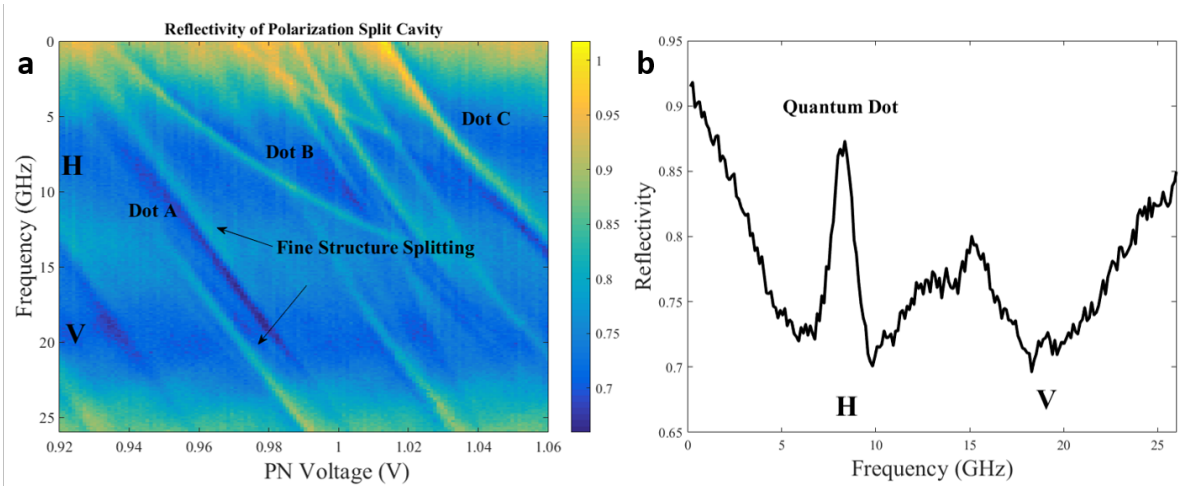

Figure 3.10: (a) A typical reflection spectrum with bias on the x-axis. The measurement is performed 45° with the cavity axis. The fine structure splitting is identified in Dot A. Parabolic tuning behavior is evident in Dot B, which occurs near the flat band condition in the device. (b) A cross section at the voltage of Dot C.

is modified according to the destructive interference induced by the Purcell enhanced quantum dots. A peak appears in reflection in the vicinity of the normal cavity dip. In our system, the cavity width is greater than the linewidth of the quantum dot, and the lineshape closely mimics the lineshape of the quantum dot itself. A relatively high quantum dot density is grown in order to increase the probability of finding a single quantum dot. Micropillars can be deterministically fabricated around quantum dots by performing lithography at cryogenic temperatures after observing photoluminescence [93].

Figure 3.10 (a) shows a typical reflection spectrum of a cavity as quantum dots are tuned with an applied voltage. The measurement is performed with the incoming light at 45° with the cavity axes. The dark blue horizontal areas correspond to the reflection dips of the polarized fundamental cavity modes. The cavity displays a polarization splitting of about 12 GHz. Such is a typical value of the polarization splitting for oxide aperture microcavities. The cavity modes are denoted H and V.

Multiple quantum dots appear in the spectrum, each indicated by a peak as they

tune through the cavity. Three of the dots are pointed out here, indicated in Figure 3.10 by A, B, and C. Quantum dot A, near 0.96 V, displays a visible fine structure splitting, which is closely aligned with the cavity, but slightly off axis. As it is tuned through mode H, one transition is prominent and the other transition shows up in mode V. There is some light from both transitions, which couples to the opposite mode because the dot is not aligned perfectly with the cavity. The dark blue is the result of a Fano-like lineshape from the dot. The energy shift due to the quantum confined Stark effect often produces a parabolic shape [91]. The shape is evident in quantum dot B. Typically, this feature appears at higher voltages, closer to the flat band condition. Quantum dot C has a strong coupling to the H cavity mode. A cross section at 1.04 V, showing the Purcell enhanced emission of quantum dot C, is given in Figure 3.10 (b).

3.4 Conclusion

Chapter 3 presents the primary characterization measurements performed on quantum dot samples. Electronic states of quantum dots are verified both with photoluminescence and high-resolution reflection measurements. There are two key aspects presented in this chapter, which are pertinent for the rest of this thesis. First, quantum dots exhibit fine structure splitting from the electron-hole exchange interaction, which gives neutral quantum dot transitions a linear polarization. Second, the quantum confined Stark effect is needed to fine tune the quantum dot into resonance with the cavity. The linear polarization of the quantum dots allows incident photons to receive a polarization rotation. The use of the quantum confined Stark effect represents a method of fine tuning, which is needed for microcavities with a high quality factor. The control method imposes a significant source of birefringence, discussed in the following chapter. A second fine tuning method, to compensate for the birefringence, is presented in Chapter 5.

Chapter 4

Design and Fabrication of Micropillar Cavities

Semiconductor microcavities are remarkable in that they greatly increase collection efficiency and enhance the light matter interaction with the embedded material. A number of methods for fabricating microcavities have been developed [94]. Here, the focus is on microcavities formed from epitaxially grown DBR mirrors. Two DBRs grown around a spacer region produce a planar Fabry-Perot interferometer. Transverse confinement is added with a selective wet oxidation. The oxide shape can be tailored from the shape of the initial etched mesa. Two patterns have primarily been developed for this work, a three-fold symmetric radiation sign, and an octagon pattern. The shape of the radiation sign turns out to be critical for fine tuning the cavity polarization, which is presented in Chapter 5. This chapter is not meant to be an exhaustive review of all optical properties of DBR mirrors and microcavities, rather an overview of the most relevant properties needed to understand birefringent effects in mircropillar cavities.

4.1 Optical Properties of DBR Cavities

A standard method of making high quality mirrors is by alternating quarter wave layers of materials with different indices of refraction. As waves propagate through the layers, they are partially reflected at each interface. When the wavelength equals twice the optical path length of each period, the condition known as the Bragg condition, the reflectivity of the mirror is very high. There exists a stop band, centered around the Bragg condition, for which light is mostly reflected. The stop band width, for the standard quarter wave design, depends primarily on the index difference of the materials. The forward and backward propagating waves couple and produce a standing wave pattern, which penetrates into the mirror.

A half wave, or integer multiple, layer included between DBR stacks creates a Fabry-Perot cavity. Light in this instance is allowed to make multiple round trip passes between the mirrors, resulting in a large standing wave in the center of the cavity. As-grown, the device is a planar cavity, exhibiting a strong quality factor for plane waves perpendicular to the wafer. Transverse confinement, here provided by an oxide aperture, greatly reduces the mode volume. Care must be taken so that the quality factor is not greatly reduced through the introduction of the aperture. The reduced mode volume, then, provides Purcell enhancement according to Equation 1.1.

Extremely high quality DBR mirrors can be grown with MBE by alternating GaAs and AlGaAs, all in the chamber, and without breaking vacuum. GaAs and AlGaAs are closely lattice matched, and can therefore be grown on top of one another relatively freely without strain or defects. The similarity in the crystal structures of GaAs and AlGaAs naturally means the two materials exhibit a similar refractive index. The reflection coefficient for the two materials is, therefore, relatively poor ($r \sim 0.08$). The result of the poor interface reflectivity is a large penetration depth of the electric field. The

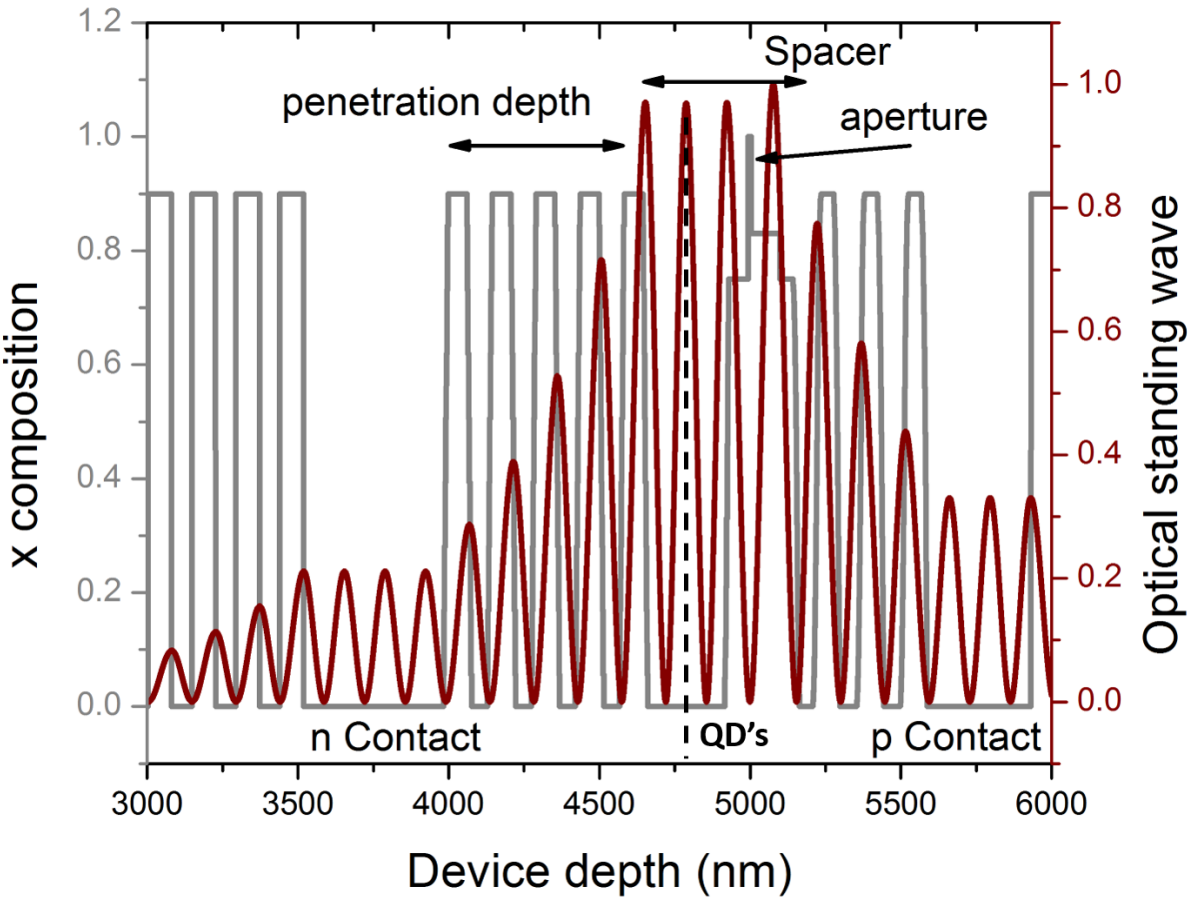

Figure 4.1: Standing wave pattern and Aluminum composition of a typical microcavity.

penetration depth has consequences, which are dealt with in Section 4.4, and is utilized to finely tune the polarization splitting. The polarization tuning is discussed in Section 5.2.

The standing wave pattern of the microcavity device is shown in Figure 4.1. The aperture is shown with the highest aluminum content in the spacer region, which is designed to sit at a node of the electric field. The quantum dots, represented by the dotted line, are located at the field anti-node. Such design follows the standard procedure of positioning the primary optical elements, those to be enhanced, at an electric field maximum. Loss is minimized by placing the aperture at a field node, where there is zero

electric field. There are two contact layers, doped n and p, which are grown thicker than the quarter wave layers in the mirrors. Growing the contact layers thicker makes etching to the layers easier and provides more reliable electrical contacts for the p-i-n structure.

DBR mirrors exhibit a strong phase dispersion, and it is directly related to the penetration depth. Incident light, as it must travel through the multiple layers, does not reflect immediately off the surface. For an incident Gaussian pulse of width, σ_0, it can be shown that the time delay, Δt, and new width, σ, are related to the phase response, $\phi(\omega)$, by [95]

$$\Delta t = -\phi' - \frac{1}{8}\frac{\phi'''}{\sigma_0^2} - \frac{1}{128}\frac{\phi^v}{\sigma_0^4} - \dots, \tag{4.1}$$

and

$$\sigma = \sqrt{\sigma_0^2 + \frac{1}{4}\frac{\phi''^2}{\sigma_0^2} + \frac{1}{32}\frac{\phi'''^2}{\sigma_0^4} + \frac{1}{16}\frac{\phi''\phi'^v}{\sigma_0^4} + \dots.} \tag{4.2}$$

The phase derivatives are evaluated at the center frequency of the impinging light. The time delay only depends on odd order derivatives, while both even and odd order derivatives determine the pulse broadening. The complex reflection coefficient of a DBR mirror can be determined by a number of methods. The standard methods are coupled mode theory, Fourier analysis, and numerical transmission matrix method (TMM) calculations [96]. The causal link between the phase dispersion and the time delay of a mirror suggests the phase slope with frequency be negative everywhere, and indeed it is.

The phase and reflection for a lossless DBR mirror are presented in Figure 4.2 for typical values of a GaAs/AlGaAs mirror. The calculation is performed with TMM, including 24 mirror periods. A single DBR mirror, around the Bragg condition, displays a linear phase slope. The wavelength is plotted on the x-axis; the slope with frequency is negative everywhere, except at the edges of the stop band where the phase has asymptotes. Light is completely transmitted at these points.

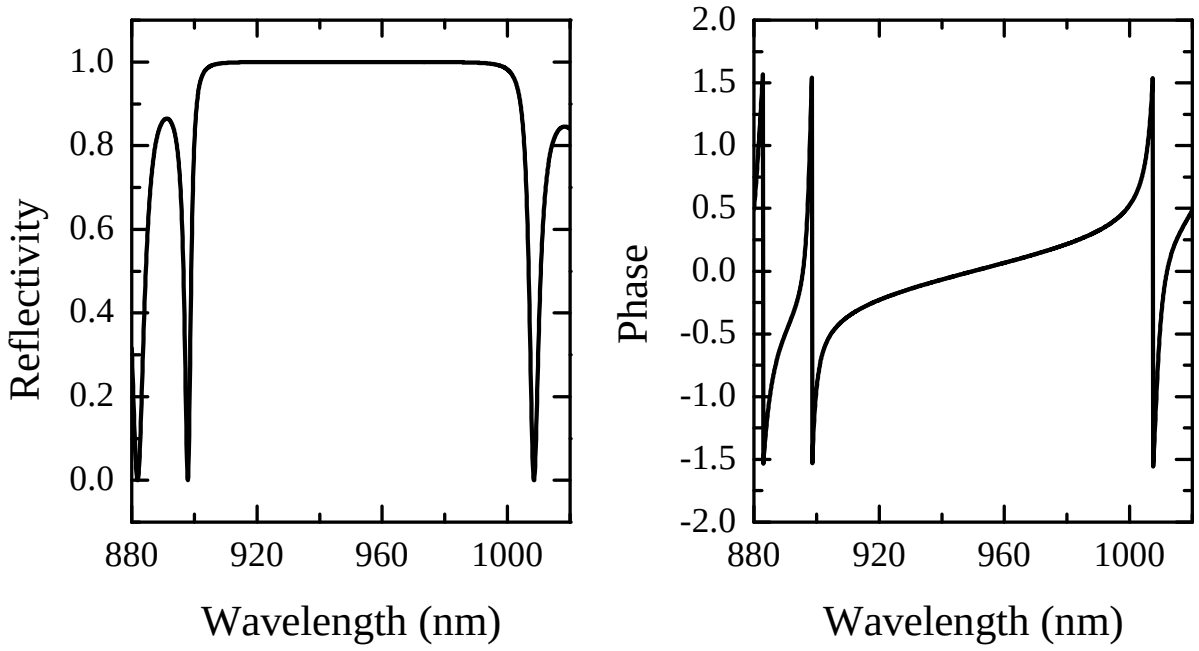

Figure 4.2: The reflectivity and phase of a DBR mirror with 24 periods of alternating GaAs and AlGaAs.

From Equation 4.1, keeping only the first term, the time delay is given by

$$\Delta t = -\phi'. \tag{4.3}$$

The time delay of reflections of a DBR mirror with relevant experimental parameters is on the order of femtoseconds, much less than the time scale of any other parameter in the system. Typically, the system is excited with picosecond pulses for resonant single photon sources. Equation 4.2 reveals that the lowest correction to the pulse width is to third order in the phase, which is negligible, around the Bragg condition. Therefore, the DBR mirrors can be treated as perfect mirrors, displaying zero dispersion, with an effective penetration depth. The penetration depth, however, can be altered by changing the Bragg condition.

Samples are grown with MBE on undoped [001] GaAs substrates. 24 mirror periods

form the bottom mirror. The bottom 13 periods are composed of GaAs and AlAs and 11 are composed of GaAs and $Al_{0.9}Ga_{0.1}As$. Exposing pure AlAs to air leads to destructive oxidation, and only the aperture region is typically allowed to be exposed by etching. After the bottom mirror, the n contact is grown, where n-doping is first added (silicon n-type dopant), followed by 5 additional mirror periods. The intrinsic cavity spacer is grown, and p-doping begins before the aperture layer (carbon p-type dopant) in the spacer. Three p-doped mirror periods, followed by the p contact layer are then grown. The top mirror consists of 22 intrinsic $GaAs/Al_{0.9}Ga_{0.1}As$ layers. Exact growth recipes are given in Reference [88].

4.2 Micropillar Fabrication

In order to complete the device, fabrication of microcavities with integrated electrical control is needed. An outline of the micropillar process is as follows: Deposit Indium Tin Oxide (ITO), etch to the p contact and the n contact layers, perform wet selective oxidation, deposit metal contacts, anneal, and package. The primary development for this thesis is the electro-optic tuning of the cavity polarization splitting. ITO deposited on the top of the device forms a Schottky contact, which can be used to apply an electric field over the top mirror. The full fabrication process is outlined here, including the ITO top contact. Exact parameters can be found in Appendix A.

ITO is desirable as a top contact as it is both conducting and transparent. Both sputtering and electron beam deposition are suitable techniques for the deposition of ITO. Electron beam deposition is used in this work. ITO deposited on substrates at room temperature is opaque, and easily removed from the device. The desired properties are obtained either by annealing, or heating the substrate during deposition. Substrate heating is unavailable if photoresist is applied, and for this work this is the case. Negative

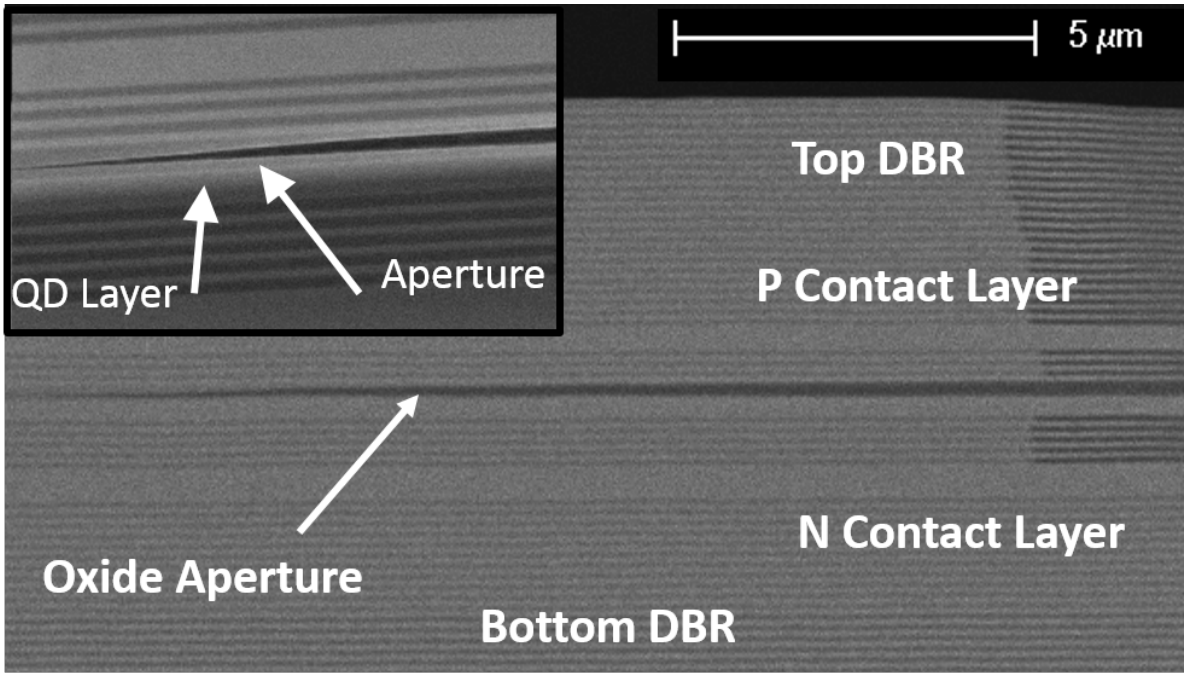

Figure 4.3: Cross sectional SEM image of a microcavity structure. The oxide aperture is the darkest layer. The p and n contact layers are visible as the thicker layers. A zoom in on the tip of the aperture is shown in the top left, which demonstrates the tapered lens design.

photoresist is patterned on the sample in order to liftoff ITO. A hot HCl wet etch, or dry methane etch, can be used for etching annealed ITO into the desired pattern.

At least two etch steps are required for the n contact and for the p contact. The etch to the n contact, for this process, has a dual purpose. It is used to access the n contact layer and to expose the AlAs oxide layer. These steps are performed in an inductively coupled plasma dry etch. A mixture of BCl_3, Cl_2, and N_2 is needed. The inclusion of BCl_3 significantly smooths the sidewalls and produces a sloping profile. The slope is tolerable for oxide aperture microcavities. Laser reflectivity monitoring is used to terminate the etch at the correct depth. Compared to air post cavities, oxide aperture cavities are much more tolerable to sidewall roughness. The optical properties are determined in great part by the aperture, thus avoiding demanding process development for the etch.

Selective AlGaAs oxidation is performed in a tube furnace with steam. The furnace

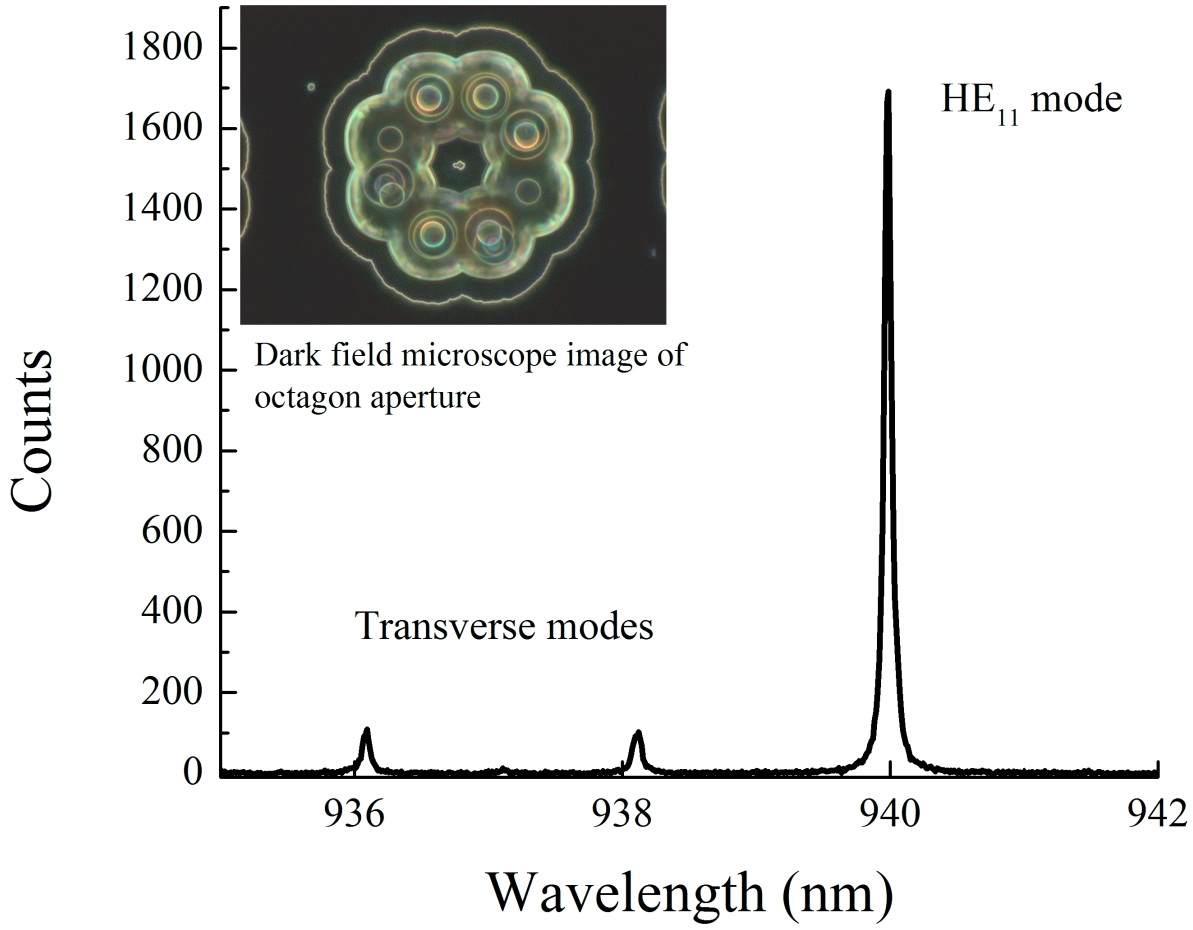

Figure 4.4: Microcavityavity photo-luminescence and corresponding dark field image of an oxide aperture. The highest peak is the fundamental HE_{11} mode. With transverse confinement, higher order spatial modes appear at higher energy. The inset is an example of a microcavity design with eight etched vias, oriented in an octagon. The top mirror is etched away to expose the aperture.

is typically heated to 420°C. A beaker of de-ionized water is heated to 85°C, and dry nitrogen is bubbled through the beaker and fed through one end of the furnace with a flow rate controller. The single layer, with the highest aluminum content in the sample, is oxidized inwards producing an aperture. A cross-sectional SEM image of a cleaved ridge is shown in Figure 4.3. Ridges are etched along with the primary samples, and placed into the furnace. The ridge is then cleaved in order to expose the aperture. The aperture appears as the darkest layer in the SEM. The aluminum content is tapered during growth, such that the tip of the aperture is thin. Growing the layer this way can reduce absorption, and it has been shown to reduce the mode volume and losses compared to a regular aperture, acting as an intra-cavity lens [97].

A typical photoluminescence spectrum of a cavity is presented in Figure 4.4. The lowest energy peak is the fundamental Gaussian mode of the cavity. Transverse confinement results in higher order Hermite-Gaussian modes, which appear at shorter wavelengths. The sample is cooled to 6 K and excited with a high energy laser. The exciting beam has a Gaussian profile, and photoluminescence is collected through a single mode fiber. Light is primarily collected from the fundamental mode. The light is sent through a grating spectrometer and imaged per the methods in Chapter 3.

The inset of Figure 4.4 is a dark field image of the aperture. The images are obtained by etching the top mirror away and imaging in a standard microscope. Aperture images can also been obtained using an infrared microscope, which has the advantage that it can be used in situ during the oxidation process [98]. A low energy light source is needed to image through the DBR mirrors because the material is highly absorbing at energies above its band gap. The limitation of infrared sources and the need to image through a thick stack of mirrors produces a poor image resolution. More information is obtainable by making higher resolution images.

Extra calibration samples are typically fabricated, allowing some to be sacrificed

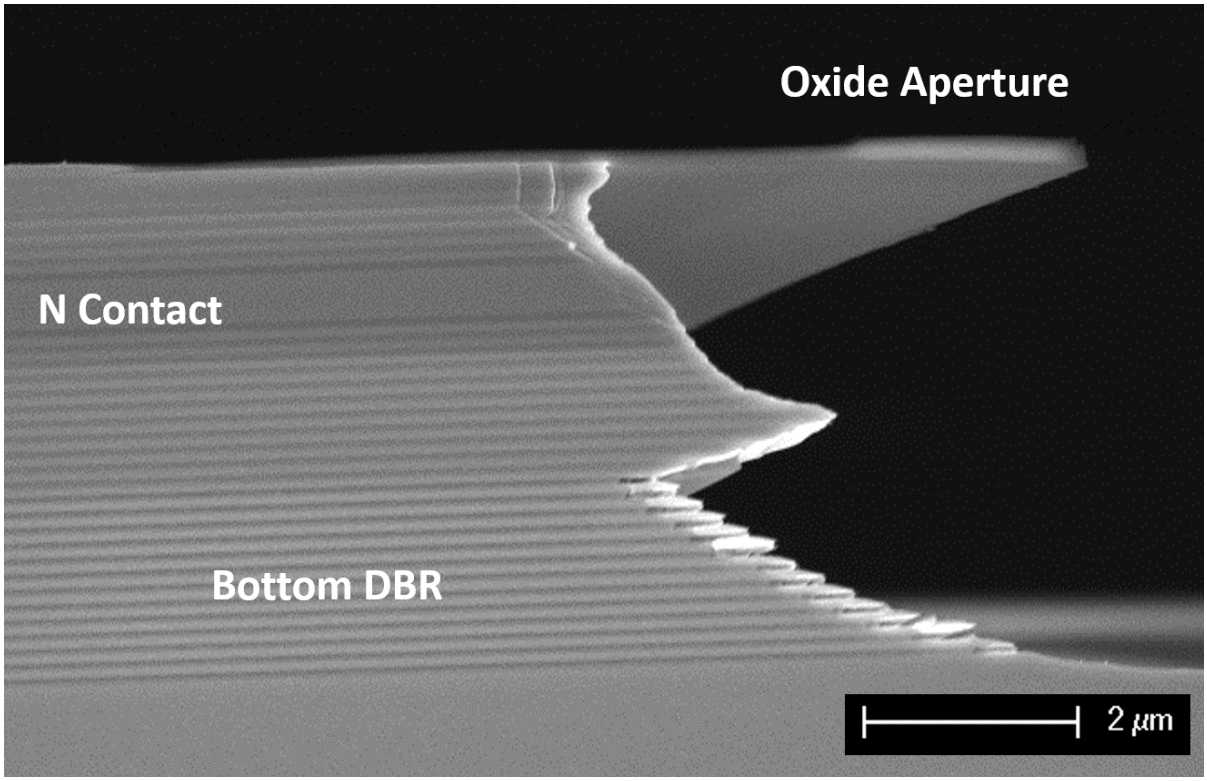

Figure 4.5: SEM cross section of an etched calibration device demonstrating the effect of the wet etch used to image the oxide aperture. The oxide is preserved, and lays partly freestanding at the top of the structure, which can be imaged in a dark field microscope. Underneath the aperture, the semiconductor layers are etched, and the transition to complete AlAs in the Bragg layers undercuts the semiconductor layers further becuase the etchant is faster for higher aluminum composition.

during processing for imaging. Oxidized calibration microcavities are wet etched in H_3PO_4:H_2O_2:H_2O, volume ratios 1:1:10, to remove the top mirror. The etchant is selective to the oxide, allowing the aperture to be preserved with a slight over etch of the mirror. The Figure 4.4 inset displays the octagon pattern, sometimes referred to as "flower power." There are eight vias etched into the mirror to expose the oxide layer. Similar patterns have been used in vertical emitting lasers [99, 100]. The remains of the bottom mirror hold the device, which are also visible in the discolored region around the vias. The edges of the aperture and the resulting outer diameter of the oxide display a high contrast in the dark field mode of an optical microscope.

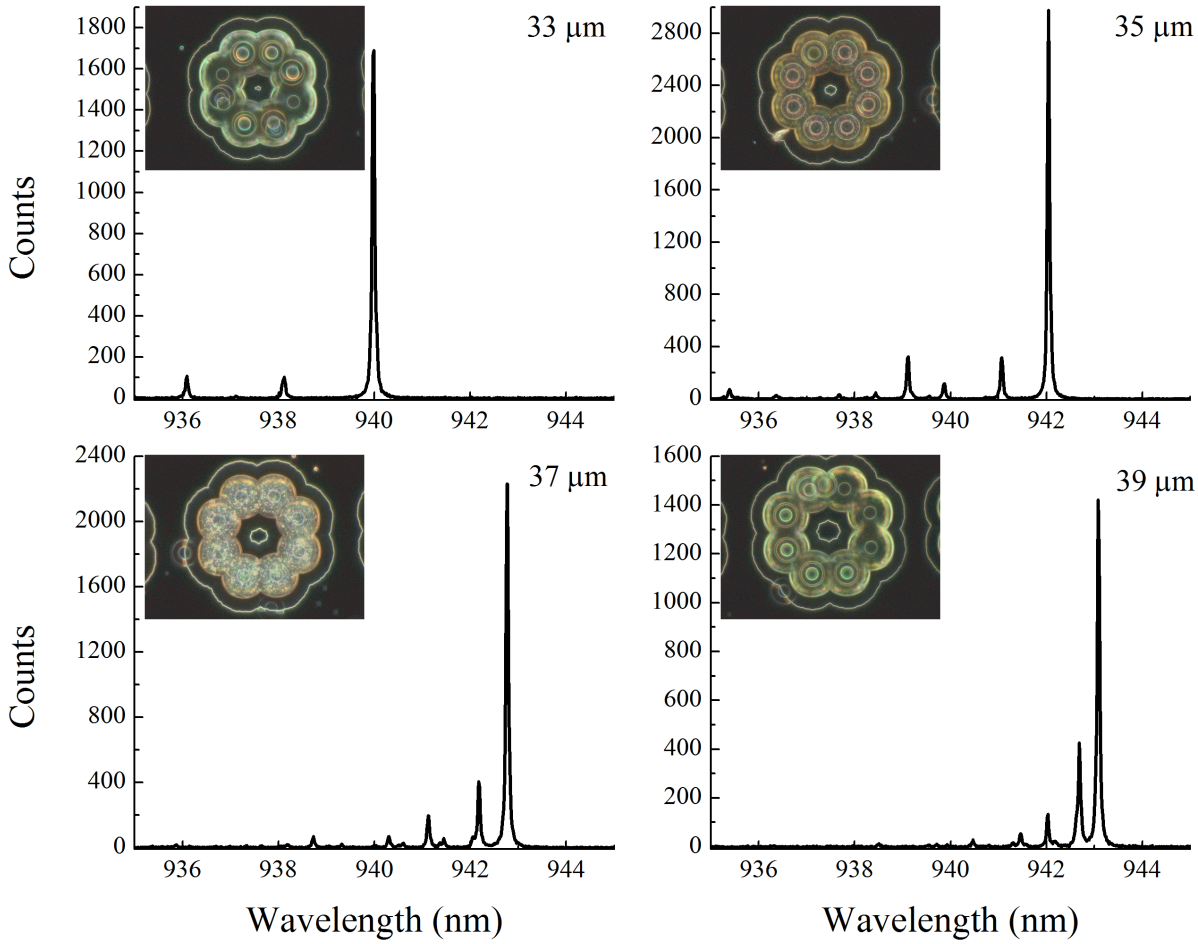

Figure 4.6: Progression of photo-luminescence spectra of multiple cavities with varying aperture diameter. The values included in each graph are the diameters of the initial mesa pattern. The transverse mode splitting increases with the smaller apertures.

A cross-sectional SEM image of an etched calibration cavity is presented in Figure 4.5. The top mirror is completely removed, and the selective etchant undercuts the aperture. On the bottom mirror, the transition to the higher aluminum content Bragg layers results in a faster etch rate, leaving a pagoda like structure.

The transverse mode confinement is directly linked to the size of the aperture. Although direct imaging is used in this work, it is theoretically possibly to reproduce all information on the shape of the aperture from the spectrum of modes [101]. Figure 4.6 displays the size dependence of the optical modes on the aperture size. The via circle

diameter is indicated in microns next to the images. As the aperture size decreases, the transverse mode splitting is bigger, indicating a smaller mode volume. The fundamental cavity mode also shifts towards higher energy as the mode volume decreases.

The oxidation rate is extremely sensitive to process parameters, including substrate temperature, water temperature, flow rate, layer thickness, and aluminum concentration [102, 103]. Oxidation times from different wafers are substantial, resulting from slight growth variations in the oxide thickness and composition. It is necessary to calibrate the growth rate, at least from wafer to wafer. For optimum results, the oxidation rate should be calibrated during every fabrication run. A number of methods can be used. The work here has relied on the methods outlined above: SEM imaging of ridges, and direct imaging of apertures after removal of the top mirror.

Three electron beam depositions are required to finish the device. Ohmic n and p contacts are needed. For depositions on ITO, it is only desirable that the metallization provide a reliable bonding pad. The metallizations developed only require one annealing step, and the order in which the metallizations are performed is not critical. For cryogenic operation, it is most desirable to bond wires to the device. A finished device is shown in Figure 4.7, which is mounted to a standard chip carrier (Evergreen Semiconductor). The carrier leads can be soldered to wires for electrical connections in the cryostat.

4.3 Birefringence in Single Photon Sources

Birefringence from crystallographic effects and aperture asymmetry, discussed in the next section, result in a finite cavity polarization splitting. Polarization splitting is typically undesirable for the operation of single photon sources. Resonantly pumped single photon sources rely on polarization rotations induced by the quantum dot. A polarizer, which blocks the exciting light, can let through photons from the quantum dot alone. Po-

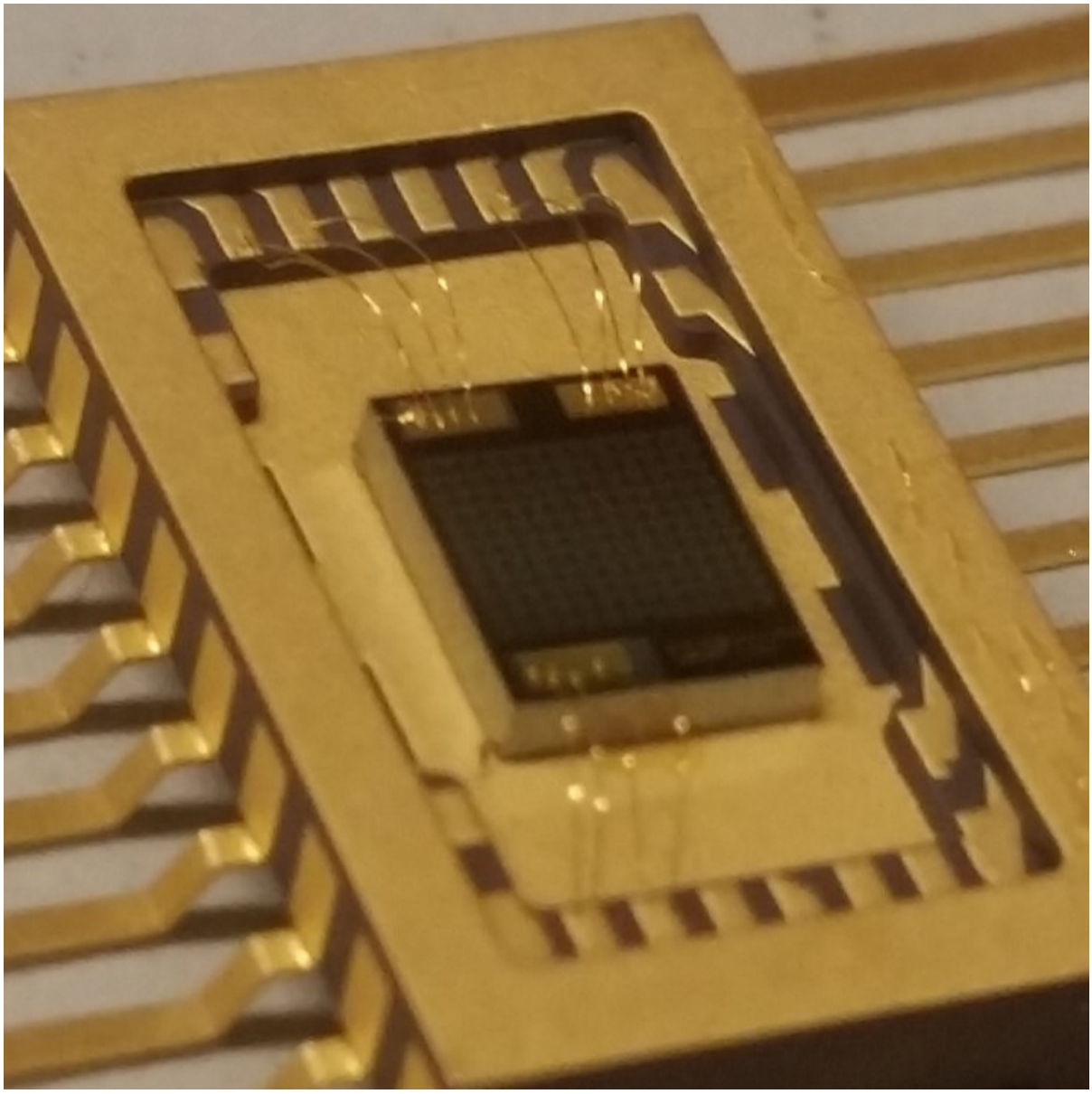

Figure 4.7: Completed device of an array of microcavities, mounted on a chip carrier (Evergreen Semiconductor). There bonding pads are used for polarization tunable devices.

larization rotation occurs only if the cavity exhibits polarization degeneracy. Otherwise, the cavity restricts excitation and emission to one polarization. With careful fabrication, cavity polarizations can be made to overlap, but rarely are the modes perfectly degenerate.

Experimentally, it is extremely difficult to block broadband light from a pulsed laser when exciting a superposition of both cavity modes. The polarized classical model, which is presented in Section 2.6, is particularly useful for studying the leaked light from exciting the system. A simulation of a cross polarized experiment with the classical model is shown in Figure 4.8. For the simulation, the cavity polarization splitting is 2 GHz. Fine tuning is generally needed to achieve a polarization splitting less than this value. κ of the cavity is 9 GHz, γ is 1.1 GHz, and g is 3 GHz. The quantum dot fine structure splitting is 4 GHz, and it makes a 30° angle with the cavity.

In Figure 4.8 (a), the cross-polarized spectrum is shown with a quantum dot and without a quantum dot. A monochromatic light source in a pure state can always be blocked by a polarizer by performing unitary rotations on the light with half and quarter wave waveplates. When a polarization splitting is present, though, there are spectrally dependent polarization rotations from the cavity. The result is the formation of *wings* in the cross polarized spectrum. For a pulsed exciting laser, the polarization splitting effectively creates a mixed polarization state of coherent driving light, which can never be perfectly isolated from the desired single photon output.

The simulated purity dependence on pulse width is shown in Figure 4.8 (b). As long as the spectral width is kept narrow a high purity is obtained. However, in order to avoid multi-photon events, the pulse should be kept shorter than the quantum dot lifetime. The exciting light is 45° with the cavity in this simulation, which represents a worst case scenario. As the quantum dot axes are generally not in a controlled direction, maximizing the brightness may require a high angle from the cavity. With the conditions presented,

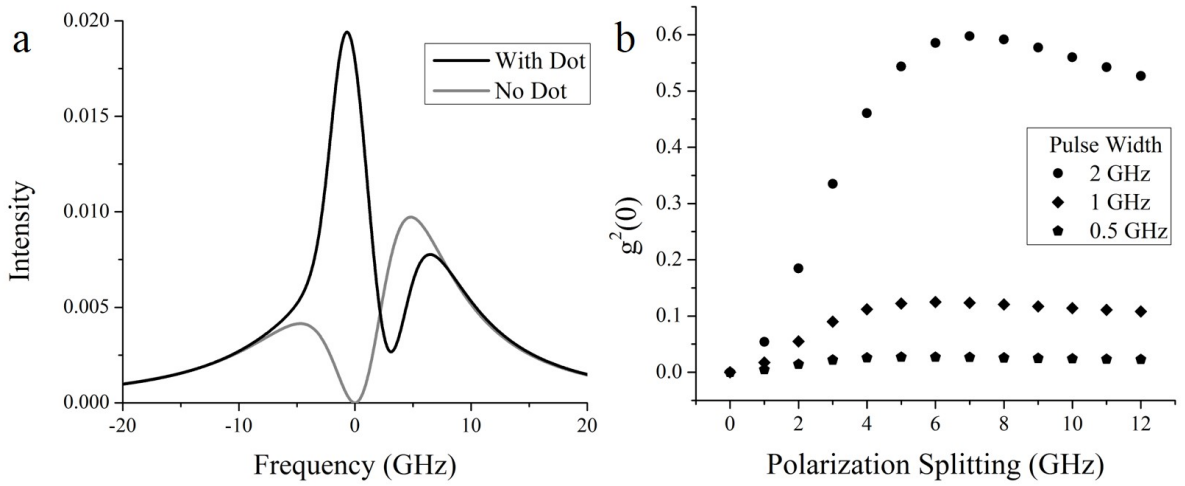

Figure 4.8: (a) Simulated spectrum of a cavity-quantum dot system, with and without the quantum dot. Polarization mode splitting produces spectrally dependent polarization rotations. (b) Simulated $g^{(2)}(\tau)$ with varying pulse widths, corresponding to the spectrum of (a). The spectral pulse width should be less than the polarization splitting in order to preserve single photon purity.

the pulse width should be kept below 1 GHz in order to allow for good extinction of the exciting laser. This would correspond to 1 nsec temporal width, which far exceeds typical Purcell enhanced lifetimes. Experimentally, it is found that exciting away from the cavity eigen-axis with $\sim$ psec pulses greatly reduces photon purity.

4.4 Electro-optic and Photo-elastic Effects

Deformation of a crystal, whether by physical stress or applied electric fields, can induce a birefringent axis not present without the perturbation. The linear electro-optic effect is presented here, as it is of paramount importance in the determination of cavity polarization splitting. The impermeability tensor, η_{ij}, which is the inverse of the dielectric constant, is represented by a Taylor series in the electric field components, E_i

$$\eta_{ij}(E) = \eta_{ij}(E) + \sum_k r_{ijk}E_k + \sum_{kl} K_{ijkl}E_kE_l. \tag{4.4}$$

r_{ijk} are the linear electro-optic coefficients, and K_{ijkl} are the quadratic electro-optic coefficients. The linear and quadratic electro-optic effects are also called the Pockels effect and the Kerr effect. A contracted notation is typically used to simply the indices, where i and j cycle through $1 \rightarrow 6$ [104]. The indices $1 \rightarrow 3$ represent components xx, yy, and zz. The indices $4 \rightarrow 6$ represent xy, yz, and zx. The symmetry of the electro-optic tensors can be directly linked to the crystal symmetry, and crystals with a center of inversion automatically have zero r_{ijk}. In the $\bar{4}$3m class, the point group for the zinc-blende structure, there is only one non-zero coefficient for the linear term, r_{41}. The tensor form is represented by

$$[r] = \begin{bmatrix} 0 & 0 & 0 \\ 0 & 0 & 0 \\ 0 & 0 & 0 \\ r_{41} & 0 & 0 \\ 0 & r_{41} & 0 \\ 0 & 0 & r_{41} \end{bmatrix} \tag{4.5}$$

The linear electro-optic effect creates a birefringence axis perpendicular to the applied field. The physical origin is the polarizability of the atoms. The lack of inversion center gives a transverse component to the polarizability, thereby producing different indices of refraction for polarizations of light propagating along the direction of the applied field. In addition to electro-optic effects, stress/strain induced birefringence can develop, as well as intimintly related piezo-electric effects [104]. The free value correction to the linear electro-optic coefficient, describing the effect of piezo-induced strain that enhances the total linear-electro optic effect, is expected to be small in GaAs [105].

In a diode structure, there are built-in and applied fields in the [001] growth direction.

For the zinc-blende structure, the principal axes are along the [110] and [1$\bar{1}$0] axes, defined respectively as the major and minor axes. After fabrication, strain fields can contribute to the polarization splitting of the cavity modes in a random direction [106, 107]. The effect of random strain fields will be revisited in Section 4.5. It is observed that micropillar cavities exhibit a strong preference for the two polarizations to align along the major and minor axes. The cause is generally attributed to the linear electro-optic effect.

In addition to crystalligraphic effects, form birefringence can develop from asymmetrical cavity shapes [108, 109]. The result can be explained by one polarization experiencing a greater transverse confinement, increasing the cavity resonance frequency more compared to the other mode. Cavity polarization splitting from asymmetric apertures is independent of the crystal structure.

Figure 4.9 shows the simulated standing wave profile and built-in electric field of a microcavity structure. The optical field is calculated with TMM, and the static field is calculated with SimWindows. A constant static field is present in the intrinsic region. Built-in fields are present at the heterostructure junctions, which arise from variations in band gap and doping. Although the built-in fields in the mirrors alternate from high to low, only one sign of the fields in the mirrors align with anti-nodes of the optical field. The interaction with the standing wave pattern has been shown to enhance the birefringence [107]. The mirror birefringence contribution to the polarization splitting is less prominent than the field in the active cavity layer, but cannot be neglected.

Polarization resolved photoluminescence is performed on a device in an unprocessed region, away from microcavities, to observe built-in birefringence. The result is shown in Figure 4.10. A forward bias of 1.0 V is applied to the device in order to keep carriers in the active region long enough to fluoresce. The planar Fabry-Perot mode exhibits a much smaller quality factor, and the light is collected in an objective, resulting in the asymmetric tail on the short wavelength side. There is a clear polarization splitting, which

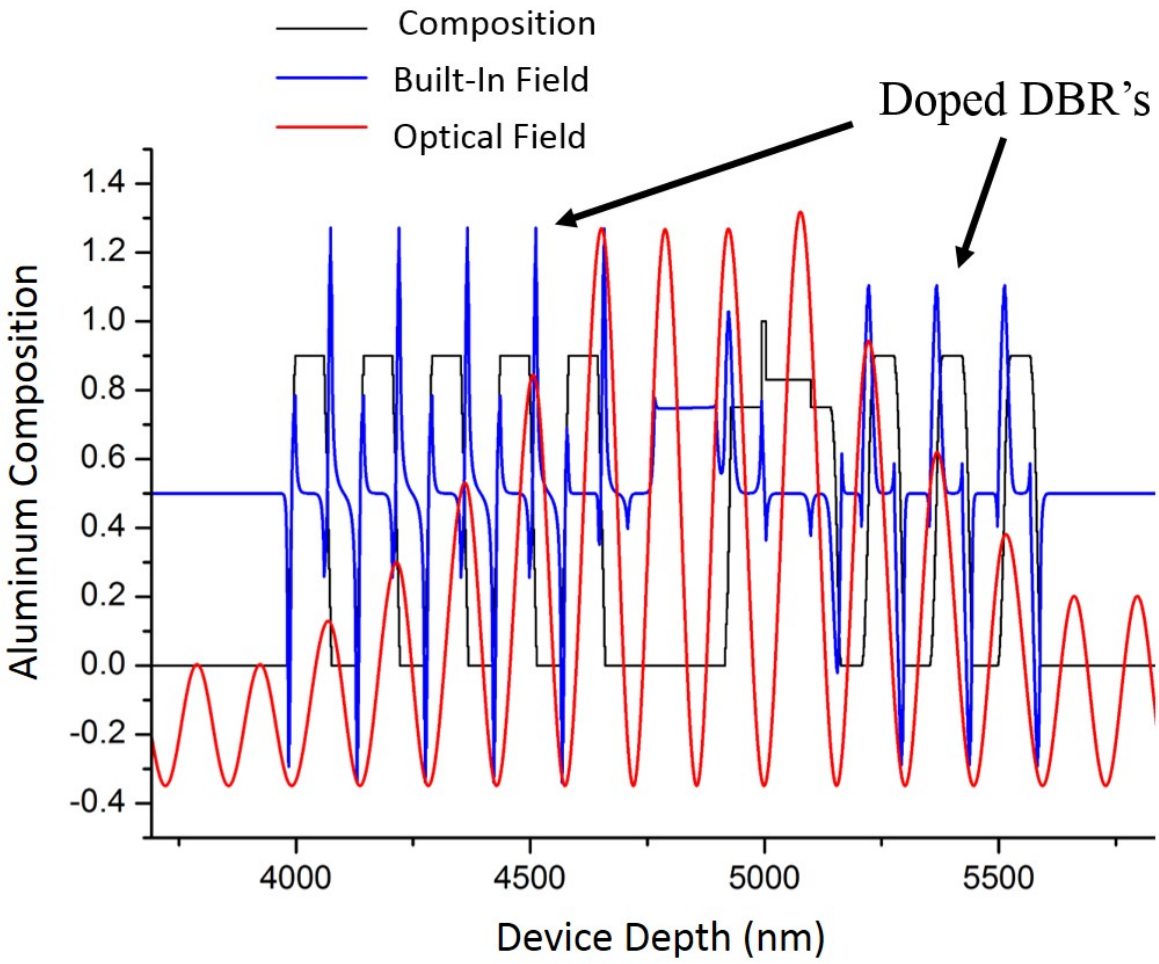

Figure 4.9: Simulation of a microcavity structure, including the built-in fields from the doped heterostructure junctions, and the optical standing wave. The standing wave overlaps only with one sign of the built-in fields, and therefore enhances the cavity polarization splitting.

is aligned with the major and minor axis. The major axis mode is at higher energy in the devices studied. The voltage dependence is difficult to study with photoluminescence because carriers tunnel out of the device. However, from 0 to 1.0 V, the polarization splitting is not greatly affected. High resolution reflection measurements verify tuning via the Pockels effect, and is discussed more in Chapter 5.

A strong position dependence of the polarization splitting on the Fabry-Perot mode is observed. The inset of Figure 4.10 shows five positions on the device over a range of $\sim$1 mm. The measurement is performed without any structures nearby on the device. The dependence of the polarization splitting on position could either be from layer thickness fluctuations during growth, or from strain induced during processing or packaging. On the device studied, there is not a clear pattern, which might indicate the source of the position dependency. Despite there being a clear dependence of polarization splitting on position, the modes never deviate far from the major and minor axes.

Second order electro-optic effects, induced by carriers (band filling, plasma...), can be applied to the device to induce birefringence [110]. However, the Pockels effect is the only prominent effect, which gives rise to birefringence transverse to the applied field. It is most convenient to place electrodes along the growth direction, which is the light propagation direction. Therefore, the Pockels effect is what needs to be considered.

4.5 Cavity Polarization Mode Coupling

The previous section was centered around isolated birefringent effects in microcavities. An additional roadblock comes from the interaction of multiple effects. Altering the form birefringence is a standard method used to account for the built-in birefringence of the cavities. In the region of small splitting, though, a polarization mode coupling can be observed from the misalignment of the form axis and the built-in axis. Polarization

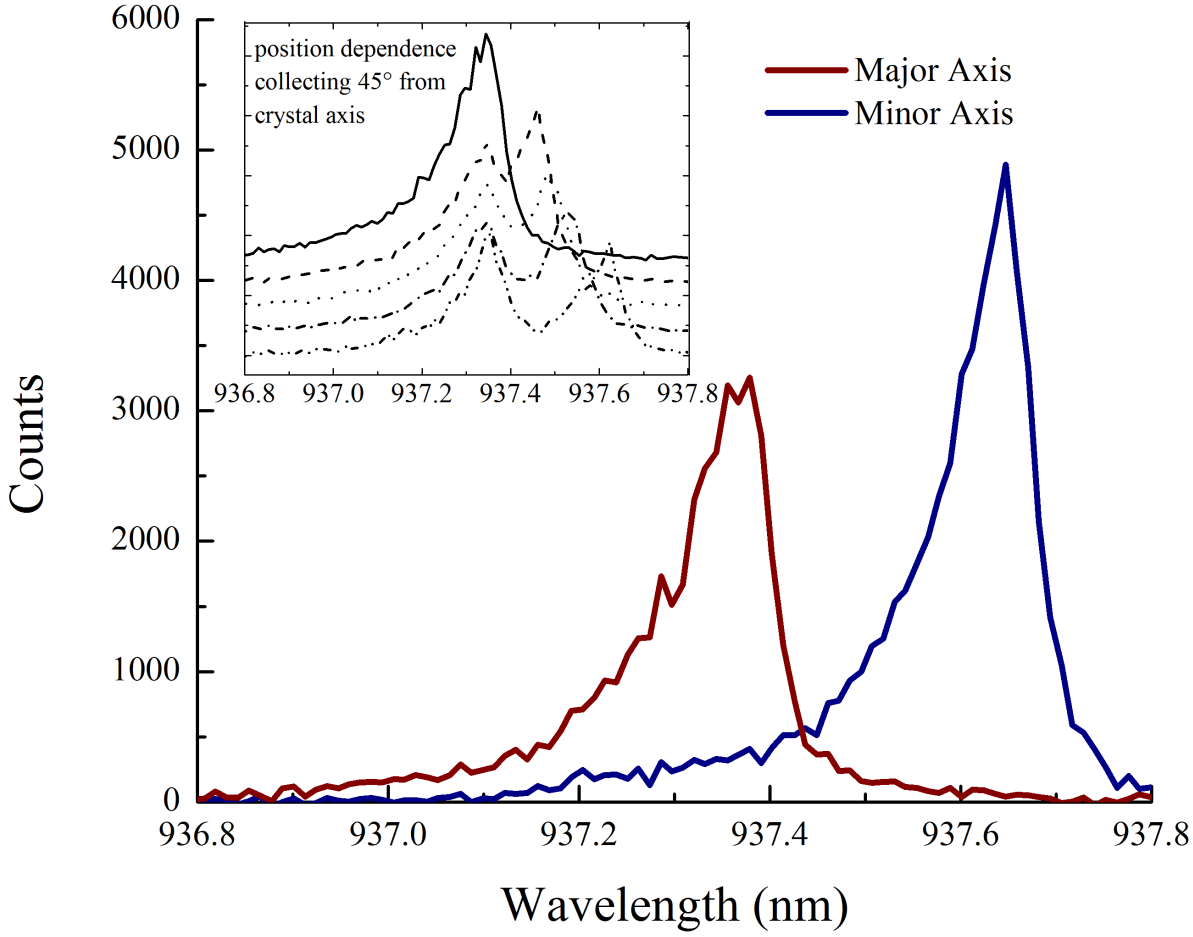

Figure 4.10: Polarization resolved photoluminescence spectrum measured on the Fabry-Perot mode. The beam is focused on the sample and collected with the same objective giving rise to a broad spectrum of transverse modes. These modes produce an asymmetric tail in the peak. The peak at higher energy corresponds to the direction of the major axis. In the inset, position dependence on the polarization splitting is shown. Although there is a position dependent polarization splitting, the two modes on the planar Fabry-Perot cavity never deviate greatly from the major and minor axes.

mode coupling has also been observed in whispering gallery resonators [111]. It is believed polarization mode coupling also explains the eigen-axis rotation with varying temperature in vertical emitting lasers [112].

The linear electro-optic effect has been shown to be a major feature of microcavities, which cannot be eliminated so far as electrical control is needed in the device. The birefringent axis, from the symmetry of the crystal, is locked to the major and minor crystal axes. Form birefringence from the shape of the aperture, or from strain fields around the cavity, can produce a less controllable birefringent axis. If the two birefringent axes are aligned, it is possible to fabricate cavities with polarization degeneracy. However, if the two axes are not aligned, the polarized modes become coupled together. The coupling leads to a rotation of the cavity axes, and prevents the modes from crossing. The observation is reminiscent of standard two mode anti-crossing behavior, described by the coupled mode formalism.

4.5.1 Coupled Mode Equations

Coupled mode equations were first formulated, in an extremely general way, by Pierce [113] to handle a variety of physical scenarios. A common example is the coupling in space of dielectric slab waveguides placed close enough in proximity so that wavefunctions overlap. A generic formalism is given by Haus [114], which is presented here. Let the parameters a_α and b_α, describe the particular modes of the structure, which here will represent the H polarization and V polarization of the cavity. A dependence of $e^{-i\beta z}$, for a propagation constant β, can be assumed. The coupled mode equations for two modes

are

$$\begin{aligned} \frac{da_1}{dz} &= -i\beta_1 a_1 + g_{12} a_2 \\ \frac{da_2}{dz} &= -i\beta_2 a_2 + g_{21} a_1, \end{aligned} \tag{4.6}$$

where g is the coupling constant (g is also used in this work to denote vacuum Rabi splitting).

Situations where power flows co-directionally allow the coupling constant components to be related by $g_{12}g_{21} = -|g_{12}|^2$. Equations 4.6 can be solved for the new propagation constant

$$\beta = \frac{\beta_1 + \beta_2}{2} \pm \sqrt{\left(\frac{\beta_1 - \beta_2}{2}\right)^2 + |g_{12}|^2}. \tag{4.7}$$

Without coupling, Equation 4.7 reduces to $\beta = \beta_1$ and $\beta = \beta_2$, the isolated propagation constants of the two modes. When $|g_{12}|$ is comparable to $\left(\frac{\beta_1 - \beta_2}{2}\right)$, the two modes couple to each other, resulting in anti-crossing.

If two birefringent axes are aligned in the same direction, $g = 0$. In VCSELs, fabricated by proton implantation, the interaction of strain and magnetic fields with a native birefringence was studied in the coupled mode framework [115]. Mode coupling strengths of $\sim$1 GHz with corresponding rotations were found. Strain was induced by using a focused laser to create a hot spot next to the cavity, effectively pulling it in one direction.

4.5.2 Experiments

Mode coupling of up to 10 GHz is observed with cavities formed by an octagon pattern of vias. Arrays of micropillars are fabricated, which step in diameter in one direction and ellipticity in the other. The sample is oriented along the major axis. Across a single row, the minor axis dimension is held fixed, and the major axis dimension is changed. The

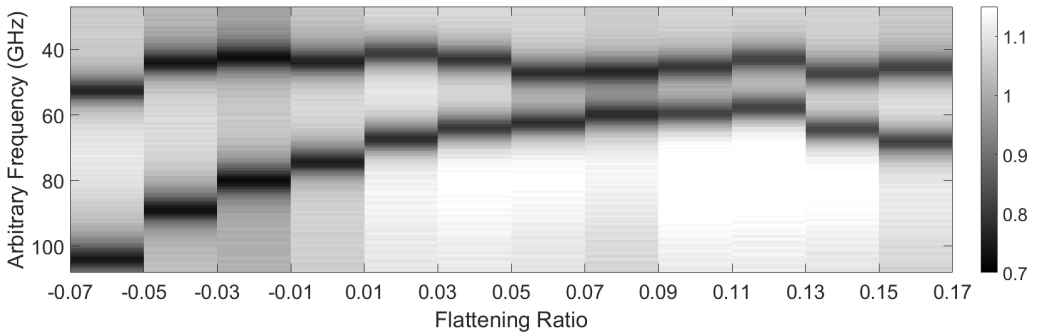

Figure 4.11: Reflection spectra of multiple cavities, with frequency on the y-axis, and the flattening ratio on the x-axis. The data is taken with the incoming light at 45° with the eigen-axis of each cavity, which are not the crystal major and minor axes.

major axis dimension is determined by a fixed flattening ratio, f_{ratio},

$$d_{maj} = d_{min}\left(1 + f_{ratio}\right), \tag{4.8}$$

where d_{maj} and d_{min} are the diameters along the major and minor axes respectively. The rows are referenced by their d_{min} dimension. For $d_{min} = 31$ μm, the reflection spectra is shown across a single row in Figure 4.11. The measurement is performed at 45° to observe both polarizations. An anti-crossing is observed for $f_{ratio} \sim 0.08$.

Figure 4.12 shows the polarization splitting with varying f_{ratio} of multiple rows. The frequency splitting never crosses zero, and the smallest apertures have the largest minimum splitting. It is typical that cavities, with the minimum splitting for each row, move diagonally across the sample as the overall size of the apertures change. In Figure 4.12, this is evident by observing that the smallest splitting for each row moves to more elliptical cavities as the apertures get bigger. It is expected that larger apertures exhibit less form birefringence, which supports this observation. The center frequency of each cavity is obtained by fitting a Gaussian function around the dip of the measured reflection spectra. The spectra are obtained with a widely tunable Titanium Sapphire laser

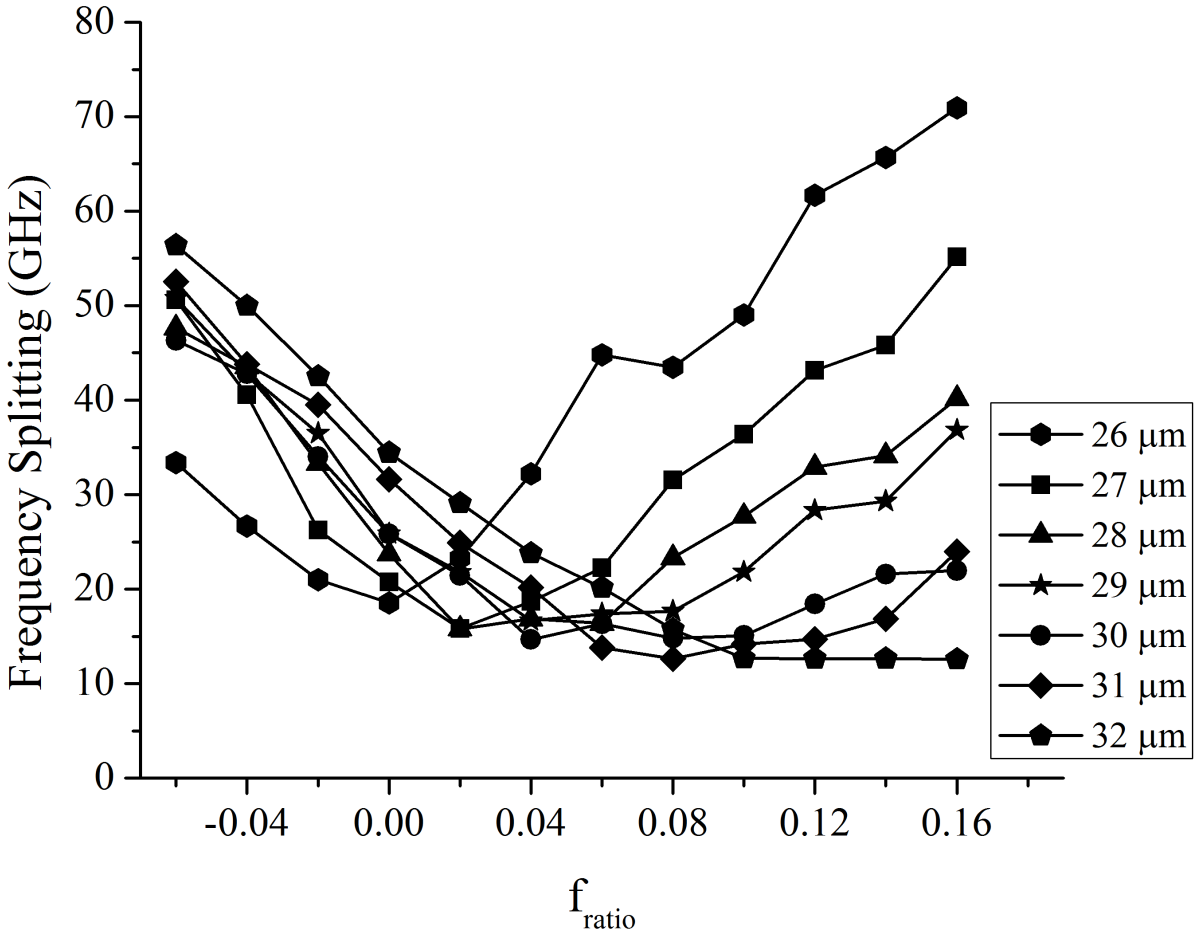

Figure 4.12: Polarization splitting of the fundamental mode of multiple cavities. The smallest cavities display polarization mode anti-crossing with zero ellipticity, and display the largest coupling strength. The larger apertures consecutively increase in the flattening ratio observed for the maximum coupling strength, and the maximum coupling strength decreases.

(MSquared Solstice). The laser scanning mode used in this experiment produces coarse frequency steps, and final spectra are smoothed before fitting.

Figure 4.13 demonstrates the rotation of cavity polarization directions observed for the same array of cavities. A non-zero polarization splitting doesn't alone demonstrate polarization coupling. In the regime of small polarization splitting, the cavity modes should be a linear superposition of the uncoupled eigenmodes. This is evident as the cavity axes rotate, with the most drastic changes at the minima of the curves in Figure 4.12. The largest apertures exhibit the smallest effect, while the smallest apertures complete a nearly 90° rotation. The cavity axes are read off from a half wave plate when aligned 45° with both modes.

Figure 4.14 shows dark field images of four apertures. The imaged samples are from a separate die of an identical fabrication run. Both samples were oxidized in the furnace together. The images demonstrate the control in ellipticity by varying the via pattern. Images are presented here of the $d_{min} = 28\ \mu m$ (top) and $d_{min} = 32\ \mu m$ (bottom) rows. The flattening ratios are $f_{ratio} = -0.04$ (left) and $f_{ratio} = 0.04$ (right). Crystallographic effects in the oxidation can produce apertures with four fold symmetry, especially in layers containing a high Aluminum concentration [116]. Close examination of the aperture shapes, however, does not reveal such effects, suggesting that the shape of the apertures in this study are primarily dominated by the via pattern. It is expected that longer oxidations would produce apertures with a diamond shape.

In order to relate the measured g to the size of the apertures, the cavities with the least splitting in each row are plotted versus their transverse mode splitting (fundamental to first order), obtained via micro-photoluminescence. g is estimated by the measured frequency splitting of cavities exhibiting the smallest frequency splitting of their row. Figure 4.15 shows the dependence of g on the transverse mode splitting for two arrays on the sample. There is a significant difference in the average g for each array, indicating a

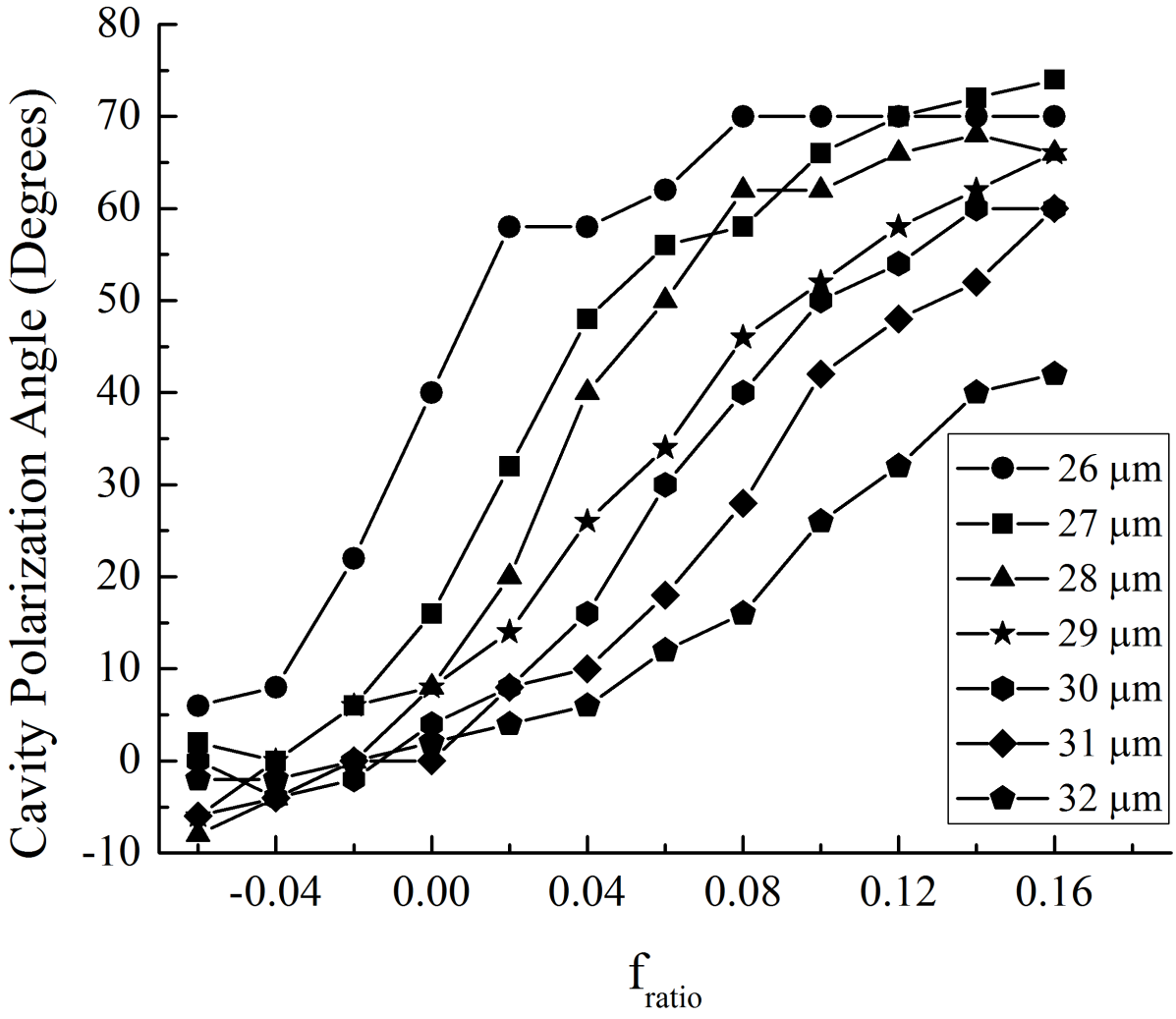

Figure 4.13: Cavity polarization angle versus flattening ratio. The maximum slope of each curve corresponds to the minimum frequency splitting in each curve of Figure 4.12.

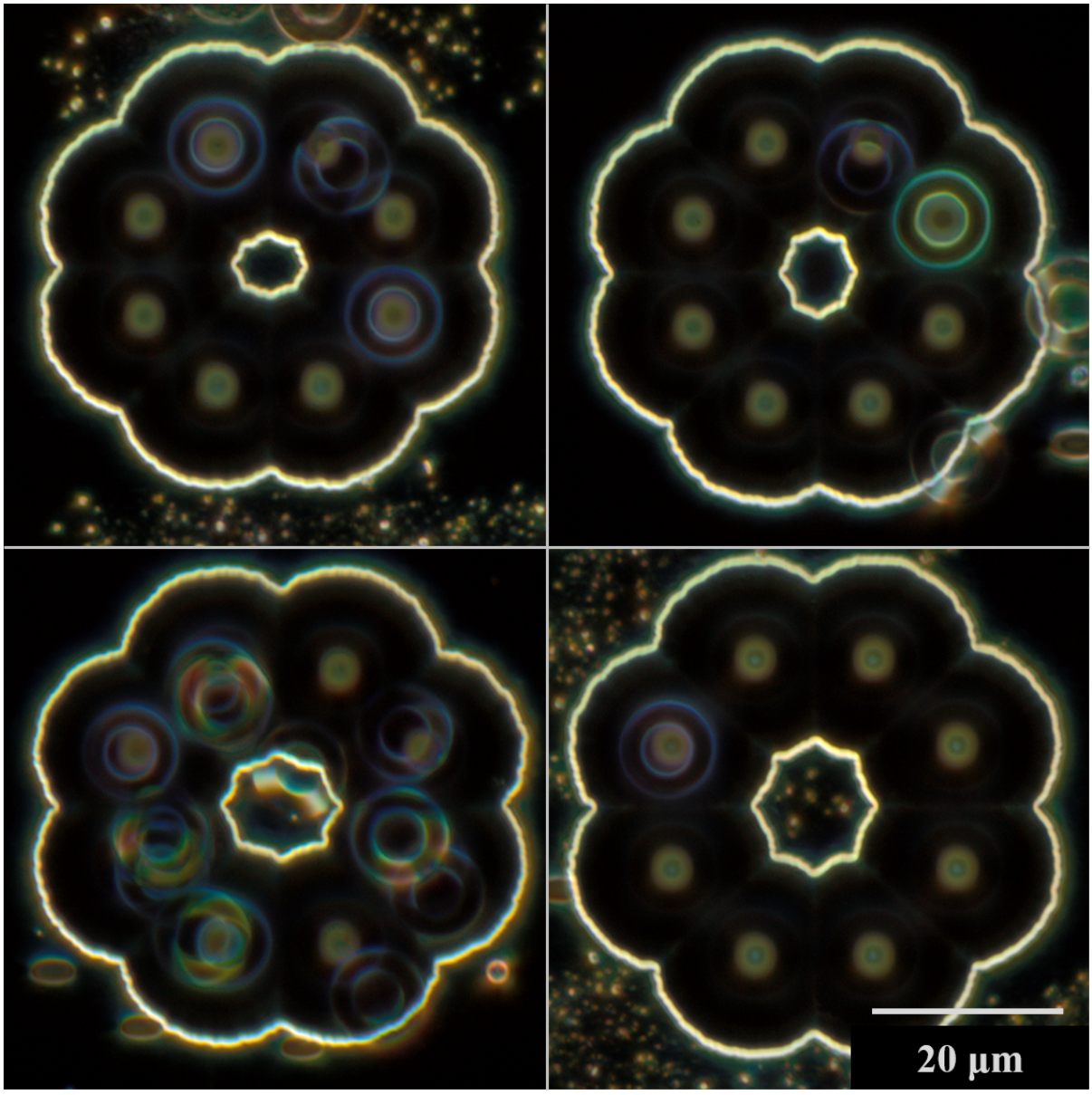

Figure 4.14: Dark field images of oxide apertures. Top left: $d_{min} = 28\ \mu m$ $f_{ratio} = -0.04$. Top right: $d_{min} = 28\ \mu m$ $f_{ratio} = 0.04$. Bottom left: $d_{min} = 32\ \mu m$ $f_{ratio} = -0.04$. Bottom right: $d_{min} = 32\ \mu m$ $f_{ratio} = 0.04$.

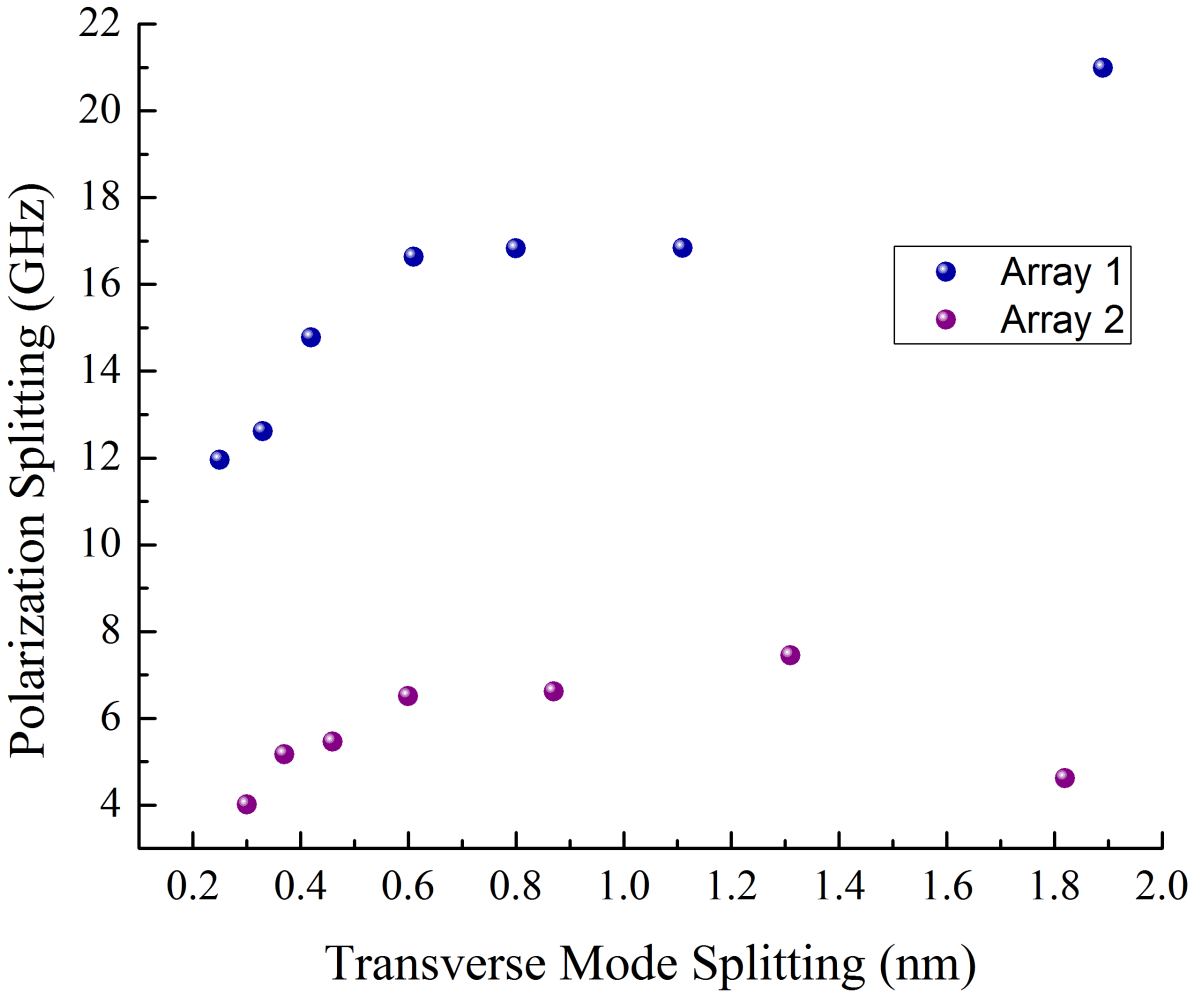

Figure 4.15: Size dependence of the coupling strength in terms of transverse mode splitting. Two arrays on the device are measured, and they produce significantly different overall mode coupling strength, and different dependency on size. The error bars for each point are smaller than the circles.

systematic difference between them. There is a general upwards trend, obeyed by both arrays, with decreasing size. However, the behavior of the smallest cavities is significantly different. The general upward trend is continued in Array 1 for the smallest cavity. In Array 2 the smallest cavity actually contains the second to smallest g of the group.

In order to confirm the presence of both form and electro-optic birefringence, polarization coupling is shown by varying the p-i-n junction bias. The tuning range is relatively small compared to varying the aperture shape. Figure 4.16 presents the mode splitting of the cavity fundamental modes as a function of voltage. Complete mode coupling behavior is difficult to observe from a single cavity, as the Pockels tuning is too small to observe the complete rotation curve. It is found, by looking at three adjacent cavities, that the Pockels tuning switches sign. The cavities are resolvable from -6 V to 1.4 V. The cavity in (a) displays a negative tuning slope with voltage. In (b), an anti-crossing curve can be barely resolved, where the modes are maximally coupled. In (c), the slope is in the opposite direction. The reflection spectrum with electro-optic tuning for the maximally coupled cavity is given in (d) to show the polarization rotation. The spectrum is measured at a single waveplate angle, and the polarization rotation is observed as a change in depth of the two modes relative to each other. The rotation angle in this measurement is about 45 degrees.

4.5.3 Discussion of Results

It was noted in Section 4.4 that strain fields can lead to birefringence away from the major and minor axes. Evidence of transverse strain in the device was presented as position dependence of the Fabry-Perot polarization splitting, although no polarization rotation was observed. By directly imaging apertures from calibration samples, it is not immediately clear that imperfections in the oxidation produce a systematic birefringent

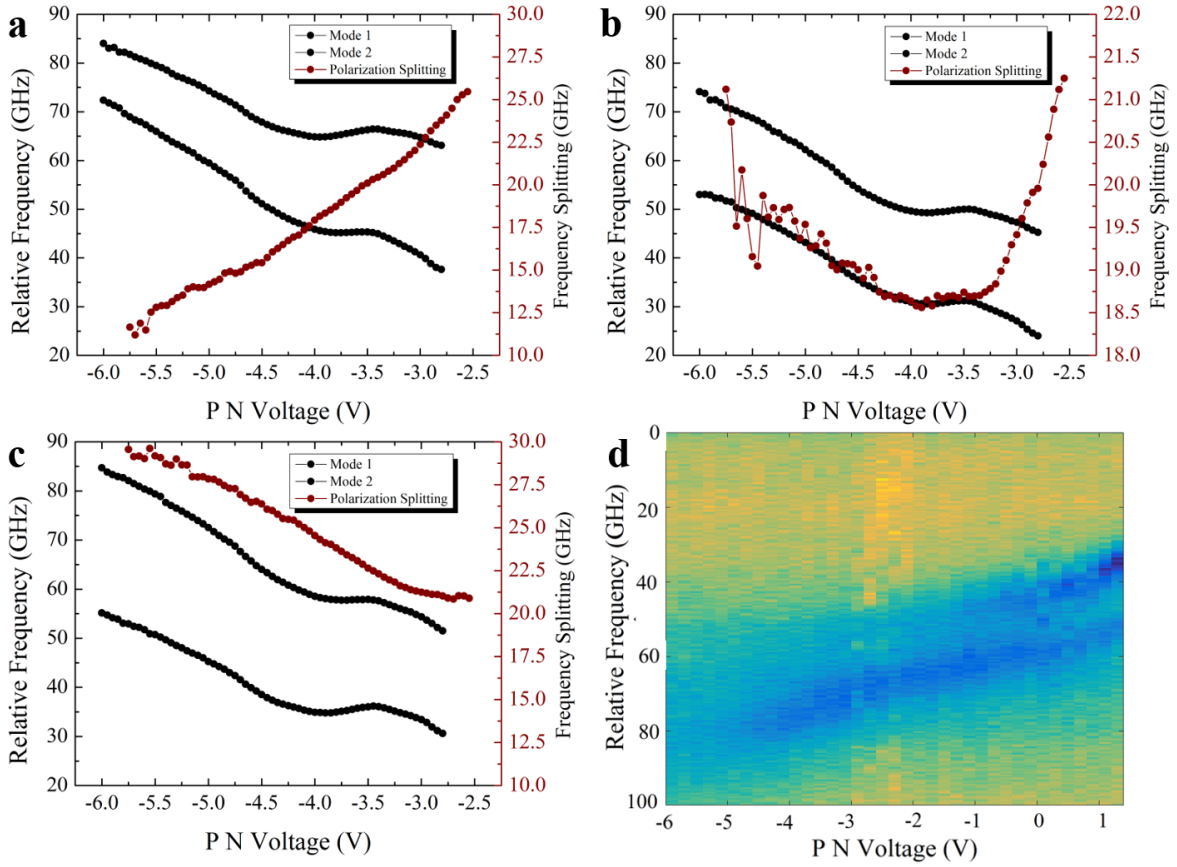

Figure 4.16: Polarization mode coupling with applied electrical tuning via the linear electro-optic effect. (a) through (c), the splitting of fundamental modes with voltage for three adjacent cavities. In (b), where the modes are maximally coupled, a relatively flat line is observed. The slopes switch direction on the cavities next to it with different flattening ratios. Visibility is limited by increased absorption as the voltage is tuned. In (d) the spectrum for the cavity in (b) is shown, which shows a polarization rotation.

axis. Further, the results for the frequency splitting and polarization rotation don't suggest a random form birefringence angle from cavity to cavity. The differences between the two arrays in Figure 4.15 further suggests a systematic component of the birefringence, which is mis-aligned with the crystal. It is also noted that a third array on the same device produces smaller polarization coupling. The dependence on transverse mode splitting is not obtained in this array because the anti-crossing point for each row cannot be clearly identified.

Although fabrication defects lead to apertures, which can be rotated away from the major and minor axis, the preference for the cavities is to align along these axes. The reason is because of the Pockels effect. The design presented is made to be as circular as possible, however, it is shown that the pattern is unstable with regards to imperfections. Even elongating the pattern in one direction leaves a significant observable mode coupling. It is desired in this work to avoid the mode coupling, however, the cavity axes could be purposfully rotated in the instance the form birefringence is purposefully aligned away from the crystal axes.

In order to have electrical control of quantum dots, an electric field must be applied across a region of the device, and a built-in doping profile will be necessary. Such requirements inevitably lead to a polarization splitting along the major and minor axis of the crystal. For high quality microcavites, which are required for single photon sources, the shape of the aperture, or mesa, must be carefully controlled so not to introduce a second birefringent axis in the device. Although producing an asymmetrical aperture may be undesirable because of increased scattering losses, purposefully creating an asymmetric aperture may be required in applications, which require strict polarization degeneracy.

4.6 Conclusion

It is clear that birefringent effects are detrimental to single photon source generation using resonant excitation and cross polarization. An electric field generally needs to be applied to a device in order to utilize the quantum confined Stark effect. Built-in electric fields and applied electric fields lead to a polarization splitting, which is always aligned with the major and minor crystal axes. The following chapter discusses fine tuning of the cavity polarization splitting with the addition of an electrical contact on top of the device. In order to use the method, the shape of the aperture must be controlled to avoid polarization mode coupling.

Chapter 5

Polarization Degenerate Cavities via Electo-Optic Tuning

In order to defeat the polarization splitting problem for quantum dot-micropillar single photon sources, an electro-optic tuning method is developed. Following the previous chapter, it is clear that crystalline effects can be detrimental to controlling the cavity polarization. A three fold triangular aperture is expected to be more robust against imperfections, avoiding polarization mode coupling. It is shown here how an additional contact on the top of the device allows fine tuning of the linear electro-optic effect. The quantum dot and the cavity polarization splitting are independently tuned.

5.1 Oxidation Through Open Mesas

The shape of the initial mesa, or pattern of vias, significantly impacts the resulting aperture shape. An open mesa shape is useful for making electrical contacts separate from the cavity. Alternatives are contacting the top of the device [117], or performing extra fabrication steps to route wires from the contact regions. Two primary ways of

forming oxide apertures have been studied in the work presented in this thesis. An understanding of the diffusion process led to the development of the octagon pattern of *vias*. The octagon pattern produces the most circularly symmetric apertures. It was revealed, however, that the shape is susceptible to polarization mode coupling from fabrication imperfections. It is therefore advantageous to sacrifice symmetry, likely at the expense of increased absorption at the aperture, in order to define the form birefringence more precisely. A number of options are available, as it is generally easy to purposefully break symmetry. A three fold pattern of arms in a radiation sign shape is discussed. The resulting apertures are triangles.

Testing of a number of mesa shapes resulted in the implementation of the radiation sign that has been used in the group for single photon sources [27]. The pattern has three arms allowing electrical access to the cavity area, without tedious fabrication steps required to contact the buried layers directly on the cavity. It has further allowed for a single contact pad to control an entire array of cavities [98]. It is conventionally expected that away from the arms, the oxide should penetrate closer to the center of the mesa. Oxidation could then "average out" the shape with increasing oxidation length.

It is first determined that the variations do not average out far into the mesa, and an extremely non-circular aperture results. The radiation pattern produces a triangular aperture after the oxidation step, which can be expected from the three fold mesa. The second observation is the orientation of the triangle is rotated from the expected orientation. The oxidation rate is enhanced along the directions of the arms, where it initially impeded because there is not a direct surface normal to this direction. To explain the enhancement, oxidation of the arms themselves must be considered. A model is proposed, which suggests that diffusion is enhanced through the arms.

Consider the initial condition of the oxidation, as steam is initially introduced. Diffusion of oxidation elements proceeds directly normal to each surface, and the initial shape

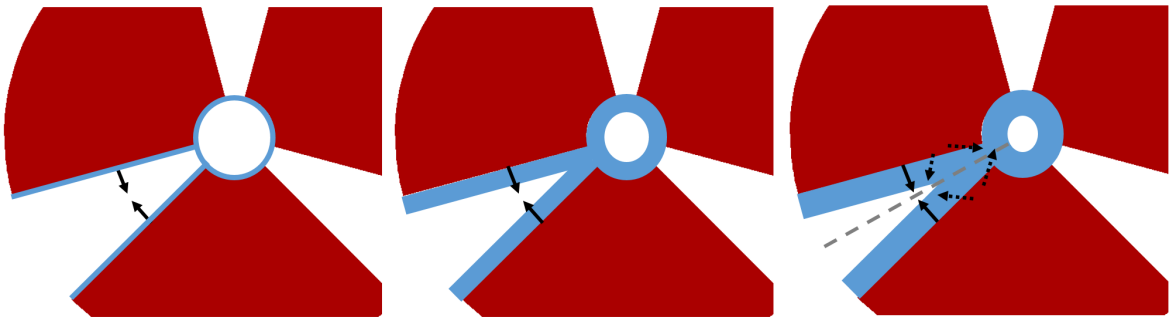

Figure 5.1: Oxide diffusion through the radiation sign. The areas in red are the etched trenches, which expose the oxide layer. The oxidation is shown from left to right, with increasing time, by the blue regions. Black arrows indicate the diffusion direction from the arms.

of the oxide should resemble the initial mesa pattern. The situation is depicted in Figure 5.1. It is apparent that the arms of the pattern become oxidized completely before the mesa. As the channel of each arm is oxidized through, the diffusion elements change direction. Considering a simple diffusion process, the high concentration at the surfaces should proceed to the area of low concentration. Initially, the direction is normal to the surface. In a planar structure, such as a ridge, this remains true. However, here, as the arms become oxidized, the direction of high concentration to low concentration is pointing towards the aperture. The arms, at this point, behave as a funnel, increasing the oxidation rate in the direction of the arms.

Experimental apertures are shown in Figure 5.2. The mesa diameters are varied from top left to bottom right. The largest mesas produce a more circular aperture, and the smallest mesas produce triangles. In the last figure, the bottom sides of the triangle are significantly oxidized more than the other directions. Variations of this kind are present often, as the epitaxy is not perfect. The particular pattern could also be the result of the onset of crystallographic dependency on the oxidation rate.

The oxidation of AlGaAs is expected to be a diffusion limited process [103]. It is further not expected to be a steady state process. It is suggested that the funneling

effect may be reduced by slowing the oxidation down, possibly by introducing less steam to decrease the diffusion rate through the device. The fast and slow directions, then, may be able to be averaged out, producing a more symmetric aperture. The implementation of smaller vias, instead of arms has proven to be a method of limiting the diffusion funnel. Future design implementations should implement a two dimensional diffusion model in order to better predict the aperture shape. A circular aperture is most desirable from a loss standpoint, as the Gaussian field pattern of the fundamental mode overlaps more with non-circular apertures at high field regions. The absorption losses are therefore expected to increase.

Improvements in geometry of the aperture, to produce more circular apertures, could be obtained by increasing the number of holes, or adding multiple layers of holes, placed further from the aperture. The diffusion funnel has been introduced so far as a detriment, however, the octagon pattern is extra susceptible to imperfections, leading to polarization mode coupling. The triangle pattern defines precisely an asymmetric axis, which are made to align with the crystal major and minor axes. Therefore, the polarization mode coupling is eliminated, and the horizontal and vertical modes can be made to cross.

5.2 Electro-optic Tuning

Even perfectly circular apertures will result in cavities with a finite polarization splitting because of crystallographic effects. Although generally small, the ever increasing quality of cavities inevitably leads to problems, as these small effects become more pronounced. Quality factors exceeding 250,000 have been reported in literature for micropillar cavities [118]. Even optimally designed circular apertures, or pillars may be susceptible to defects, strain, or imperfections in the fabrication process. Strain tuning of microcavities using laser induced defects has been used to finely tune the cavity

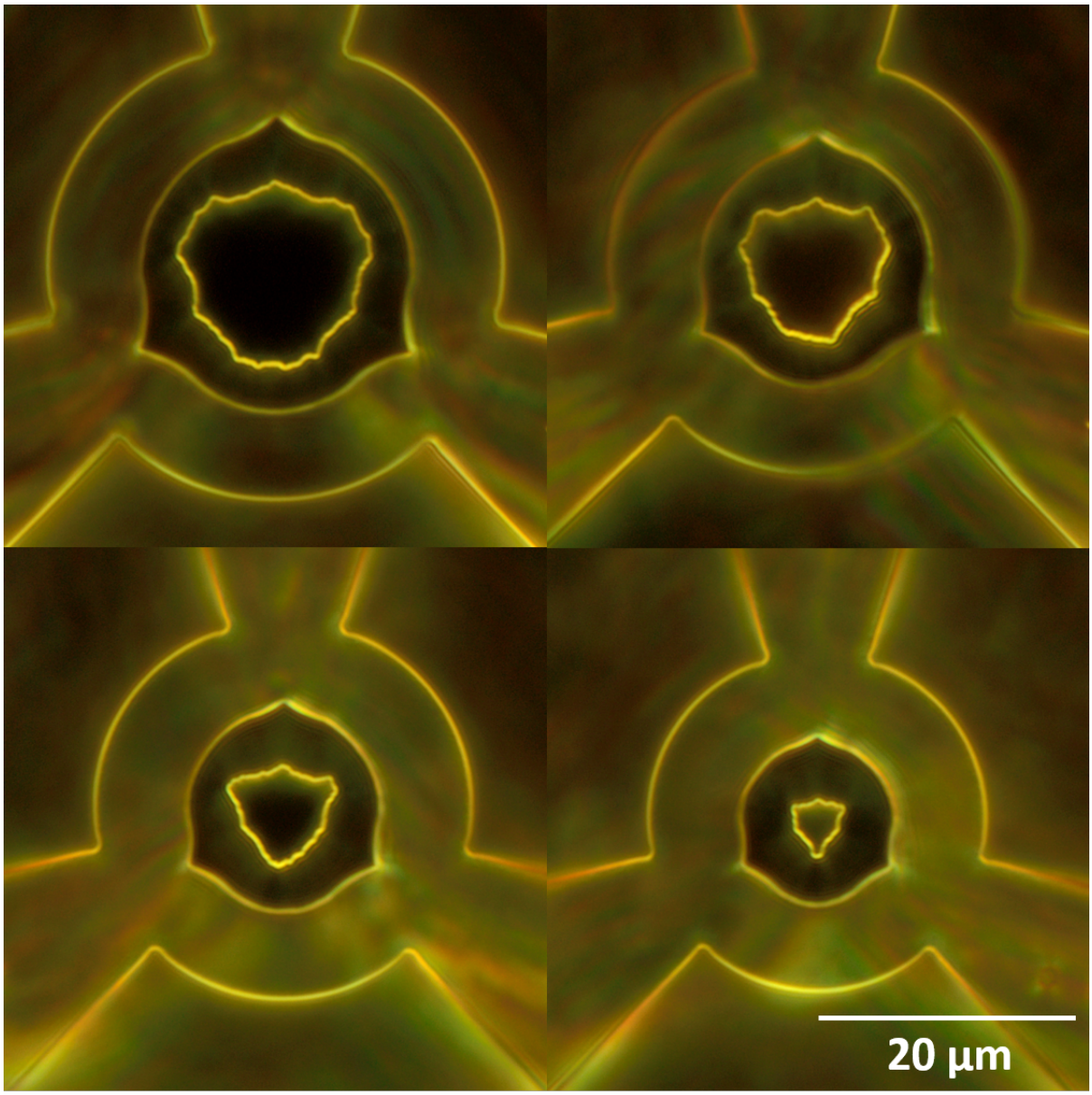

Figure 5.2: Triangle formed from oxide diffusion in a radiation sign mesa. The size of the initial mesa pattern is varied, from the biggest mesa in the top left, to the smallest in the bottom right. Triangular mesas are formed from diffusion through the arms. The devices shown are designed with no ellipticity.

polarization splitting [119]. A continuous, fine tuning method, though still needs to be developed for reliable fabrication of polarization degenerate cavities. The ellipticity can be used as a coarse control, compensating for crystalline effects. Here, fine tuning is realized with an additional electrical control. Complete restoration of polarization degeneracy of the fundamental mode is demonstrated. Electrical control of the embedded quantum dot wavelength is retained while the cavity polarization splitting is tuned.

The device presented, shown in Figure 5.3, has three contacts. The quantum dots are embedded in a p-i-n diode, which are buried in the device surrounded by two DBRs. A transparent ITO Schottky contact is deposited on the top of the device. An SEM and bright-field microscope image of a cavity with ITO is shown in Figure 5.4. Applying an electric field over the top mirror tunes the cavity polarization splitting through the Pockels effect. The electric field in the active region can be set independently to tune the quantum dot into resonance with the cavity mode. Such a device has similarly been used to control the output polarization state of a vertical-cavity surface-emitting laser through modification of the optical gain of the polarized modes [120]. Other methods of fine tuning may involve strain, which has also been utilized to fine tune the fine structure splitting of the dots. [121].

5.2.1 Tuning Theory

The single linear electro-optic coefficient, r_{41}, is taken to be a completely real value [105]. The dc electric field, E_{dc}, applied to the device is along the growth direction, which is the [001] direction. From Equation 4.4, the induced birefringence along the major [110] and minor [1$\bar{1}$0] axes is given by

$$\frac{1}{n_{\pm}^2} - \frac{1}{n_0^2} = \pm r_{41} E_{dc}, \tag{5.1}$$

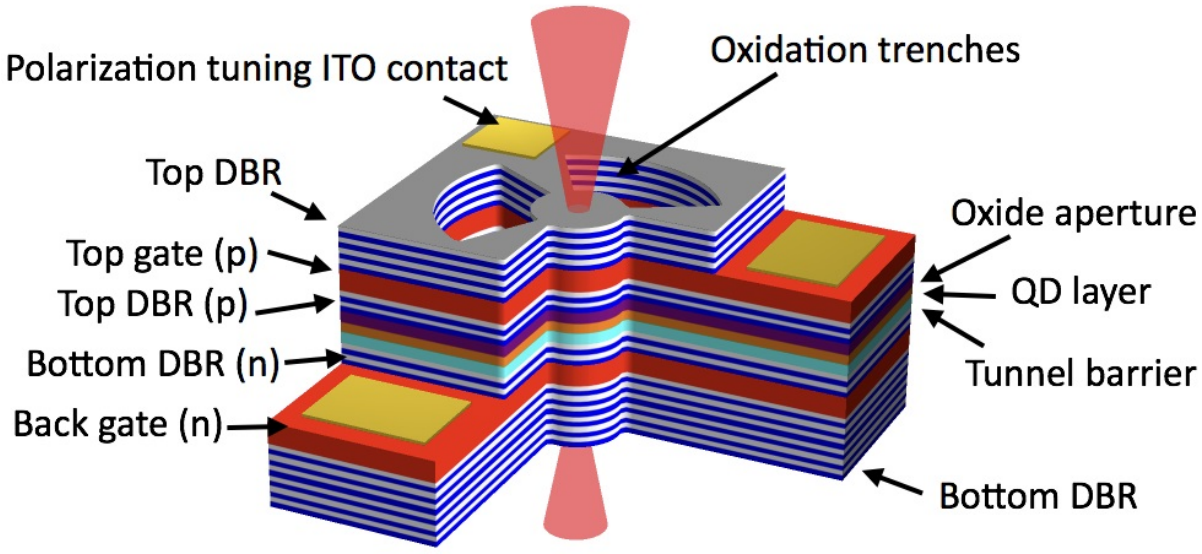

Figure 5.3: Representation of the microcavity. A p-i-n doped active region around the quantum dots controls their emission wavelength, and an ITO top contact can be biased with respect to the p layer to separately apply a voltage to the top mirror. This figure is published in Reference [122].

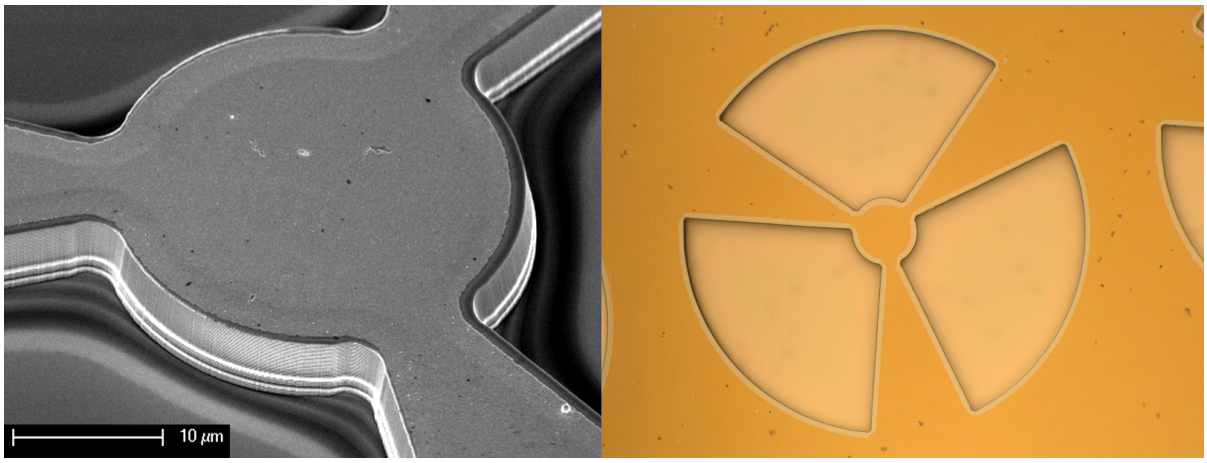

Figure 5.4: SEM and microscope images of a fabricated radiation sign device. The ITO layer is deposited on top of the device.

where n_0 is the real index without a field and $n_\pm$ refers to the real index of the $[110]\,(+)$ and $[1\bar{1}0]\,(-)$ axes, respectively.

As seen in Chapter 4, DBR mirrors exhibit a large penetration depth, and necessarily demand a finite phase dispersion. The reflection phase shift is zero, and reflectivity a maximum, when the wavelength satisfies the Bragg condition. The standard configuration to fabricate high quality factor cavities is precisely that the resonance wavelength matches the Bragg wavelength for both mirrors. In this configuration, there are field anti-nodes at the ends of the spacer, and the cavity resonance matches the expected value from the spacer alone. As the resonance is moved away from the Bragg condition, the standing wave pattern is disturbed, and the determination of the new resonance must take into account the non-zero phase shifts upon reflection of the mirrors.

The phase shift behavior of the DBR mirrors is studied with an effective mirror model [96]. The birefringence can be tuned in the spacer region, but the control across the spacer is reserved for tuning the quantum dot into resonance with the cavity. The large penetration depth, however, allows the cavity resonance to be tuned by applying an electric field only over a single mirror. It was shown that to first order, the time delay from a mirror is determined by the linear phase slope $\frac{d\phi}{d\omega}\Big|_{\omega=\omega_0}$. The time delay is replaced with an effective *hard* mirror. The effective penetration depth, L_{eff}, of the mirror is given by

$$L_{eff} = -\frac{c}{2n_1}\frac{d\phi}{d\omega}\bigg|_{\omega=\omega_0}. \tag{5.2}$$

Equation 5.2 is evaluated at the Bragg condition, denoted $\omega = \omega_0$. L_{eff} is used to model a dispersive mirror with a fictitious, *fixed phase*, mirror placed some distance from the actual mirror interface. In general, it is irrelevant what material is chosen to replace the resulting empty space, so long as the optical length is kept the same. For calculations involving cavities, it is most convenient to choose the material in front of

the mirror to be the same material composing the spacer region of the cavity, denoted by n_1. Analytical solutions for the penetration depth exist in the case of a single DBR mirror [123, 95, 96, 124].

The optical path length of the layers in a DBR are altered by the Pockels effect when a field is present; the Bragg frequency shifts as a result of an applied voltage. The shift is equivalent to moving the mirror some distance, ΔL_{eff},

$$\Delta L_{eff} = \frac{2n_1}{\omega_0 n_{1,gr}} L_{eff} \Delta\omega_{Bragg}. \tag{5.3}$$

$\Delta\omega_{Bragg}$ is the frequency shift of the Bragg condition and $n_{1,gr}$ is the group index of the spacer material. Considering a Fabry-Perot cavity formed from two identical DBR mirrors, with penetration depths given by Equation 5.2 and a spacer layer of length, L_{spacer}, the cavity resonance shift can be calculated. The frequency shift of the cavity, $\Delta\omega$, is given by

$$\Delta\omega = \frac{n_1}{n_{1,gr}} \frac{2L_{eff}}{L_{spacer} + 2L_{eff}} \Delta\omega_{Bragg}. \tag{5.4}$$

Equation 5.4 would be the complete solution if the back mirror exhibits no phase dispersion. However, a change in the resonance frequency of the cavity is equivalent to applying a second phase shift on the back mirror. For two DBR mirrors, the cavity shift from the change in penetration depth of one mirror is accompanied by a change in penetration depth of the second. The coupling of both mirrors with a shift in cavity frequency must be taken into account. The parameter $k = \frac{n_1}{n_{1,gr}} \frac{2L_{eff}}{L_{spacer}+2L_{eff}}$ is introduced for simplicity, which is a dimensionless parameter related to the effect of moving a single mirror. Equation 5.4 can then be written as $\Delta\omega = k\Delta\omega_{Bragg}$. A steady state equilibrium solution for the total change in the resonance frequency can be written as

$$\Delta\omega = -k\Delta\omega + k\left(\Delta\omega_{Bragg} - \Delta\omega\right). \tag{5.5}$$

The first term on the right hand side of Equation 5.5 is the phase change of the back mirror. The deviation from the Bragg condition is precisely the total resonance shift. The second term is the phase shift of the second mirror, which is determined from the difference in the Bragg shift of the mirror and the total resonance shift. The total change in cavity resonance is determined from Equation 5.5

$$\Delta\omega = \frac{k}{1+2k}\Delta\omega_{Bragg}. \tag{5.6}$$

$\Delta\omega_{Bragg}$ is found from computing the new optical path length of a single period in the DBR with an applied field. The cavity polarization splitting is denoted $\Delta\omega'$. For small changes in the index of refraction of both materials composing the DBR cavity, n_1 and n_2, the polarization splitting can be expressed as

$$\Delta\omega' = \frac{k}{1+2k}\frac{\omega_0}{2}\left(\frac{\Delta n_1}{n_1} + \frac{\Delta n_2}{n_2}\right). \tag{5.7}$$

The values Δn_1 and Δn_2 are the changes in refractive index for materials 1 and 2, which compose the mirror.

It turns out that the coupling of the mirrors is such that, in the language of effective mirrors, pulling one mirror also pulls the other with it in the same direction. The standing wave, thus, translates in one direction. The pulling effect diminishes the available tuning range, as the frequency shows a preference to remain the same. The results of the model suggest looking for a way to develop an alternate mode of tuning, where the mirrors shift in the opposite direction. The standing wave would be pulled apart. However, it is discussed later, that this mode of tuning exhibits significant tradeoffs.

The features of the effective mirror model in the system are demonstrated in TMM simulations. A simplified structure, one compatible with the model, is shown in Figure

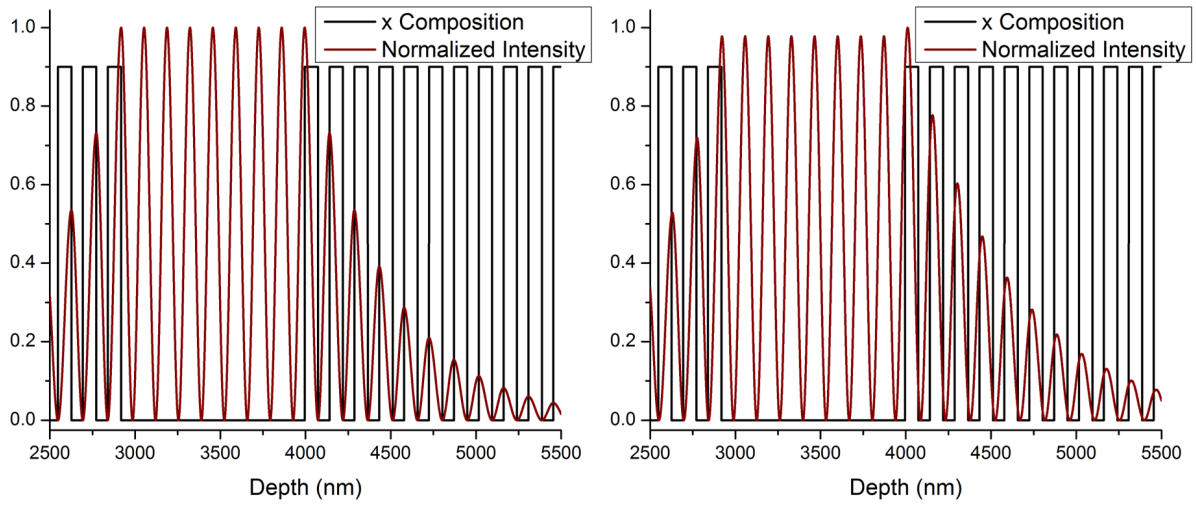

Figure 5.5: Exagerated TMM simulation of the electro-optic tuning effect. (Left) the normal case without electro-optic tuning. (Right) after applying the electro-optic tuning to the top mirror. The penetration depth after tuning increases, a direct consequence of the induced phase shift of the mirror.

5.5. The parameters used in the simulation are greatly exaggerated, and only used to point out the features of tuning. For the right plot, a bias on the top mirror is added. The penetration depth is altered, thereby giving rise to a new resonance frequency. The same simulation is shown in Figure 5.6 where the ends of the spacer are analyzed in greater depth. The frequency pulling predicted by the model agrees with the simulation.

5.2.2 Experimental Results

Equation 5.7 assumes two identical mirrors with a cavity resonance matching exactly the Bragg condition. Our devices have more complex designs than this simplified model. Nevertheless, the model can give a rough estimate of the expected tuning range with an applied voltage over a single mirror, and yield insight into the effects of various parameters that may be exploited to increase the tuning range. Parameters derived from the device design yield a penetration depth, $L_{eff} = 382$ nm, and the spacer layer thickness is, $L_{spacer} = 536$ nm. Values for the linear electro-optic coefficient are taken to be

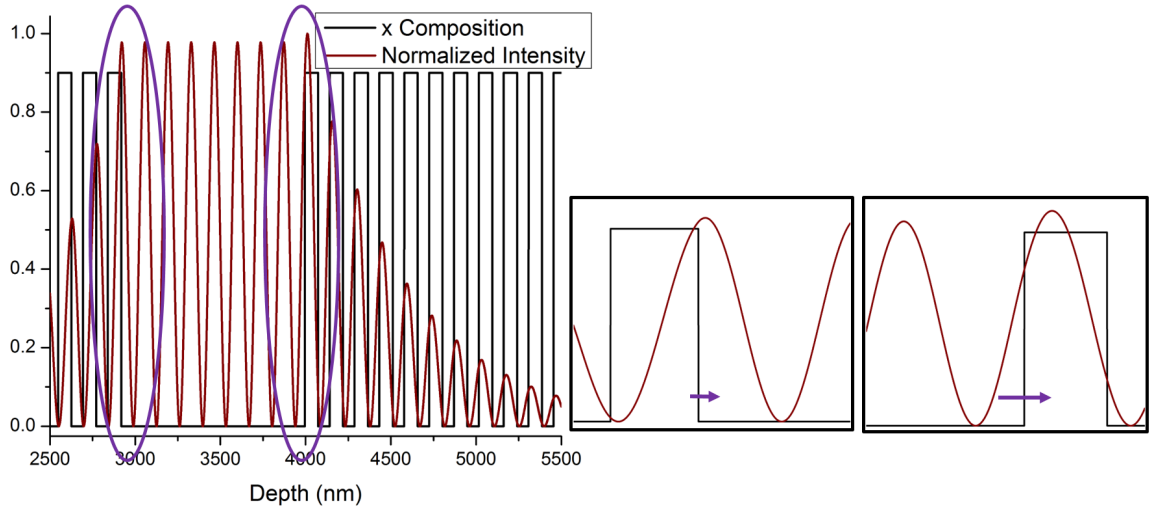

Figure 5.6: TMM simulation demonstrating the frequency pulling of the mirrors from tuning the DBR out of resonance.

$r_{41} = 1.72 \times 10^{-10} \mathrm{cmV}^{-1}$ and $r_{41} = 1.00 \times 10^{-10} \mathrm{cmV}^{-1}$ for GaAs and AlGaAs respectively [125]. An estimate of the tuning range using Equation 5.7 then yields $\Delta\omega' = 2.2$ GHz. The theoretical model is verified with TMM calculations. TMM on a symmetric cavity, which is consistent with the assumptions of the model, yields a tuning range of 2.2 GHz as well.

The samples are etched in a radiation pattern. The mesa is elongated along the major axis to account for the initial built-in birefringence. The ellipticity is used as a coarse tuning, whereby the electro-optic tuning method can be used as a fine control. With polarization resolved reflection spectroscopy, the electro-optic tuning method is studied on the scale of GHz. Complete restoration of the cavity polarization splitting is achieved.

Reflection spectroscopy on the lowest order HE_{11} Gaussian modes of the cavity, centered at 930 nm with quality factor Q $\sim$ 35,000, reveal in detail the behavior of the modes with electro-optic tuning. Figure 5.7 (a) shows the typical tuning behavior when the top mirror voltage is tuned and the p-i-n voltage is fixed. H and V are the cavity modes, and H corresponds to the major axis, [110]. H and V cross around -5 V for this cavity.

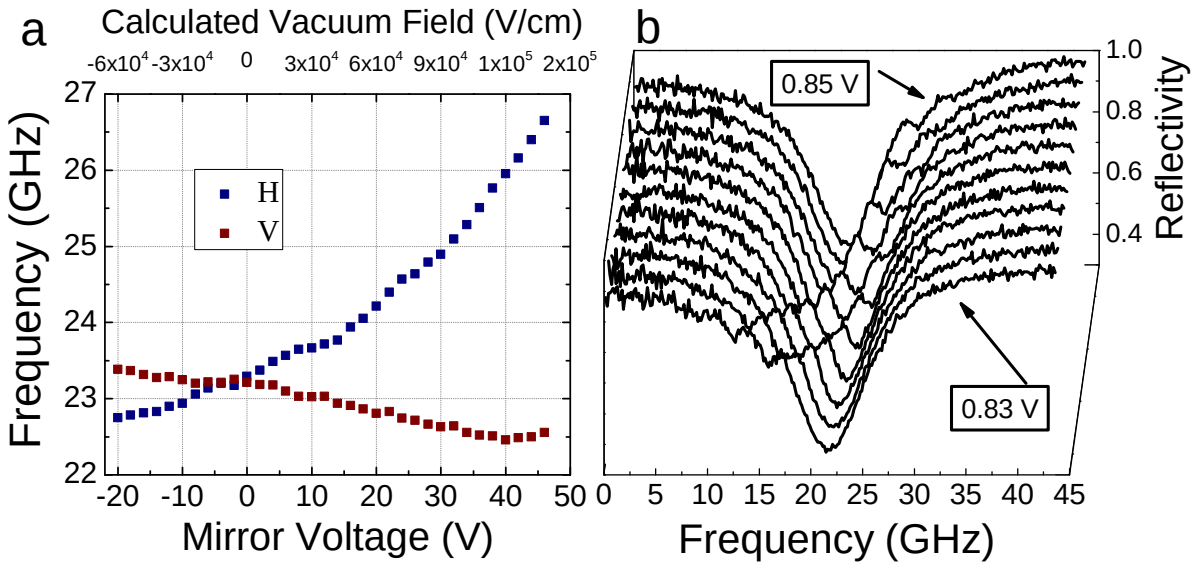

Figure 5.7: Typical behavior of the system tuning the top mirror voltage (a), and the p-i-n voltage (b). The cavity modes cross around -5 V when tuning the top mirror voltage. The quantum dot energy is tuned by tuning the p-i-n voltage. The top x-axis in (a) is the calculated field in vacuum units. This figure is published in Reference [122].

There is an absolute shift of the cavity resonance, which can be explained by quadratic electro-optic effects that do not exhibit birefringence: Kerr effect, etc. Figure 5.7 (b) shows the tuning of a quantum dot through the cavity as the p-i-n voltage is tuned, and the top mirror voltage is fixed.

The tuning range observed experimentally is approximately 4.5 GHz, and is completely reversible. The experimental tuning range observed agrees within an order of magnitude with the analytic model outlined above. As stated, the actual device does not completely satisfy the assumptions of this model. TMM calculations are also performed on the full device design, which yield a modest tuning range of 0.73 GHz, about 5 times less than observed in the experiment.

Several effects could explain the deviation of the observed shift from theory. In addition to the deviation from theory we observe a $\sim 10\,\%$ increase in the width of the H mode at high fields but not for the V mode. The device layout has contacts oriented

along the major axis and small transverse currents could introduce free carrier losses for only the H mode. Although mirror absorption can alter the phase dispersion, the observed increase in width does not correspond to values of absorption that are expected to result in measurable shifts of the cavity resonance. For transverse fields applied to the device, quadratic electro-optic effects can induce birefringence. Typical values of the quadratic electro-optic coefficient for GaAs are small, but very dispersive around the band gap [125]. Large quadratic effects have additionally been observed in complicated waveguide heterostructures [126, 127].

5.2.3 Demonstration of Optimal Quantum Dot Coupling

The quantum dot-microcavity system must be excited in the cavity polarization basis when the polarization degeneracy is large. An example of this, albeit with small polarization splitting, is shown in Figure 5.8. In the reflection spectrum of the cavity, the quantum dot appears as a peak in the cavity mode, which is due to the excitation of an electron-hole pair of a neutral quantum dot. Fits to a semi-classical model yield a quantum dot-cavity coupling of $g \sim 1.5$ GHz, and quantum dot decoherence of $\gamma \sim 1$ GHz. The fine structure splitting of the quantum dot is clearly visible as two peaks. The inset shows the same measurement for the case of imperfect polarization degeneracy. The p-i-n voltage is adjusted slightly as the mirror voltage is tuned due to a dependence of the quantum dot energy on the mirror voltage. This dependence does not prevent the ability to tune the quantum dot energy and cavity polarization splitting independently, but the two control voltages must be adjusted together to keep the quantum dot on resonance with the cavity.

Self-assembled InGaAs quantum dots, grown on [001] substrates, are typically not oriented along either the major or minor crystal axis [65]. The resulting cavity-quantum

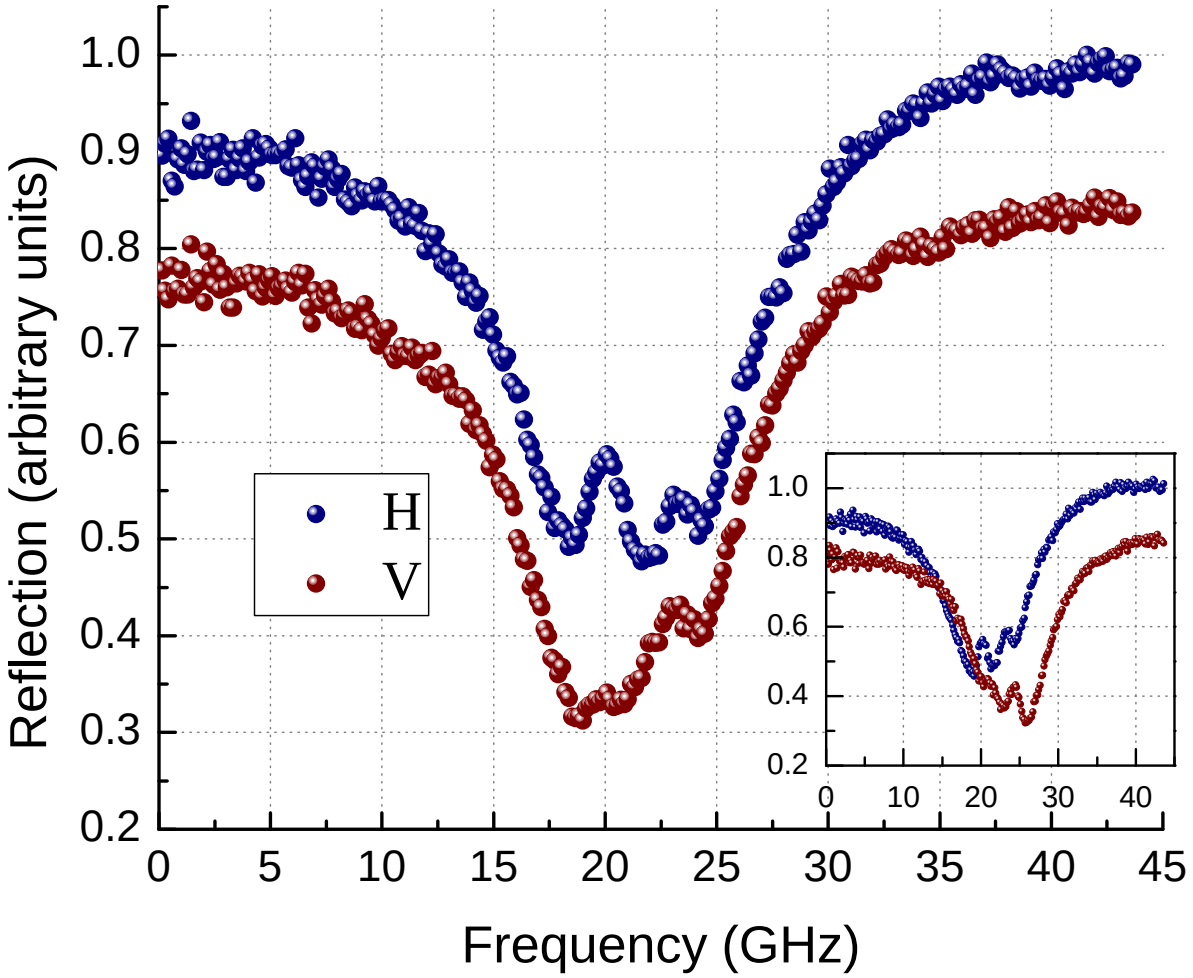

Figure 5.8: Polarization resolved reflection spectra for a polarization degenerate cavity. The incident laser polarization is aligned along the cavity axis. The cavity is tuned away from degeneracy in the inset. H and V are offset for clarity. This figure is published in Reference [122].

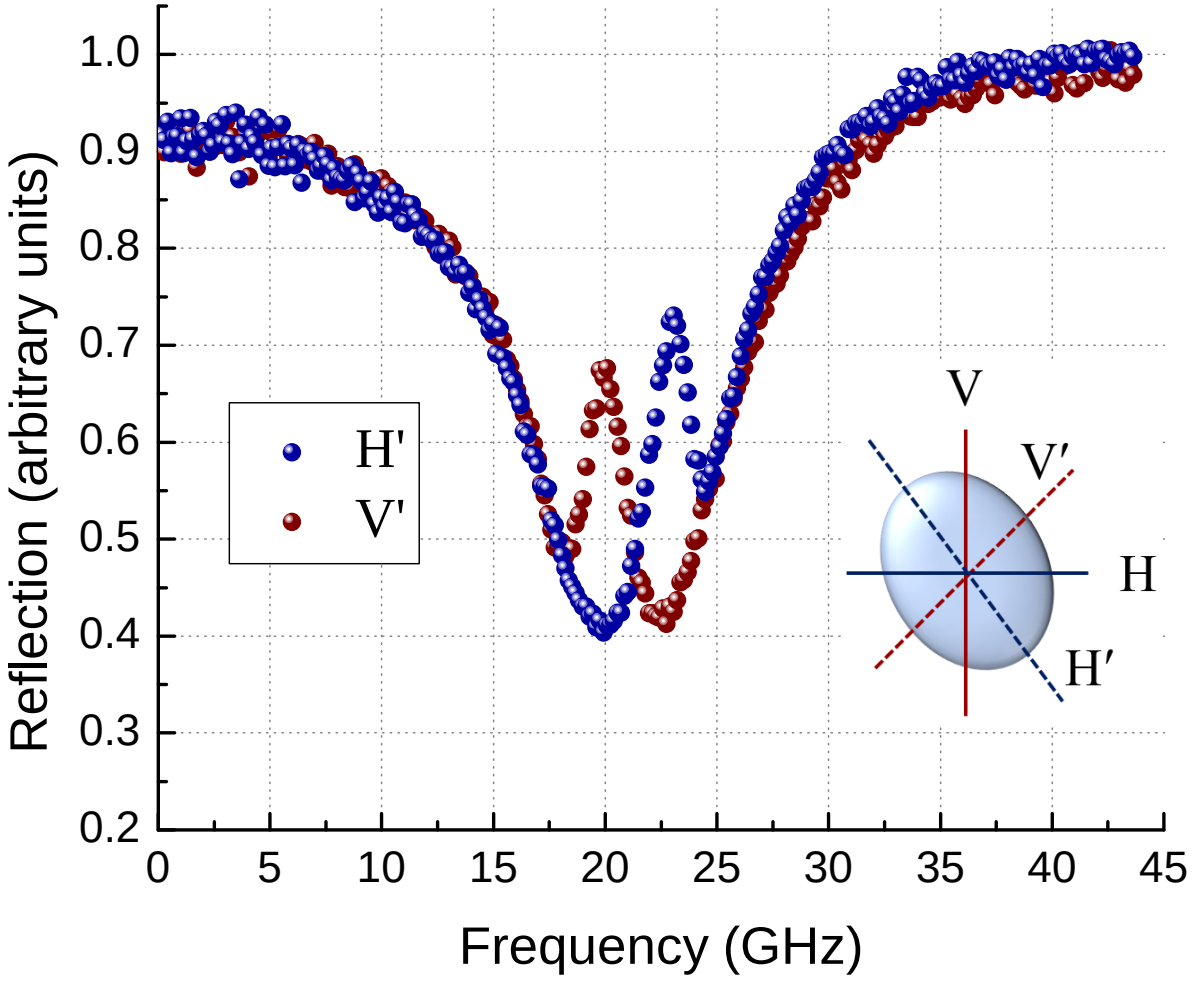

Figure 5.9: Reflection spectra of a polarization degenerate cavity in the basis of the neutral exciton transitions. Maximum quantum dot coupling is achieved without cavity birefringence. This figure is published in Reference [122].

dot system, therefore, has a cavity polarization basis and quantum dot polarization basis. Maximum coupling of photons to exciton transitions can be accomplished in the case of identical cavity and quantum dot basis, or when the cavity is polarization degenerate. The latter is shown in Figure 5.9, which shows the reflection spectrum in the quantum dot basis, denoted as H′ and V′. The quantum dot is oriented approximately 45° from the cavity basis. For either exciton transition, the coupling to the cavity mode is stronger than in the cavity basis, evident by the higher peaks in reflectivity.

5.3 Discussion

The three contact design has proven to be successful for fine tuning the cavity polarization into degeneracy. With a radiation pattern, the oxidation produces a triangle, which allows polarization coupling to be avoided. The fabrication process is compatible with deterministic methods of identifying particular quantum dots prior to fabrication We study a neutral quantum dot here, but the polarization degeneracy is also important for spin based applications.

To conclude this chapter, the challenges in improving the tuning range are discussed, with possible avenues of engineering devices for improved tunability. The electro-optic tuning method battles a small linear electro-optic coefficient. Despite this, it is experimentally verified that tuning is possible within a reasonable fine tuning range relevant for microcavities. There exists another drawback, which is the frequency pulling effect from the second mirror. Within the effective mirror framework developed, the frequency pulling is described by two coupled mirrors. As one mirror is pulled away from the cavity, the second mirror follows, resulting in translational motion of the standing wave.

As noted in Section 4.1, the slope of the phase response is rooted in causality. A drastically wider tuning range is found if the two mirrors push themselves apart. On

the surface, the alternate tuning mode is achieved if the back mirror has the opposite slope, however this is equivalent to there being a negative time delay, which cannot be achieved with a standard quarter wave mirror. The phase direction can be flipped, however, around a cavity resonance, which comes at an expense of a reduced reflectivity. By deviating from the standard quarter wave design, the phase and reflectivity can be modulated across the spectrum. An example of such a modification is lasers with sampled grating mirrors [128]. Engineering mirrors with oscillations in the phase response could prove to be a route towards increasing tunability, but it necessarily makes the mirrors less reflective, as the phase and reflectivity are not inseparable.

From the above discussion, it is likely that in attempting to improve tunability, there will exists tradeoffs between the reflectivity of the mirror, and its tunability. Unfortunately, applications involving cavity quantum electrodynamics with quantum dots demand that the mirrors be as highly reflecting as possible, leaving little room for additional engineering of the phase response. More direct improvements may be obtained by decreasing the length of the spacer region, which from Equation 5.4, can increase the phase shift. In this case the cavity resonance is not distributed over multiple nodes. It is also clear that the linear electro-optic effect has a more drastic effect when directly applied over the cavity region, therefore, wider tunability can be obtained if the p contact is placed within the cavity layer itself, tuning the cavity resonance directly. Care must be taken to avoid affecting the dots. For the later strategy, a longer cavity spacer may be beneficial, but the mode volume would necessarily increase.

5.4 Conclusion

With the addition of an electrical control, applying an electric field over one of the mirrors of the device, residual polarization splitting can be eliminated. The triangular

oxide aperture is expected to align the photo-elastic and form birefringence with the major and minor axes. Therefore, polarization mode coupling can be eliminated. With three contacts, two control fields can be utilized to tune the quantum dot resonance and the cavity polarization splitting. The form birefringence is utilized as a coarse control. With the electro-optic tuning method, it is proposed that single photon sources can be fabricated, exciting the quantum dot at arbitrary angles. This freedom could allow for optimization of the brightness of single photon sources with resonant pulsed excitation.

Chapter 6

Polarization Enabled Interactions

This chapter presents *polarization enabled interactions*. The work has been possible due to the fabrication of polarization degenerate, or close to degenerate, microcavities. When the cavity is polarization degenerate, the quantum dot can couple to both cavity polarizations. As discussed in previous chapters, this feature allows resonant excitation, with cross polarization filtering, of quantum dots. Interesting phenomena arise in the quantum theory of polarized cavity-quantum dot interactions. Two main results are presented here: Unconventional Photon Blockade (UPB), and strongly correlated photons. The experiments presented in this chapter are the result of a collaboration with the quantum optics group at Leiden University. More details can be found in the original manuscripts [129, 130]. UPB was additionally observed subsequently by another group of researchers working in the microwave regime [131].

6.1 Unconventional Photon Blockade

Resonant generation of single photons in the strong coupling regime can be achieved by means of photon blockade [32]. The non-linear Jaynes-Cummings ladder, in this

scheme, allows resonant excitation to only one dressed state. Transitions to the higher number rungs of the ladder are non-resonant. Photon blockade requires, strictly, the strong coupling condition, which is difficult to achieve with microcavities.

The mechanism of UPB considers the coupling of two cavity modes by means of a single emitter. The effect was originally proposed by Liew and Savona [132]. In particular, the work demonstrated that strong antibunching could be observed at the output of the system, even for relatively small Kerr nonlinearities. The method greatly relaxes the constraint of having low cavity loss. It turns out, cavity loss is a necessary mechanism for the observation of the effect [133].

The original work described the antibunching numerically. Bamba et. al showed that UPB could be explained by destructive quantum interference between different excitation pathways [134]. The theoretical framework has been further developed for multiple interactions. Input output theory has been developed [135], as well as the theory for Gaussian squeezed states [136]. Gerace and Savona [137] showed the effect could be observed from two cavities with a bulk material possessing a finite second-order susceptibility. A review of UPB is given by Flayac and Savona [138].

Figure 6.1 shows the basic pathways available in a cavity with a single quantum dot transition. Only the lowest photon number states, from zero to two, are considered here. The conventional photon blockade effect is demonstrated in Figure 6.1 (a). Strong coupling results in a non-linear Jaynes Cummings ladder of polariton states. A resonant transition to the first state is non-resonant with the higher number states. Figure 6.1 (b) demonstrates UPB. From the ground state, a photon can be excited, either in the $|10\rangle$ or $|01\rangle$ states. In the weak coupling regime, these states can be sufficiently described by the bare states of the cavity. The cavity, further, is considered to be polarization degenerate. From the one photon states, the two photon states can be excited. The two photon states can either exist in the configuration that two photons are in one polarization, or that one

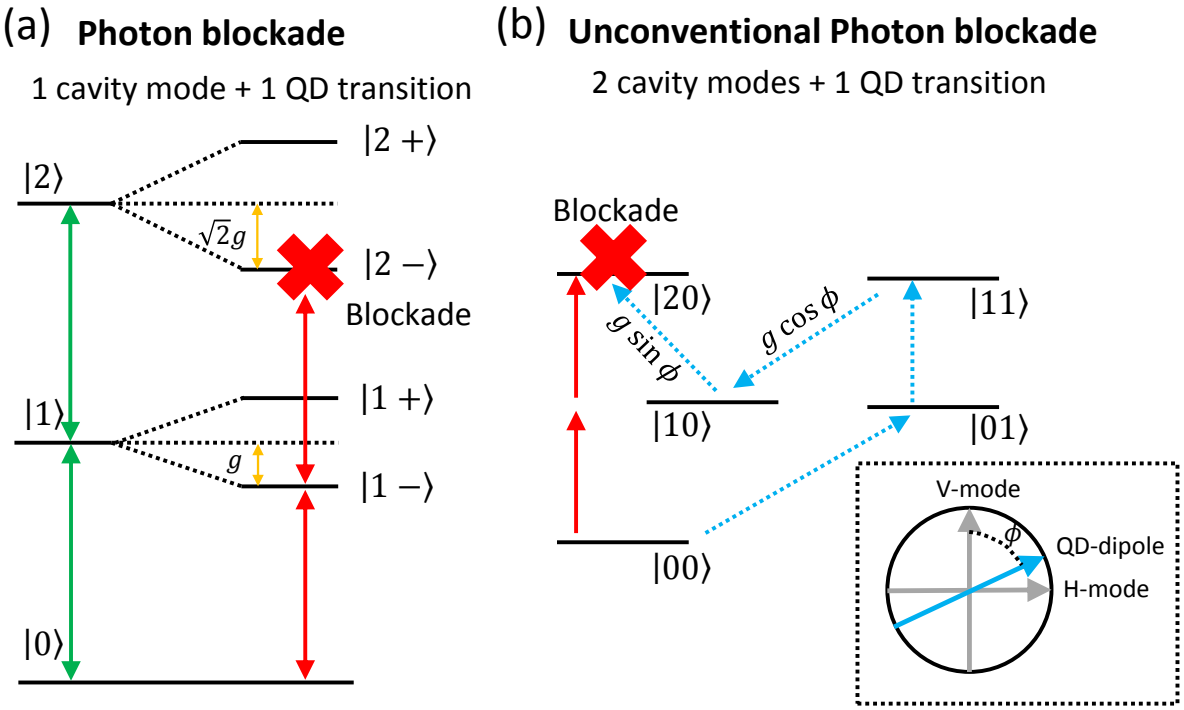

Figure 6.1: Level diagram indicating the processes of photon blockade (a) and unconventional photon blockade (b). The dressed states can be individually dressed in the case of photon blockade, and transitions to higher rungs on the Jaynes-Cummings ladder are non-resonant from the anharmiticity of the ladder. Unconventional photon blockade relies on interference between the two paths provided by the polarization degenerate cavity. This diagram is published in Reference [129].

photon is in each polarization.

From the two photon states, the system can decay back to the one photon states. The particular pathways of interest are the two pathways to the $|20\rangle$ state. Post-selection with a polarizer can select for photons emitted in this state. The presence of a strong nonlinearity, which couples both modes of the cavity, results in a relative phase shift between the two pathways. The two pathways destructively interfere to block transitions to the $|20\rangle$ state.

To study the results, the Hamiltonian from Equation 2.41 is modified to include both

cavity polarizations and drive polarizations

$$\frac{\hat{H}}{\hbar} = (\omega_l - \omega_H)\,\hat{a}_H^\dagger \hat{a}_H + (\omega_l - \omega_V)\,\hat{a}_V^\dagger \hat{a}_V + \frac{1}{2}(\omega_l - \omega_0)\,\hat{\sigma}_+\hat{\sigma}_- + g\left(\hat{\sigma}_+\hat{b} + \hat{\sigma}_-\hat{b}^\dagger\right) + \eta_H\left(\hat{a}_H^\dagger - \hat{a}_H\right) + \eta_V\left(\hat{a}_V^\dagger - \hat{a}_V\right). \tag{6.1}$$

ω_H and ω_V are the resonance frequencies of the linearly polarized cavity modes, $\hat{a}_H^\dagger$ and $\hat{a}_V^\dagger$ are the photon creation operators for both polarizations. ω_{QD} is the quantum dot resonance frequency, and $\hat{\sigma}_+$ is the standard raising operator. The drive is further separated into two polarizations with the field strengths, η_H and η_V, for the two polarizations. The quantum dot couples to both cavity modes, depending on the angle the dot makes with the cavity. The interaction term includes the creation operator, $\hat{b} = \hat{a}_V \cos\phi + \hat{a}_H \sin\phi$, where ϕ is the relative angle between the cavity and the quantum dot.

UPB can be studied numerically using the quantum master equation in Lindblad form, Equation 2.42, with the above Hamiltonian. The calculation of the $g^{(2)}(0)$ is shown in Figure 6.2. The cross polarization condition is evident from the blue area of the plot, which is characterized by $g^{(2)}(0)$ of zero. Outside of this condition, the $g^{(2)}(0) = 1$, as expected, due to the amount of coherent light leakage through the system. The calculation also demonstrates photon bunching behavior under polarization conditions given in the red regions.

H and V denote the cavity modes, although the cavity is polarization degenerate in the simulation. Antibunching is expected under cross polarization, which is the typical case for a single photon source. The origin of antibunching, classically, comes from the fact that the photons are rotated by the quantum dot. Only photons, which undergo a polarization rotation, are allowed through the second polarizer. Simulations in Figure 6.2 fail when the light excites one of the quantum dot axes. In this configuration there is no polarization rotation experienced, and single photon generation does not occur. In

UPB, antibunching occurs after post-selecting only one cavity mode, which is initially in the vacuum state. If post-selection is not anti-aligned with the incoming light, the output state is a mixture of light in two modes. It is possible to interpret the bunching as a quantum interference effect, where photon pathways constructively interfere. In this instance, one photon states are blocked, while higher number states are allowed through. The transition of antibunched light to bunched light is a critical feature of UPB [138].

The UPB region, shown in the simulation by B, is explored experimentally. Results are presented in Figure 6.3 for varied outgoing half wave plate and quarter wave plate angles. The sample studied contains a residual polarization splitting of 1.6 GHz, which is added to the theory. In Figures 6.3 (a) and (b), the mean photon number is plotted, where the experiment and theory agree very well. The average photon number input is 0.06. More photons are allowed through the polarizer as the output waveplates are adjusted. In Figures 6.3 (c) and (d), $g^{(2)}(0)$ is plotted, again for experiment and theory, with a close match between the two. In Figures 6.3 (e) and (f), $g^{(2)}(\tau)$ is plotted for the points marked by arrows C and D, to more clearly demonstrate the transition. Taking into account the detector jitter, $g^{(2)}(0) \sim 0.005$ is obtained.

The experiment is performed under continuous wave excitation, which allows the use of a better formulated theory and aids in eliminating spectrally dependent rotations from the birefringent cavity. As the UPB effect is observed away from the cavity axis, this is a necessary condition. A polarization degenerate cavity, such as the one presented in Chapter 5, is needed to perform pulsed UPB. In the continuous wave case, it can be shown that the cavity polarization splitting reduces the effectiveness of the method [129].

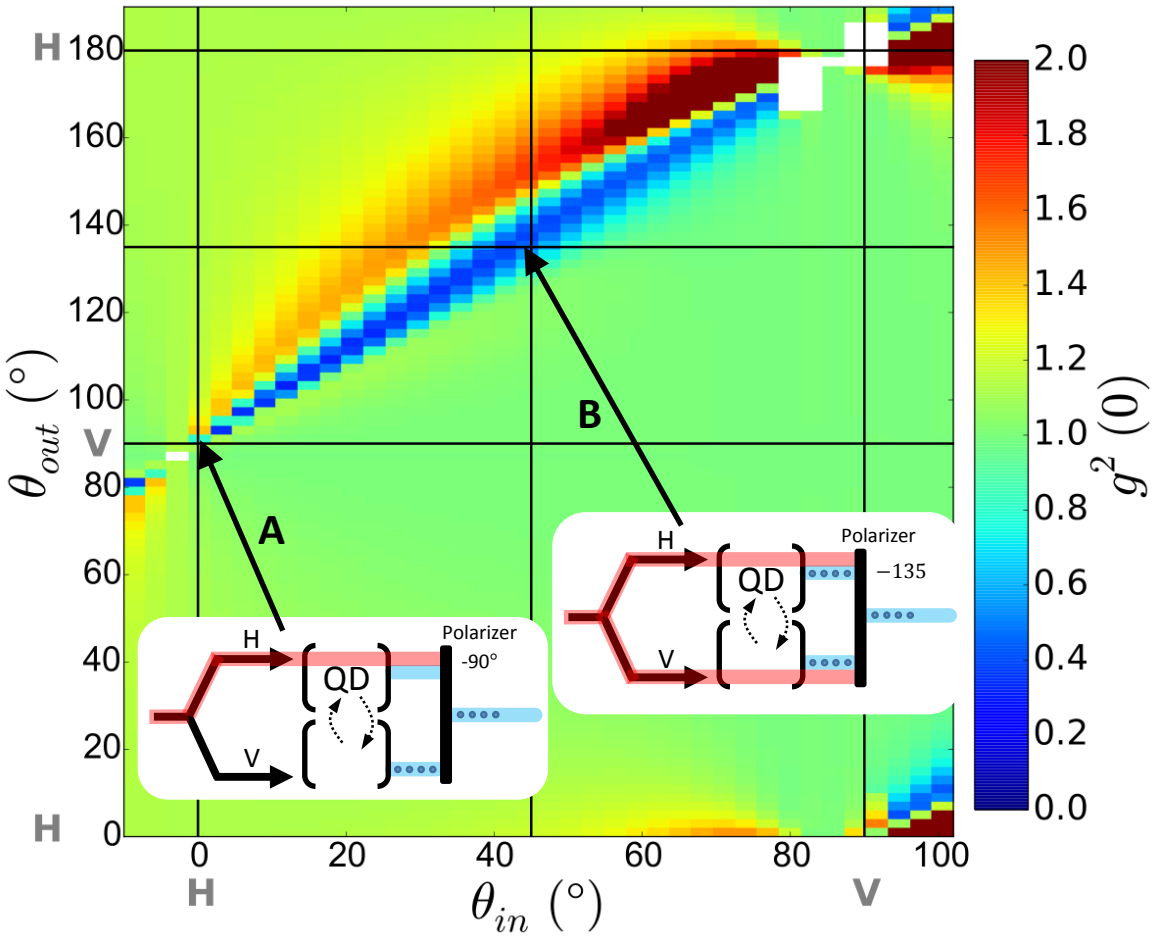

Figure 6.2: Simulation of $g^{(2)}(0)$ with various linear polarization, in and out, configurations. H and V denote the cavity polarizations. The standard single photon source is indicated by A, where one cavity mode is excited. Unconventional photon blockade is seen in the area pointed out by B. Both cavity modes are excited. This figure is published in Reference [129].

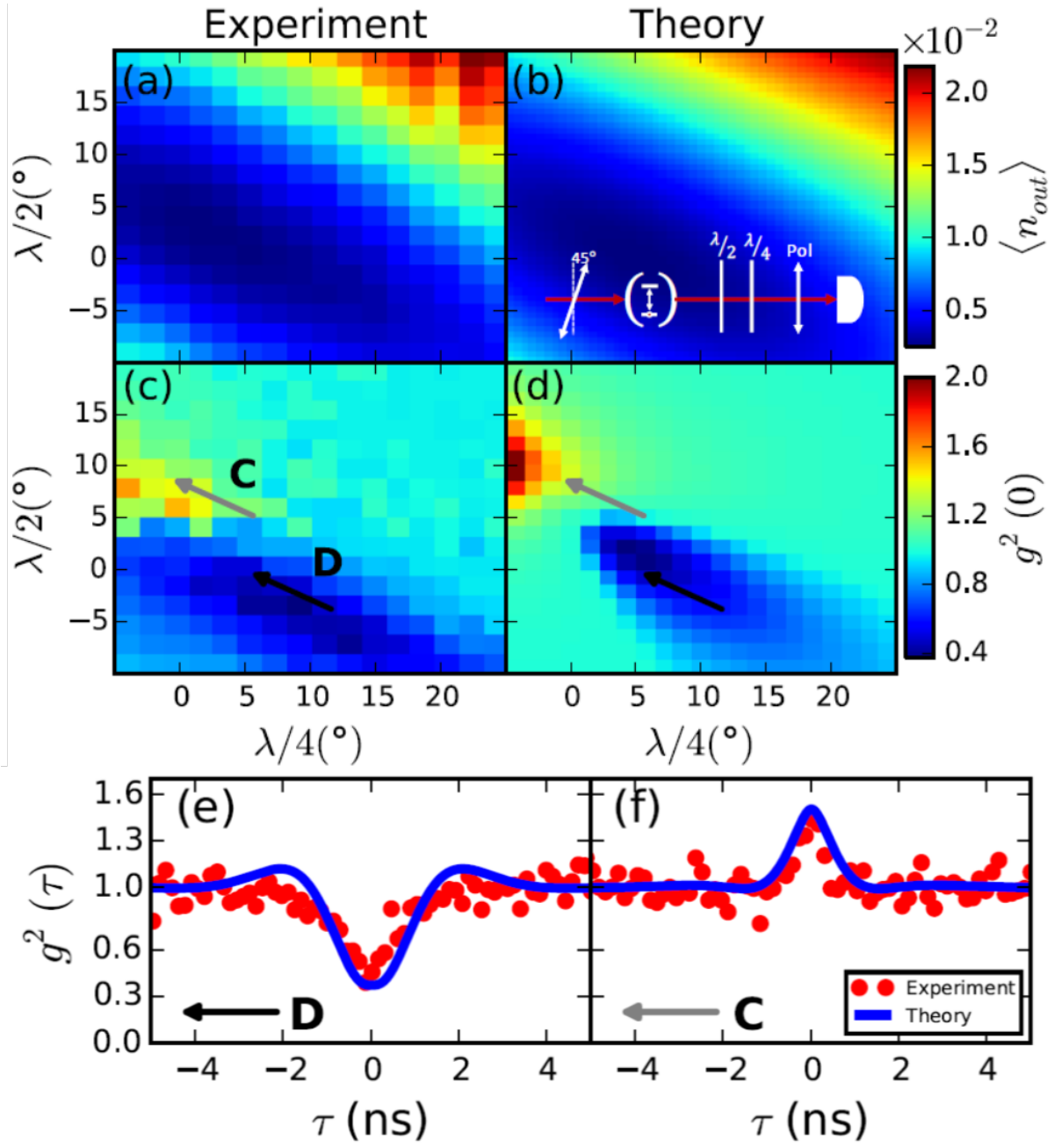

Figure 6.3: Experiment and theory of UPB in the region B, from Figure 6.2. (a) and (b) show the mean photon number for quarter and half waveplate outputs. (c) and (d) show $g^{(2)}(0)$ for the same configurations. The $g^{(2)}(\tau)$ function for points C and D are shown in (e) and (f). This figure is published in Reference [129].

6.2 Strongly Correlated Photons

In a classical description of polarization rotations, photon bunching and antibunching are not immediately evident. A classical description was presented in Section 2.6, and used to predict the performance of single photon sources in Section 4.3. Photon statistics necessarily disappear in a completely classical approach. Antibunching is inferred because the quantum dot is a single emitter, which can only emit one photon per emission lifetime. A low $g^{(2)}(0)$ is expected when the coherent input light is sufficiently depressed. Photon bunching well beyond classically expected values is demonstrated here. The work in this section is published in [130].

UPB was demonstrated as a way to produce single photons from quantum interference between cavity modes. It was demonstrated with UPB that both antibunching and bunching can be produced from a two level system. Although the quantum dot is a single emitter, the interaction of two cavity paths allows for a configuration for photons to constructively interfere. The observed $g^{(2)}(0)$, can be greater than that of thermal light sources. In the regime of very weak excitation, a very high second order correlation function can be measured. For certain polarization conditions, a $g^{(2)}(0) > 25$ is measured.

Figure 6.4 (a) presents the polarization orientations, which produce statistically different photon outputs. With co-polarized pre and post-selection, the expected coherent output is obtained. Under cross polarization, the output is strongly antibunched due to the interaction with a single embedded dot. Cross polarization is the typical orientation for building a single photon source. Figure 6.4 (b) shows the transmission around the cavity resonance, where the special polarization is shown to enhance the contrast of the quantum dot dip. Under a special polarization angle, a strongly correlated photon output is obtained. The value of $g^{(2)}(0)$ varies depending on the timing jitter of the detector. Figure 6.4 (c) shows the $g^{(2)}(0)$ obtained for detectors with 500 psec jitter, 50 psec jitter,

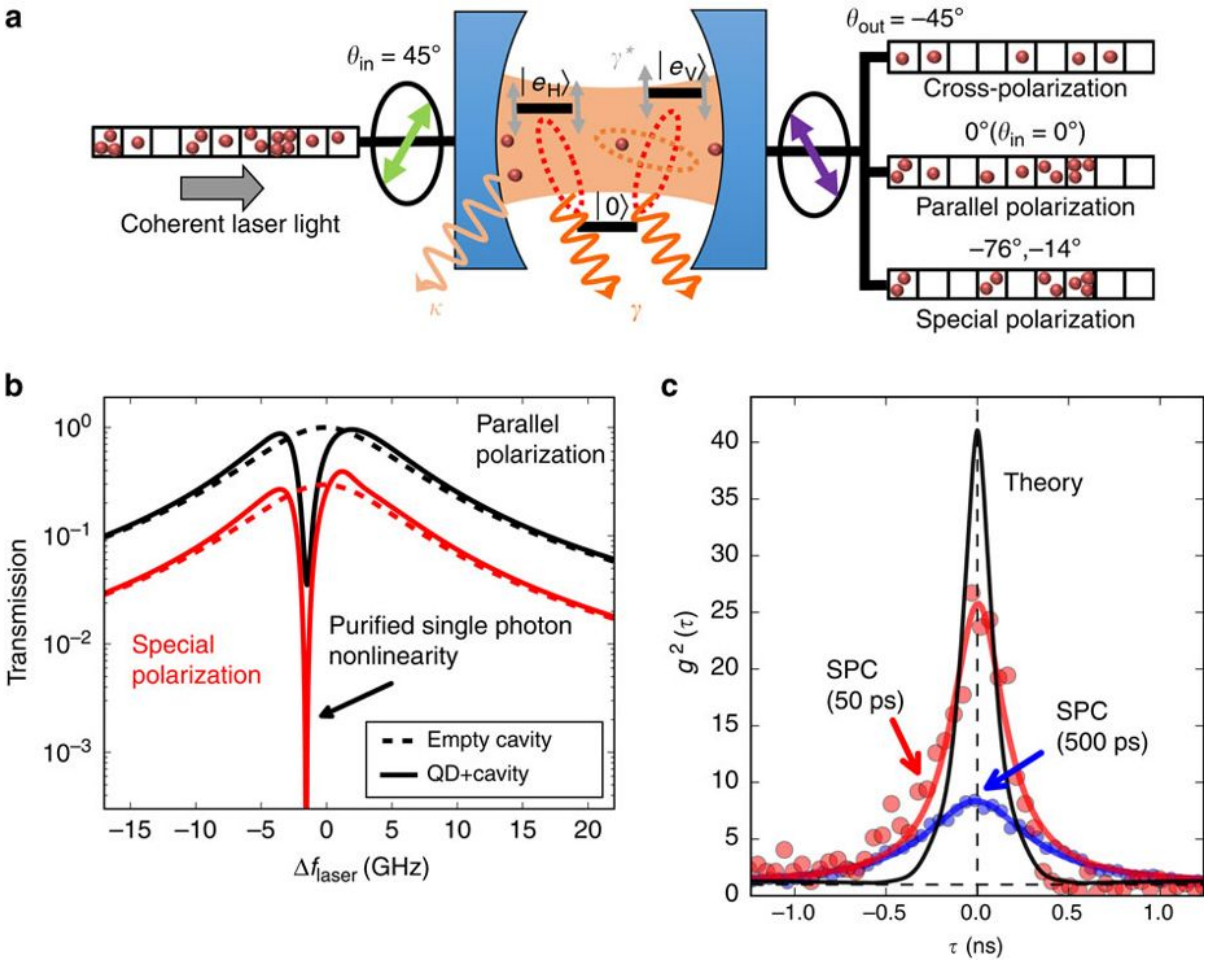

Figure 6.4: Strongly correlated photons as the incoming and outgoing polarization states are altered. (a) A diagram indicating the polarization orientations. The usual polarization orientations are represented by parallel and cross polarized output polarizers. With a special angle, bunching occurs. (b) The transmission around the cavity resonance with parallel polarization and special angle polarization. (c) The second order correlation function exhibiting enhanced bunching, measured with two sets of detectors. This figure is published in Reference [130].

and the theoretical solution. $g^{(2)}(0) = 25.7 \pm 0.9$ from experiment, and is expected to be greater than 40 without detector jitter.

To understand the strong photon correlations, much greater than the classical limit, consider that a coherent input is applied to the cavity. The standard configuration, then, allows for a single photon to be transmitted through a cavity with a different polarization state. If the single photon component is subtracted from the field, the result is an intensity dependent $g^{(2)}(0)$. The strong correlation is achieved in a regime of very weak excitation. In this limit, it can be assumed that three photon states and above can be neglected. A subtraction of the one photon state produces states, with the greatest probabilities to be in the vacuum state or the two photon state.

Both UPB, and the strongly correlated photon result, can also be discussed in terms of general quadrature squeezing. The fundamental difference between antibunching and sub-Poissanian light was pointed out in Chapter 2. Sub-Poissanian light can be referred to as amplitude squeezed. The system currently studied has not been able to produce amplitude squeezed light. However, it is discussed in detail how the system can produce more general quadrature squeezed states [82], which in principle can be measured by superimposing the squeezed light with the excitation laser. Use of squeezed states from quantum dots is limited at the moment. However, a prime example of the practical use of squeezed light comes from detecting gravitational waves [139].

6.3 Conclusion

Classically, single photon generation with resonant excitation is obtained by linear polarization rotations induced by a single quantum dot. The interaction of a quantum dot with a polarization degenerate cavity should, however, be most correctly described with quantum mechanics. The generation of single photons has most simply been explained

by quantum interference between two cavity modes. Unconventional photon blockade has been studied in detail, and verified in our experimental system. Interesting dynamics appear under arbitrary polarization orientations. In particular, both antibunched and bunched photon statistics can be found from the interaction of a two-level system in a polarization degenerate cavity. The amount of bunching can greatly exceed expected classical results. Further studies of this system in the quantum regime may yield insight for the design of single photon sources.

Chapter 7

Conclusion and Outlook

To conclude, interesting dynamics between quantum dots and multiple cavity modes are accessible with strong enough coupling of the quantum dot to both modes. Such interactions are studied here, where the cavity modes are the two-fold degenerate polarizations of a microcavity. The physical processes are diminished, however, as the cavity polarization splitting is larger than the cavity width. The optimal situation is exact polarization degeneracy. The experiments demonstrated in this thesis, which deviate from the case of exciting one polarization, are performed with weak narrow linewidth lasers to avoid masking the quantum dot interaction with coherent background light. With perfectly polarization degenerate cavities, this background can be reduced. On one hand, the performance of single photon sources can be improved because an arbitrary angle of excitation light with the quantum dot can be chosen. Experiments with higher power and pulsed excitation may provide insight into the quantum dynamics of the cavity-quantum dot interactions as well. Such insight may reveal avenues to improve single photon performance.

What is contained in this thesis, is a detailed account of birefringent phenomenon in semiconductor micropillar cavities. For cavities with a high quality factor, normally small

birefringent mechanisms must be considered. In particular, photo-elastic and electro-optic effects dictate a polarization splitting along the major and minor crystal axis. It is possible to reduce strain related birefringence with extremely careful fabrication practices. However, the linear electro-optic effect remains unavoidable because doping and electrical control of the quantum dot resonance is always required. A coarse compensation can be utilized with the form birefringence of an aperture, or mesa shape in an air guided pillar. Asymmetrical apertures may further be required to avoid polarization mode coupling.

At the end of the day, the polarization splitting needs to be controlled within ∼GHz. Such a tolerance cannot be obtained in fabricated devices without a method of fine tuning. At least one new method was developed for the work of this thesis. It was shown that complete polarization degeneracy can be achieved with an additional electrical contact placed on top of the device. The quantum dot resonance and polarization splitting are independently tuned. The electro-optic tuning method is simple. Only one additional contact is deposited, and the additional fabrication steps are non-invasive to the rest of the process. With the knowledge contained here, I remain hopeful that improvements can be made to the electro-optic tuning method. Additional methods of fine tuning the polarization splitting, such as the utilization of the photo-elastic behavior, may also be possible.

Appendix A

Process

A.1 Process Flow

In order to use the electro-optic polarization tuning method, an ITO top contact layer must be deposited on the top of the device. It is best to deposit the ITO layer first. It is possible to perform the liftoff recipe after the etch if desired. The recipe developed is for liftoff of ITO. A hot HCl etch wet etch, or dry methane etch, can be used otherwise to pattern the ITO. The rest of the process is standard for VCSEL fabrication. The N and P etches can be performed in either order, same for the N and P metallizations. The general order of the process, though, should be followed. The metal recipes are not compatible with oxidation in the furnace. It is best to have both contacts deposited before the last anneal.

- ITO Liftoff
- N and P etches
- Oxide Aperture
- N and P Metalizations

- Rapid Thermal Anneal

ITO liftoff

- Solvent clean: Acetone, Isopropanol, blow dry
- Bake at 115°C for 5 minutes
- Spin NR9-1000PY at 3000 rpm
- Softbake at 150 °C for 60 seconds
- Expose for 1 minute 30 seconds
- Post Exposure Bake at 100 °C for 60 seconds
- Develop for 10 seconds in AZ300 MIF
- DI rinse
- Deposit 40nm ITO. Start at 0.1Å/second. Ramp to 1Å/second
- Liftoff in NMP for 3 hours
- Solvent clean: Isopropanol, blow dry
- Gasonics recipe 3, 3 times 90 seconds
- Anneal in RTA, 1 hour at 200°C in N_2

N/P Etch

- Solvent clean: Acetone, Isopropanol, blow dry
- Bake at 115°C for 5 minutes
- Spin on AZ4330 at 3000 rpm

- Softbake at 95°C for 60 seconds
- Expose for 25 seconds
- Develop in AZ 400K 1:4, about 1 minute 30 seconds
- DI rinse
- Monitored NEtch/PEtch
- Immediate DI Rinse
- Liftoff in NMP for 3 hours
- Solvent clean: Isopropanol, blow dry
- Gasonics recipe 3, 3 times 90 seconds

Oxide

- NH_4OH clean 20 seconds, blow dry immediately before furnace
- Wet oxidation in Lindberg furnace, 420°C, 8 sccm, 80°C probe temperature
- Wet etch calibration dies in H_3PO_4:H_20_2:DI 1:1:10, typically 8 minutes

N/P/ITO Metal

- Solvent clean: Acetone, Isopropanol, blow dry
- Bake at 115°C for 5 minutes
- Spin on NR9-6000PY at 3000 rpm
- Softbake at 150°C for 1 minute
- Expose for 1 minute

- Post Exposure Bake at 100 °C for 60 seconds
- Develop in AZ300 MIF for 30 seconds
- DI rinse
- Ash in PEII for 20 seconds
- 1:4 HCl:DI clean 20 seconds immediately before deposition
- Deposit metal
- Liftoff in NMP for 3 hours
- Solvent clean: Isopropanol, blow dry

Anneal

- RTA 410°C for 30 seconds in Forming Gas

A.2 N and P Etch

The dry etch for the N and P contact etch steps are performed in ICP 2. Flow rates are as follows: $BCl_3/Cl_2/N_2$ 15/15/10. The etch is performed at a pressure of 0.4, and ICP power and forward bias are given by 900/100W succesfully.

ICP 2 has a laser reflectivity monitor, which is used to monitor the etch depth during the process. Figure A.1 shows the simulated reflectivity as a function of etch depth. The thicker contact regions exhibit a rising amplitude in the oscillatory pattern. Besides counting the number of oscillations, the patterns of amplitude can be used to stop the etch in the correct place.

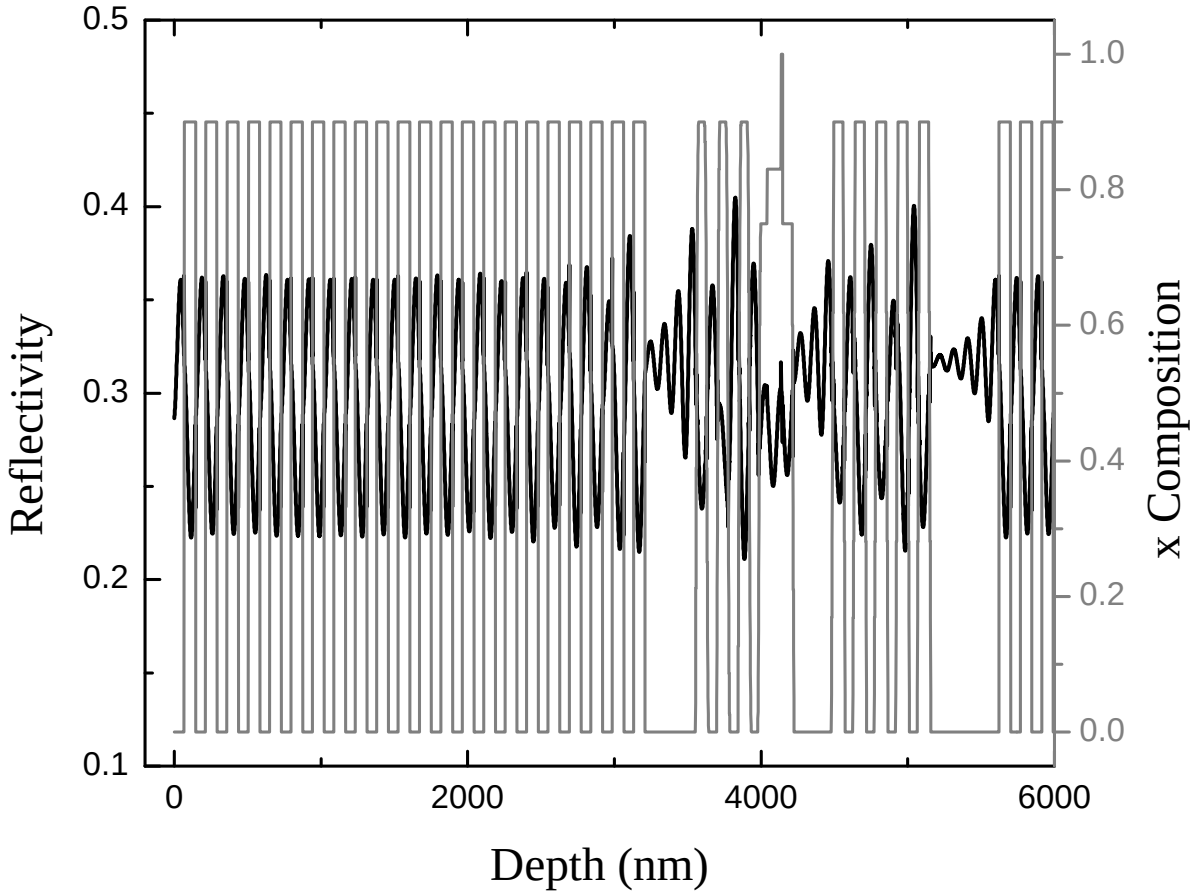

Figure A.1: Simulated reflectivity as a function of etch depth for the ICP etch monitoring system.

A.3 Metallizations

N metal: Deposit Ni/AuGe/Ag/Au 50/ 800/1000/5000Å. The N metal deposition is typically performed in E Beam 1, evaporating 1 pellot of eutectic AuGe entirely. Ag can be optional, but may be desirable if wire bonding issues arrise. The use of Ag has been reported to be a succesful barrier layer in Ohmic contacts to GaAs [140, 141].

P metal: Deposit Ti/Pt/Au 100/200/5000Å. Typically done in E Beam 3.

Top ITO metal: Deposit Cr/Ni/Au 250/200/5000Å. Typically done in E Beam 3.

Fabricated chips are cleaved in a Loomis cleaver. After mounting, Au wires are bonded to the contact pads in a wedge bonder. The Au-Au bond typically requires heat. A temperature of 150°C is a reasonable temperature. Ag-Au bonds, however, can be done without heat.

The main text of the thesis featured a standard chip carrier (Evergreen Semiconductor) with bond pads. Regular submounts have also been fabricated on Alumina or AlN substrates. The wedge bond requires a positive height difference between sample and bond pad for optimal performance. The constraint can be alleviated with a ball bonder. Additional pieces of substrate, with evaporated bond pads, can be glued to the submount. PCB boards with specified wire layouts can also be glued to a submount, providing a convenient bonding pad. Varnish or epoxy can be used as an adhesive. To avoid damage to samples, the following packaging order is recommended: Solder wires to submount or carrier, mount the sample, Ash sample, then perform wire bonding. It is recommended to perform an ash in PE-II immediately before wire bonding. For extreme precaution, the electrical instruments should be powered and set to 0 V when connecting the device, and should remain on at all times. Precautions against static discharge are also recommended.

Appendix B

Electrical Properties

B.1 IV Curves

Devices are initially tested electrically by verifying their current-voltage (I-V) curves. The I-V curves give the first indication of the quality of a device, both electrically, but also optically, as low quality material allows for undesirable current in the device. The p-i-n junction design produces diode-like characteristics. In forward bias, the bands flatten and decrease the potential barrier in the device so that carriers can flow. The turn-on voltage should appear at around 1 V. At low temperature, the turn-on voltage should be higher. In reverse bias, the potential barrier in the device increases, but eventually carriers can tunnel through, leading to a reverse bias breakdown. An example I-V curve is shown in Figure B.1.

Different heterostructure designs have been used to provide better charging capabilities of quantum dots. Two such designs include the AlGaAs tunnel barrer [142], and the p-i-n-i-n structure [143]. An AlGaAs tunnel barrier design has been implemented in our group. The tunnel barrier can greatly reduce the amount of current flowing through a device and increase the tuning range of a quantum dot. Figure B.2 shows an I-V curve

with a tunnel barrier. The I-V curve for the tunnel barrier deomonstrates a greater-turn on voltage, as well as greater reverse breakdown voltage, compared to the other devices. The total amount of current is also greatly reduced.

I-V curves also indicate the quality of electro-optic tuning devices. Typically, the I-V curve is measured from the top contact to the buried p contact. A very large voltage can be applied to devices without drawing current. An I-V curve for a device, measured from the top contact to the p contact is shown in Figure B.3. Good polarization tunable devices can operate with up to 50 V in forward bias at low temperature, with only a few μA being drawn. Including the reverse bias, up to 80 V tuning range can be achieved.

Results in publications are performed using a 27 nm tunnel barrier. Enhanced performance is expected with a 27 nm AlGaAs tunnel barrier. The two structures, from n contact layer are indicated in the table below. Exact growth layers can be found in [88].

Layer	27 nm Tunnel Barrier	AlGaAs Barrier
i-GaAs	15	15
i-InGaAs QDs	1.6	1.6
i-GaAs Tunnel Barrier	NA	5
i-AlGaAs Tunnel Barrer	NA	21.8
i-GaAs	27	5
n-GaAs	50.3	47.3

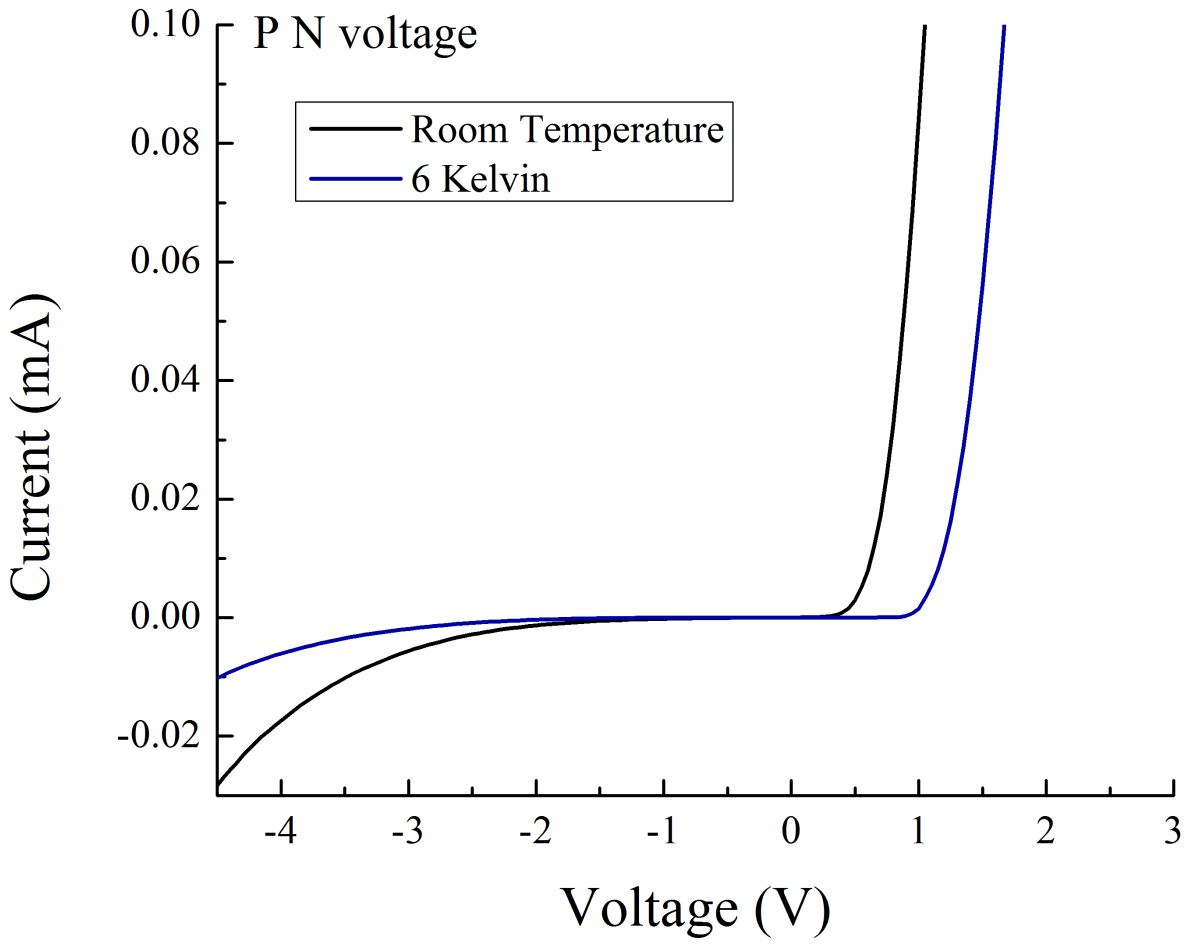

Figure B.1: IV curve of a microcavity device, from the p contact to the n contact, at room temperature and 6 Kelvin.

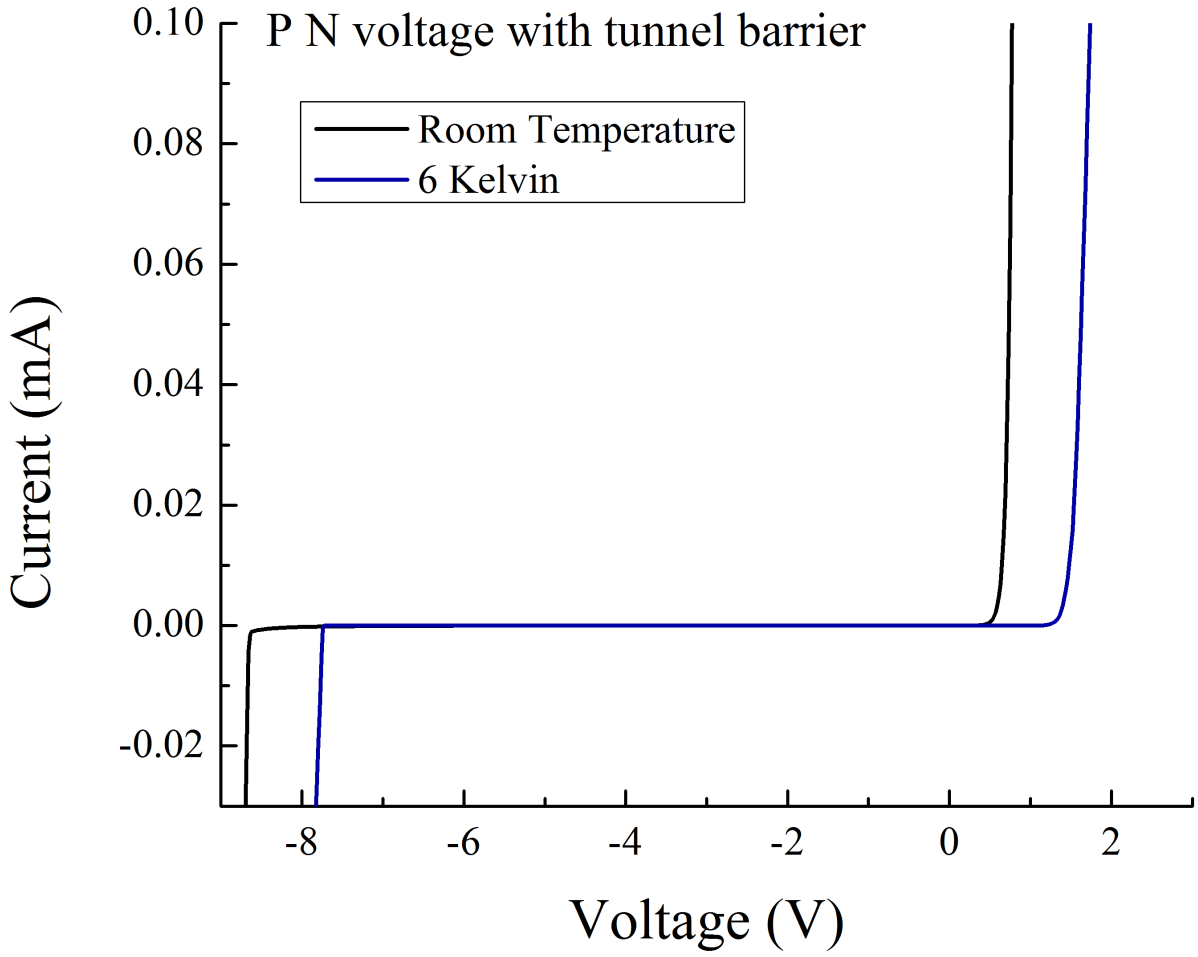

Figure B.2: IV curve of a microcavity device, from the p contact to the n contact including the tunnel barrier, at room temperature and 6 Kelvin.

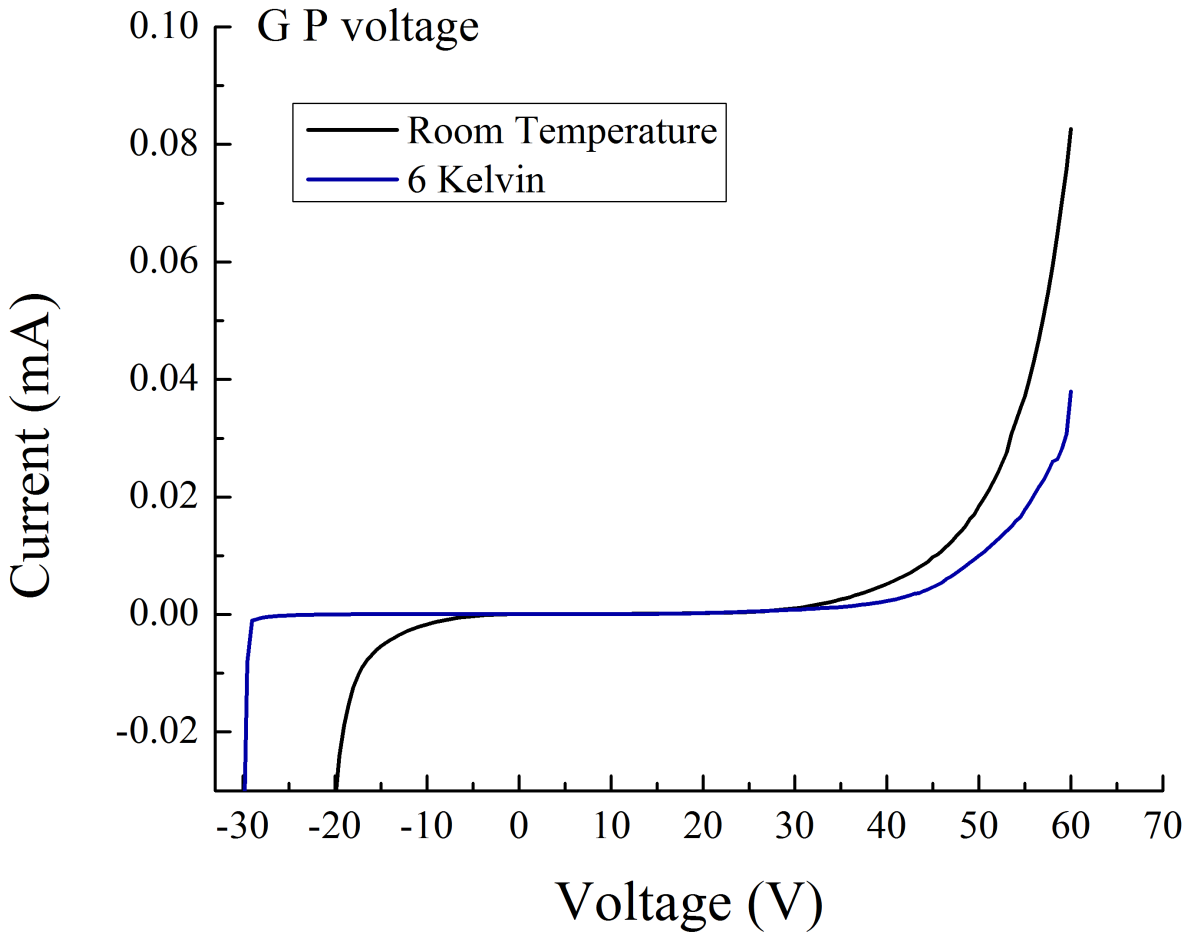

Figure B.3: IV curve of a polarization tunable microcavity device, from the ITO contact to the p contact, at room temperature and 6 Kelvin.

Bibliography

[1] S. J. Freedman and J. F. Clauser, *Experimental test of local hidden-variable theories*, *Physical Review Letters* **28** (1972), no. 14 938–941.

[2] A. Aspect, P. Grangier, and G. Roger, *Experimental realization of Einstein-Podolsky-Rosen-Bohm Gedankenexperiment: A new violation of Bell's inequalities*, *Physical Review Letters* **49** (1982), no. 2 91–94.

[3] A. Aspect, J. Dalibard, and G. Roger, *Experimental test of Bell's inequalities using time- varying analyzers*, *Physical Review Letters* **49** (1982), no. 25 1804–1807.

[4] Z. Y. Ou and L. Mandel, *Violation of bell's inequality and classical probability in a two-photon correlation experiment*, *Physical Review Letters* **61** (1988), no. 1 50–53.

[5] Y. H. Shih and C. O. Alley, *New type of einstein-podolsky-rosen-bohm experiment using pairs of light quanta produced by optical parametric down conversion*, *Physical Review Letters* **61** (1988), no. 26 2921–2924.

[6] J. L. O'Brien, A. Furusawa, and J. Vučković, *Photonic quantum technologies*, *Nature Photonics* **3** (dec, 2009) 687–695.

[7] E. Knill, R. Laflamme, and G. J. Milburn, *A scheme for efficient quantum computation with linear optics*, *Nature* **409** (jan, 2001) 46–52.

[8] R. Raussendorf and H. J. Briegel, *A One-Way Quantum Computer*, *Physical Review Letters* **86** (may, 2001) 5188–5191.

[9] M. A. Nielsen, *Optical Quantum Computation Using Cluster States*, *Physical Review Letters* **93** (jul, 2004) 040503.

[10] T. Rudolph, *Why I am optimistic about the silicon-photonic route to quantum computing*, *APL Photonics* **2** (mar, 2017) 030901.

[11] C. Taballione, T. A. W. Wolterink, J. Lugani, A. Eckstein, B. A. Bell, R. Grootjans, I. Visscher, D. Geskus, C. G. H. Roeloffzen, J. J. Renema, I. A.

Walmsley, P. W. H. Pinkse, and K.-J. Boller, *88 reconfigurable quantum photonic processor based on silicon nitride waveguides*, *Optics Express* **27** (2019), no. 19 26842.

[12] N. C. Harris, G. R. Steinbrecher, M. Prabhu, Y. Lahini, J. Mower, D. Bunandar, C. Chen, F. N. C. Wong, T. Baehr-Jones, M. Hochberg, S. Lloyd, and D. Englund, *Quantum transport simulations in a programmable nanophotonic processor*, *Nature Photonics* **11** (jul, 2017) 447–452.

[13] C. Sparrow, E. Martín-López, N. Maraviglia, A. Neville, C. Harrold, J. Carolan, Y. N. Joglekar, T. Hashimoto, N. Matsuda, J. L. O'Brien, D. P. Tew, and A. Laing, *Simulating the vibrational quantum dynamics of molecules using photonics*, *Nature* **557** (may, 2018) 660–667.

[14] H. Wang, Y.-M. He, T.-H. Chung, H. Hu, Y. Yu, S. Chen, X. Ding, M.-C. Chen, J. Qin, X. Yang, R.-Z. Liu, Z.-C. Duan, J.-P. Li, S. Gerhardt, K. Winkler, J. Jurkat, L.-J. Wang, N. Gregersen, Y.-H. Huo, Q. Dai, S. Yu, S. Höfling, C.-Y. Lu, and J.-W. Pan, *Towards optimal single-photon sources from polarized microcavities*, *Nature Photonics* **13** (nov, 2019) 770–775.

[15] N. C. Harris, J. Carolan, D. Bunandar, M. Prabhu, M. Hochberg, T. Baehr-Jones, M. L. Fanto, A. M. Smith, C. C. Tison, P. M. Alsing, and D. Englund, *Linear programmable nanophotonic processors*, *Optica* **5** (dec, 2018) 1623.

[16] F. Marsili, V. B. Verma, J. A. Stern, S. Harrington, A. E. Lita, T. Gerrits, I. Vayshenker, B. Baek, M. D. Shaw, R. P. Mirin, and S. W. Nam, *Detecting single infrared photons with 93% system efficiency*, *Nature Photonics* **7** (mar, 2013) 210–214.

[17] I. Esmaeil Zadeh, J. W. Los, R. B. Gourgues, V. Steinmetz, G. Bulgarini, S. M. Dobrovolskiy, V. Zwiller, and S. N. Dorenbos, *Single-photon detectors combining high efficiency, high detection rates, and ultra-high timing resolution*, *APL Photonics* **2** (nov, 2017).

[18] T. J. Weinhold, A. Gilchrist, K. J. Resch, A. C. Doherty, J. L. O'Brien, G. J. Pryde, and A. G. White, *Understanding photonic quantum-logic gates: The road to fault tolerance*, arXiv:0808.0794.

[19] A. Reiserer and G. Rempe, *Cavity-based quantum networks with single atoms and optical photons*, *Reviews of Modern Physics* **87** (dec, 2015) 1379–1418.

[20] H. J. Kimble, M. Dagenais, and L. Mandel, *Photon Antibunching in Resonance Fluorescence*, *Physical Review Letters* **39** (sep, 1977) 691–695.

[21] R. Short and L. Mandel, *Observation of sub-Poissonian photon statistics*, *Physical Review Letters* **51** (1983), no. 5 384–387.

[22] A. Imamoglu and Y. Yamamoto, *Turnstile device for heralded single photons: Coulomb blockade of electron and hole tunneling in quantum confined p - i - n heterojunctions*, *Physical Review Letters* **72** (jan, 1994) 210–213.

[23] J. Kim, O. Benson, H. Kan, and Y. Yamamoto, *A single-photon turnstile device*, *Nature* **397** (feb, 1999) 500–503.

[24] C. Santori, M. Pelton, G. Solomon, Y. Dale, and Y. Yamamoto, *Triggered Single Photons from a Quantum Dot*, *Physical Review Letters* **86** (feb, 2001) 1502–1505.

[25] M. Pelton, C. Santori, J. Vucković, B. Zhang, G. S. Solomon, J. Plant, and Y. Yamamoto, *Efficient Source of Single Photons: A Single Quantum Dot in a Micropost Microcavity*, *Physical Review Letters* **89** (nov, 2002) 233602.

[26] P. Michler, A. Kiraz, C. Becher, W. V. Schoenfeld, P. M. Petroff, L. Zhang, E. Hu, and A. Imamoglu, *A quantum dot single-photon turnstile device.*, *Science (New York, N.Y.)* **290** (dec, 2000) 2282–5.

[27] S. Strauf, N. G. Stoltz, M. T. Rakher, L. A. Coldren, P. M. Petroff, and D. Bouwmeester, *High-frequency single-photon source with polarization control*, *Nature Photonics* **1** (dec, 2007) 704–708.

[28] A. Muller, E. B. Flagg, P. Bianucci, X. Y. Wang, D. G. Deppe, W. Ma, J. Zhang, G. J. Salamo, M. Xiao, and C. K. Shih, *Resonance Fluorescence from a Coherently Driven Semiconductor Quantum Dot in a Cavity*, *Physical Review Letters* **99** (nov, 2007) 187402.

[29] S. Ates, S. M. Ulrich, S. Reitzenstein, A. Löffler, A. Forchel, and P. Michler, *Post-Selected Indistinguishable Photons from the Resonance Fluorescence of a Single Quantum Dot in a Microcavity*, *Physical Review Letters* **103** (oct, 2009) 167402.

[30] M. Bayer, G. Ortner, O. Stern, A. Kuther, A. A. Gorbunov, A. Forchel, P. Hawrylak, S. Fafard, K. Hinzer, T. L. Reinecke, S. N. Walck, J. P. Reithmaier, F. Klopf, and F. Schäfer, *Fine structure of neutral and charged excitons in self-assembled In(Ga)As/(Al)GaAs quantum dots*, *Physical Review B* **65** (may, 2002) 195315.

[31] A. Boca, R. Miller, K. M. Birnbaum, A. D. Boozer, J. McKeever, and H. J. Kimble, *Observation of the Vacuum Rabi Spectrum for One Trapped Atom*, *Physical Review Letters* **93** (dec, 2004) 233603.

[32] K. M. Birnbaum, A. Boca, R. Miller, A. D. Boozer, T. E. Northup, and H. J. Kimble, *Photon blockade in an optical cavity with one trapped atom*, *Nature* **436** (jul, 2005) 87–90.

[33] A. Faraon, I. Fushman, D. Englund, N. Stoltz, P. Petroff, and J. Vučković, *Coherent generation of non-classical light on a chip via photon-induced tunnelling and blockade*, *Nature Physics* **4** (nov, 2008) 859–863.

[34] L. De Santis, C. Antón, B. Reznychenko, N. Somaschi, G. Coppola, J. Senellart, C. Gómez, A. Lemaître, I. Sagnes, A. G. White, L. Lanco, A. Auffèves, and P. Senellart, *A solid-state single-photon filter*, *Nature Nanotechnology* **12** (may, 2017) 663–667.

[35] P. Senellart, G. Solomon, and A. White, *High-performance semiconductor quantum-dot single-photon sources*, *Nature Nanotechnology* **12** (nov, 2017) 1026–1039.

[36] J. J. Sakurai and J. Napolitano, *Modern Quantum Mechanics*. Addison-Wesley, San Francisco, second ed., 2011.

[37] E. M. Purcell, *Spontaneous Emission Probabilities at Radio Frequencies*, *Physical Review* **69** (jun, 1946) 681.

[38] J. Gérard, B. Sermage, B. Gayral, B. Legrand, E. Costard, and V. Thierry-Mieg, *Enhanced Spontaneous Emission by Quantum Boxes in a Monolithic Optical Microcavity*, *Physical Review Letters* **81** (aug, 1998) 1110–1113.

[39] R. M. Thompson, R. M. Stevenson, A. J. Shields, I. Farrer, C. J. Lobo, D. A. Ritchie, M. L. Leadbeater, and M. Pepper, *Single-photon emission from exciton complexes in individual quantum dots*, *Physical Review B* **64** (oct, 2001) 201302.

[40] C. Santori, G. S. Solomon, M. Pelton, and Y. Yamamoto, *Time-resolved spectroscopy of multiexcitonic decay in an InAs quantum dot*, *Physical Review B* **65** (feb, 2002) 073310.

[41] P. A. Dalgarno, J. M. Smith, J. McFarlane, B. D. Gerardot, K. Karrai, A. Badolato, P. M. Petroff, and R. J. Warburton, *Coulomb interactions in single charged self-assembled quantum dots: Radiative lifetime and recombination energy*, *Physical Review B* **77** (jun, 2008) 245311.

[42] A. V. Kuhlmann, J. Houel, A. Ludwig, L. Greuter, D. Reuter, A. D. Wieck, M. Poggio, and R. J. Warburton, *Charge noise and spin noise in a semiconductor quantum device*, *Nature Physics* **9** (sep, 2013) 570–575.

[43] C. Antón, P. Hilaire, C. A. Kessler, J. Demory, C. Gómez, A. Lemaître, I. Sagnes, N. D. Lanzillotti-Kimura, O. Krebs, N. Somaschi, P. Senellart, and L. Lanco, *Tomography of the optical polarization rotation induced by a single quantum dot in a cavity*, *Optica* **4** (nov, 2017) 1326.

[44] E. Moreau, I. Robert, L. Manin, V. Thierry-Mieg, J. M. Gérard, and I. Abram, *Quantum Cascade of Photons in Semiconductor Quantum Dots*, *Physical Review Letters* **87** (oct, 2001) 183601.

[45] C. Santori, G. S. Solomon, M. Pelton, and Y. Yamamoto, *Time-resolved spectroscopy of multiexcitonic decay in an InAs quantum dot*, *Physical Review B* **65** (feb, 2002) 073310.

[46] H. Jayakumar, A. Predojevic, T. Huber, T. Kauten, G. S. Solomon, and G. Weihs, *Deterministic Photon Pairs and Coherent Optical Control of a Single Quantum Dot*, *Physical Review Letters* **110** (mar, 2013) 135505.

[47] M. Müller, S. Bounouar, K. D. Jöns, M. Glässl, and P. Michler, *On-demand generation of indistinguishable polarization-entangled photon pairs*, *Nature Photonics* **8** (mar, 2014) 224–228.

[48] A. Dousse, J. S. Suffczynski, A. Beveratos, O. Krebs, A. L. Lematre, I. Sagnes, J. Bloch, P. Voisin, and P. Senellart, *Ultrabright source of entangled photon pairs Energy Energy (meV)*, *Nature* **466** (2010).

[49] J. Liu, R. Su, Y. Wei, B. Yao, S. F. C. da Silva, Y. Yu, J. Iles-Smith, K. Srinivasan, A. Rastelli, J. Li, and X. Wang, *A solid-state source of strongly entangled photon pairs with high brightness and indistinguishability*, *Nature Nanotechnology* **14** (jun, 2019) 586–593.

[50] Z. Lin and J. Vučković, *Enhanced two-photon processes in single quantum dots inside photonic crystal nanocavities*, *Physical Review B* **81** (jan, 2010) 035301.

[51] Y.-M. He, H. Wang, C. Wang, M.-C. Chen, X. Ding, J. Qin, Z.-C. Duan, S. Chen, J.-P. Li, R.-Z. Liu, C. Schneider, M. Atatüre, S. Höfling, C.-Y. Lu, and J.-W. Pan, *Coherently driving a single quantum two-level system with dichromatic laser pulses*, *Nature Physics* **15** (sep, 2019) 941–946.

[52] C. C. Gerry and P. L. Knight, *Introductory Quantum Optics*. Cambridge University Press, Cambridge, 2005.

[53] R. J. Glauber, *Coherent and Incoherent States of the Radiation Field*, *Physical Review* **131** (sep, 1963) 2766–2788.

[54] R. J. Glauber, *The Quantum Theory of Optical Coherence*, *Physical Review* **130** (jun, 1963) 2529–2539.

[55] R. Hanbury Brown and R. Q. Twiss, *A test of a new type of stellar interferometer on Sirius*, *Nature* **178** (1956), no. 4541 1046–1048.

[56] R. H. BROWN and R. Q. TWISS, *Correlation between Photons in two Coherent Beams of Light*, *Nature* **177** (jan, 1956) 27–29.

[57] X. T. Zou and L. Mandel, *Photon-antibunching and sub-Poissonian photon statistics*, *Physical Review A* **41** (jan, 1990) 475–476.

[58] E. B. Flagg, A. Muller, J. W. Robertson, S. Founta, D. G. Deppe, M. Xiao, W. Ma, G. J. Salamo, and C. K. Shih, *Resonantly driven coherent oscillations in a solid-state quantum emitter*, *Nature Physics* **5** (2009), no. 3 203–207.

[59] D. Najer, I. Söllner, P. Sekatski, V. Dolique, M. C. Löbl, D. Riedel, R. Schott, S. Starosielec, S. R. Valentin, A. D. Wieck, N. Sangouard, A. Ludwig, and R. J. Warburton, *A gated quantum dot strongly coupled to an optical microcavity*, *Nature* **575** (nov, 2019) 622–627.

[60] H. Snijders, J. Frey, J. Norman, V. Post, A. Gossard, J. Bowers, M. van Exter, W. Löffler, and D. Bouwmeester, *Fiber-Coupled Cavity-QED Source of Identical Single Photons*, *Physical Review Applied* **9** (mar, 2018) 031002.

[61] C. K. Hong, Z. Y. Ou, and L. Mandel, *Measurement of subpicosecond time intervals between two photons by interference*, *Physical Review Letters* **59** (nov, 1987) 2044–2046.

[62] Y. H. Shih and C. O. Alley, *New Type of Einstein-Podolsky-Rosen-Bohm Experiment Using Pairs of Light Quanta Produced by Optical Parametric Down Conversion*, *Physical Review Letters* **61** (dec, 1988) 2921–2924.

[63] T. B. Pittman, D. V. Strekalov, A. Migdall, M. H. Rubin, A. V. Sergienko, and Y. H. Shih, *Can Two-Photon Interference be Considered the Interference of Two Photons?*, *Physical Review Letters* **77** (sep, 1996) 1917–1920.

[64] P. Grangier, G. Roger, and A. Aspect, *Experimental Evidence for a Photon Anticorrelation Effect on a Beam Splitter: A New Light on Single-Photon Interferences*, *Europhysics Letters (EPL)* **1** (feb, 1986) 173–179.

[65] S. Seidl, B. Gerardot, P. Dalgarno, K. Kowalik, A. Holleitner, P. Petroff, K. Karrai, and R. Warburton, *Statistics of quantum dot exciton fine structure splittings and their polarization orientations*, *Physica E: Low-dimensional Systems and Nanostructures* **40** (apr, 2008) 2153–2155.

[66] E. Jaynes and F. Cummings, *Comparison of quantum and semiclassical radiation theories with application to the beam maser*, *Proceedings of the IEEE* **51** (1963), no. 1 89–109.

[67] B. W. Shore and P. L. Knight, *The Jaynes-Cummings Model*, *Journal of Modern Optics* **40** (jul, 1993) 1195–1238.

[68] L. Allen and J. H. Eberly, *Optical Resonance and Two-Level Atoms*. Dover Publications, Inc., New York, 1987.

[69] C. W. Gardiner and M. J. Collett, *Input and output in damped quantum systems: Quantum stochastic differential equations and the master equation*, *Physical Review A* **31** (1985), no. 6 3761–3774.

[70] A. Auffèves-Garnier, C. Simon, J.-M. Gérard, and J.-P. Poizat, *Giant optical nonlinearity induced by a single two-level system interacting with a cavity in the Purcell regime*, *Physical Review A* **75** (may, 2007) 053823.

[71] E. Waks and J. Vuckovic, *Dipole Induced Transparency in Drop-Filter Cavity-Waveguide Systems*, *Physical Review Letters* **96** (apr, 2006) 153601.

[72] D. Englund, A. Faraon, I. Fushman, N. Stoltz, P. Petroff, and J. Vučković, *Controlling cavity reflectivity with a single quantum dot*, *Nature* **450** (dec, 2007) 857–861.

[73] V. Loo, C. Arnold, O. Gazzano, A. Lemaître, I. Sagnes, O. Krebs, P. Voisin, P. Senellart, and L. Lanco, *Optical Nonlinearity for Few-Photon Pulses on a Quantum Dot-Pillar Cavity Device*, *Physical Review Letters* **109** (oct, 2012) 166806.

[74] H. J. Snijders, D. N. L. Kok, M. F. van de Stolpe, J. A. Frey, J. Norman, A. C. Gossard, J. E. Bowers, M. P. van Exter, D. Bouwmeester, and W. Löffler, *Polarized quantum dot cavity-QED and single photons*, arXiv:1811.1057.

[75] J. T. Shen and S. Fan, *Coherent photon transport from spontaneous emission in one-dimensional waveguides*, *Optics Letters* **30** (aug, 2005) 2001.

[76] C. W. Gardiner and P. Zoller, *Quantum Noise*. Springer-Verlag Berlin Heidelberg, third ed., 2004.

[77] M. A. Armen and H. Mabuchi, *Low-lying bifurcations in cavity quantum electrodynamics*, *Physical Review A* **73** (jun, 2006) 063801.

[78] J. Johansson, P. Nation, and F. Nori, *QuTiP: An open-source Python framework for the dynamics of open quantum systems*, *Computer Physics Communications* **183** (aug, 2012) 1760–1772.

[79] J. Johansson, P. Nation, and F. Nori, *QuTiP 2: A Python framework for the dynamics of open quantum systems*, *Computer Physics Communications* **184** (apr, 2013) 1234–1240.

[80] H. A. Haus, *Waves and Fields in Optoelectronics*. Prentice-Hall, Inc., Englewood Cliffs, 1984.

[81] M. P. Bakker, *Cavity quantum electrodynamics with quantum dots in microcavities*. PhD thesis, Leiden University, 2015.

[82] H. Snijders, *Quantum Dot Microcavity Control Of Photon Statistics*. PhD thesis, Leiden University, 2018.

[83] E. O. Kane, *Band structure of indium antimonide*, *Journal of Physics and Chemistry of Solids* **1** (1957), no. 4 249–261.

[84] J. H. Davies, *The Physics of Low-Dimensional Semiconductors*. Cambridge University Press, Cambridge, 1998.

[85] C. G. Van de Walle and R. M. Martin, *Theoretical study of band offsets at semiconductor interfaces*, *Physical Review B* **35** (may, 1987) 8154–8165.

[86] C. G. Van de Walle, *Band lineups and deformation potentials in the model-solid theory*, *Physical Review B* **39** (jan, 1989) 1871–1883.

[87] K.-N. Tu, J. W. Mayer, and L. C. Feldman, *Electronic Thin Film Science For Electrical Engineers and Materials Scientists*. Macmillan, New York, 1992.

[88] J. C. Norman, *Quantum Dot Lasers for Silicon Photonics*. PhD thesis, University of California Santa Barbara, 2018.

[89] A. Wojs, L. Jacak, P. Hawrylak, and S. Fafard, *Electronic structure and magneto-optics of self-assembled quantum dots*, *Physical Review B - Condensed Matter and Materials Physics* **54** (1996), no. 8 5604–5608.

[90] S. Raymond, X. Guo, J. L. Merz, and S. Fafard, *Excited-state radiative lifetimes in self-assembled quantum dots obtained from state-filling spectroscopy*, *Physical Review B* **59** (mar, 1999) 7624–7631.

[91] D. A. B. Miller, D. S. Chemla, T. C. Damen, A. C. Gossard, W. Wiegmann, T. H. Wood, and C. A. Burrus, *Band-Edge Electroabsorption in Quantum Well Structures: The Quantum-Confined Stark Effect*, *Physical Review Letters* **53** (nov, 1984) 2173–2176.

[92] R. J. Warburton, *Single spins in self-assembled quantum dots*, *Nature Materials* **12** (jun, 2013) 483–493.

[93] A. Dousse, L. Lanco, J. Suffczyński, E. Semenova, A. Miard, A. Lemaître, I. Sagnes, C. Roblin, J. Bloch, and P. Senellart, *Controlled Light-Matter Coupling for a Single Quantum Dot Embedded in a Pillar Microcavity Using Far-Field Optical Lithography*, *Physical Review Letters* **101** (dec, 2008) 267404.

[94] K. Vahala, *Optical Microcavities*. World Scientific Publishing Co., 2004.

[95] P. Laporta and V. Magni, *Dispersive effects in the reflection of femtosecond optical pulses from broadband dielectric mirrors*, *Applied Optics* **24** (jul, 1985) 2014.

[96] L. A. Coldren, S. W. Corzine, and M. L. Masanovic, *Diode Lasers and Photonic Integrated Circuits*. John Wiley & Sons, Ltd, Hoboken, second ed., 2012.

[97] L. A. Coldren, B. J. Thibeault, E. R. Hegblom, G. B. Thompson, and J. W. Scott, *Dielectric apertures as intracavity lenses in verticalcavity lasers*, *Applied Physics Letters* **68** (jan, 1996) 313–315.

[98] M. P. Bakker, A. V. Barve, A. Zhan, L. A. Coldren, M. P. van Exter, and D. Bouwmeester, *Polarization degenerate micropillars fabricated by designing elliptical oxide apertures*, *Applied Physics Letters* **104** (apr, 2014) 151109.

[99] C. Chua, R. Thornton, and D. Treat, *Planar laterally oxidized vertical-cavity lasers for low-threshold high-density top-surface-emitting arrays*, *IEEE Photonics Technology Letters* **9** (aug, 1997) 1060–1062.

[100] C. L. Chua, R. L. Thornton, D. W. Treat, and R. M. Donaldson, *Anisotropic apertures for polarization-stable laterally oxidized vertical-cavity lasers*, *Applied Physics Letters* **73** (sep, 1998) 1631–1633.

[101] J. Gudat, *Cavity quantum electrodynamics with quantum dots in microcavities*. PhD thesis, Leiden University, 2012.

[102] Pei-Cheng Ku and C. Chang-Hasnain, *Thermal oxidation of AlgaAs: modeling and process control*, *IEEE Journal of Quantum Electronics* **39** (apr, 2003) 577–585.

[103] K. Choquette, K. Geib, C. Ashby, R. Twesten, O. Blum, H. Hou, D. Follstaedt, B. Hammons, D. Mathes, and R. Hull, *Advances in selective wet oxidation of AlGaAs alloys*, *IEEE Journal of Selected Topics in Quantum Electronics* **3** (jun, 1997) 916–926.

[104] J. F. Nye, *Physical Properties of Crystals*. Oxford University Press, Oxford, 1985.

[105] S. Adachi and K. Oe, *Linear electro-optic effects in zincblende-type semiconductors: Key properties of InGaAsP relevant to device design*, *Journal of Applied Physics* **56** (1984), no. 74.

[106] M. P. van Exter, A. K. Jansen van Doorn, and J. P. Woerdman, *Electro-optic effect and birefringence in semiconductor vertical-cavity lasers*, *Physical Review A* **56** (jul, 1997) 845–853.

[107] R. F. M. Hendriks, M. P. van Exter, J. P. Woerdman, A. van Geelen, L. Weegels, K. H. Gulden, and M. Moser, *Electro-optic birefringence in semiconductor vertical-cavity lasers*, *Applied Physics Letters* **71** (nov, 1997) 2599–2601.

[108] G. P. Bava, P. Debernardi, and L. Fratta, *Three-dimensional model for vectorial fields in vertical-cavity surface-emitting lasers*, *Physical Review A* **63** (jan, 2001) 023816.

[109] P. Debernardi, G. Bava, C. Degen, I. Fischer, and W. Elsasser, *Influence of anisotropies on transverse modes in oxide-confined VCSELs*, *IEEE Journal of Quantum Electronics* **38** (2002), no. 1 73–84.

[110] J. Faist and F. Reinhart, *Phase modulation in GaAs/AlGaAs double heterostructures. I. Theory*, *Journal of Applied Physics* **67** (jun, 1990) 6998–7005.

[111] S. Ramelow, A. Farsi, S. Clemmen, J. S. Levy, A. R. Johnson, Y. Okawachi, M. R. E. Lamont, M. Lipson, and A. L. Gaeta, *Strong polarization mode coupling in microresonators*, *Optics Letters* **39** (sep, 2014) 5134.

[112] K. D. Choquette, D. A. Richie, and R. E. Leibenguth, *Temperature dependence of gainguided verticalcavity surface emitting laser polarization*, *Applied Physics Letters* **64** (apr, 1994) 2062–2064.

[113] J. R. Pierce, *Coupling of Modes of Propagation*, *Journal of Applied Physics* **25** (feb, 1954) 179–183.

[114] H. A. Haus and W. Huang, *Coupled-Mode Theory*, *Proceedings of the IEEE* **79** (1991), no. 10 1505–1518.

[115] A. K. Jansen van Doorn, M. P. van Exter, A. M. van der Lee, and J. P. Woerdman, *Coupled-mode description for the polarization state of a vertical-cavity semiconductor laser*, *Physical Review A - Atomic, Molecular, and Optical Physics* **55** (1997), no. 2 1473–1484.

[116] K. D. Choquette, K. M. Geib, H. C. Chui, B. E. Hammons, H. Q. Hou, T. J. Drummond, and R. Hull, *Selective oxidation of buried AlGaAs versus AlAs layers*, *Applied Physics Letters* **69** (sep, 1996) 1385–1387.

[117] N. Somaschi, V. Giesz, L. De Santis, J. C. Loredo, M. P. Almeida, G. Hornecker, S. L. Portalupi, T. Grange, C. Antón, J. Demory, C. Gómez, I. Sagnes, N. D. Lanzillotti-Kimura, A. Lemaítre, A. Auffeves, A. G. White, L. Lanco, and P. Senellart, *Near-optimal single-photon sources in the solid state*, *Nature Photonics* **10** (may, 2016) 340–345.

[118] C. Schneider, P. Gold, S. Reitzenstein, S. Höfling, and M. Kamp, *Quantum dot micropillar cavities with quality factors exceeding 250,000*, *Applied Physics B* **122** (jan, 2016) 19.

[119] C. Bonato, D. Ding, J. Gudat, S. Thon, H. Kim, P. M. Petroff, M. P. van Exter, and D. Bouwmeester, *Tuning micropillar cavity birefringence by laser induced surface defects*, *Applied Physics Letters* **95** (dec, 2009) 251104.

[120] M. S. Park, B. T. Ahn, B.-S. Yoo, H. Y. Chu, H.-H. Park, and C. J. Chang-Hasnain, *Polarization control of vertical-cavity surface-emitting lasers by electro-optic birefringence*, *Applied Physics Letters* **76** (feb, 2000) 813–815.

[121] R. Trotta, J. S. Wildmann, E. Zallo, O. G. Schmidt, and A. Rastelli, *Highly Entangled Photons from Hybrid Piezoelectric-Semiconductor Quantum Dot Devices*, *Nano Letters* **14** (jun, 2014) 3439–3444.

[122] J. A. Frey, H. J. Snijders, J. Norman, A. C. Gossard, J. E. Bowers, W. Löffler, and D. Bouwmeester, *Electro-optic polarization tuning of microcavities with a single quantum dot*, *Optics Letters* **43** (sep, 2018) 4280.

[123] D. Babic and S. Corzine, *Analytic expressions for the reflection delay, penetration depth, and absorptance of quarter-wave dielectric mirrors*, *IEEE Journal of Quantum Electronics* **28** (1992), no. 2 514–524.

[124] S. Corzine, R. Yan, and L. Coldren, *A tanh substitution technique for the analysis of abrupt and graded interface multilayer dielectric stacks*, *IEEE Journal of Quantum Electronics* **27** (1991), no. 9 2086–2090.

[125] C.-A. Berseth, C. Wuethrich, and F. K. Reinhart, *The electrooptic coefficients of GaAs: Measurements at 1.32 and 1.52 μm and study of their dispersion between 0.9 and 10 μm*, *Journal of Applied Physics* **71** (mar, 1992) 2821–2825.

[126] M. Glick, F. K. Reinhart, G. Weimann, and W. Schlapp, *Quadratic electrooptic light modulation in a GaAs/AlGaAs multiquantum well heterostructure near the excitonic gap*, *Applied Physics Letters* **48** (apr, 1986) 989–991.

[127] T. H. Wood, R. W. Tkach, and A. R. Chraplyvy, *Observation of large quadratic electrooptic effect in GaAs/AlGaAs multiple quantum wells*, *Applied Physics Letters* **50** (mar, 1987) 798–800.

[128] V. Jayaraman, D. A. Cohen, and L. A. Coldren, *Demonstration of broadband tunability in a semiconductor laser using sampled gratings*, *Applied Physics Letters* **60** (may, 1992) 2321–2323.

[129] H. J. Snijders, J. A. Frey, J. Norman, H. Flayac, V. Savona, A. C. Gossard, J. E. Bowers, M. P. van Exter, D. Bouwmeester, and W. Löffler, *Observation of the Unconventional Photon Blockade*, *Physical Review Letters* **121** (jul, 2018) 043601.

[130] H. Snijders, J. A. Frey, J. Norman, M. P. Bakker, E. C. Langman, A. Gossard, J. E. Bowers, M. P. van Exter, D. Bouwmeester, and W. Löffler, *Purification of a single-photon nonlinearity*, *Nature Communications* **7** (aug, 2016) 12578.

[131] C. Vaneph, A. Morvan, G. Aiello, M. Féchant, M. Aprili, J. Gabelli, and J. Estève, *Observation of the Unconventional Photon Blockade in the Microwave Domain*, *Physical Review Letters* **121** (2018).

[132] T. C. H. Liew and V. Savona, *Single Photons from Coupled Quantum Modes*, *Physical Review Letters* **104** (may, 2010) 183601.

[133] A. Majumdar, M. Bajcsy, A. Rundquist, and J. Vučković, *Loss-Enabled Sub-Poissonian Light Generation in a Bimodal Nanocavity*, *Physical Review Letters* **108** (may, 2012) 183601.

[134] M. Bamba, A. Imamolu, I. Carusotto, and C. Ciuti, *Origin of strong photon antibunching in weakly nonlinear photonic molecules*, *Physical Review A* **83** (feb, 2011) 021802.

[135] H. Flayac and V. Savona, *Input-output theory of the unconventional photon blockade*, *Physical Review A* **88** (sep, 2013) 033836.

[136] M.-A. Lemonde, N. Didier, and A. A. Clerk, *Antibunching and unconventional photon blockade with Gaussian squeezed states*, *Physical Review A* **90** (dec, 2014) 063824.

[137] D. Gerace and V. Savona, *Unconventional photon blockade in doubly resonant microcavities with second-order nonlinearity*, *Physical Review A* **89** (mar, 2014) 031803.

[138] H. Flayac and V. Savona, *Unconventional photon blockade*, *Physical Review A* **96** (nov, 2017) 053810.

[139] J. Aasi, J. Abadie, B. P. Abbott, R. Abbott, T. D. Abbott, M. R. Abernathy, C. Adams, T. Adams, P. Addesso, R. X. Adhikari, C. Affeldt, O. D. Aguiar, P. Ajith, B. Allen, E. Amador Ceron, D. Amariutei, S. B. Anderson, W. G. Anderson, K. Arai, M. C. Araya, C. Arceneaux, S. Ast, S. M. Aston, D. Atkinson, P. Aufmuth, C. Aulbert, L. Austin, B. E. Aylott, S. Babak, P. T. Baker, S. Ballmer, Y. Bao, J. C. Barayoga, D. Barker, B. Barr, L. Barsotti, M. A. Barton, I. Bartos, R. Bassiri, J. Batch, J. Bauchrowitz, B. Behnke, A. S. Bell, C. Bell, G. Bergmann, J. M. Berliner, A. Bertolini, J. Betzwieser, N. Beveridge, P. T. Beyersdorf, T. Bhadbhade, I. A. Bilenko, G. Billingsley, J. Birch, S. Biscans, E. Black, J. K. Blackburn, L. Blackburn, D. Blair, B. Bland, O. Bock, T. P. Bodiya, C. Bogan, C. Bond, R. Bork, M. Born, S. Bose, J. Bowers, P. R. Brady, V. B. Braginsky, J. E. Brau, J. Breyer, D. O. Bridges, M. Brinkmann, M. Britzger, A. F. Brooks, D. A. Brown, D. D. Brown, K. Buckland, F. Brückner, B. C. Buchler, A. Buonanno, J. Burguet-Castell, R. L. Byer, L. Cadonati, J. B. Camp, P. Campsie, K. Cannon, J. Cao, C. D. Capano, L. Carbone, S. Caride, A. D. Castiglia, S. Caudill, M. Cavaglià, C. Cepeda, T. Chalermsongsak, S. Chao, P. Charlton, X. Chen, Y. Chen, H.-S. Cho, J. H. Chow, N. Christensen, Q. Chu, S. S. Y. Chua, C. T. Y. Chung, G. Ciani, F. Clara, D. E. Clark, J. A. Clark, M. Constancio Junior, D. Cook, T. R. Corbitt, M. Cordier, N. Cornish, A. Corsi, C. A. Costa, M. W. Coughlin, S. Countryman, P. Couvares, D. M. Coward,

M. Cowart, D. C. Coyne, K. Craig, J. D. E. Creighton, T. D. Creighton, A. Cumming, L. Cunningham, K. Dahl, M. Damjanic, S. L. Danilishin, K. Danzmann, B. Daudert, H. Daveloza, G. S. Davies, E. J. Daw, T. Dayanga, E. Deleeuw, T. Denker, T. Dent, V. Dergachev, R. DeRosa, R. DeSalvo, S. Dhurandhar, I. Di Palma, M. Díaz, A. Dietz, F. Donovan, K. L. Dooley, S. Doravari, S. Drasco, R. W. P. Drever, J. C. Driggers, Z. Du, J.-C. Dumas, S. Dwyer, T. Eberle, M. Edwards, A. Effler, P. Ehrens, S. S. Eikenberry, R. Engel, R. Essick, T. Etzel, K. Evans, M. Evans, T. Evans, M. Factourovich, S. Fairhurst, Q. Fang, B. F. Farr, W. Farr, M. Favata, D. Fazi, H. Fehrmann, D. Feldbaum, L. S. Finn, R. P. Fisher, S. Foley, E. Forsi, N. Fotopoulos, M. Frede, M. A. Frei, Z. Frei, A. Freise, R. Frey, T. T. Fricke, D. Friedrich, P. Fritschel, V. V. Frolov, M.-K. Fujimoto, P. J. Fulda, M. Fyffe, J. Gair, J. Garcia, N. Gehrels, G. Gelencser, L. Á. Gergely, S. Ghosh, J. A. Giaime, S. Giampanis, K. D. Giardina, S. Gil-Casanova, C. Gill, J. Gleason, E. Goetz, G. González, N. Gordon, M. L. Gorodetsky, S. Gossan, S. Goßler, C. Graef, P. B. Graff, A. Grant, S. Gras, C. Gray, R. J. S. Greenhalgh, A. M. Gretarsson, C. Griffo, H. Grote, K. Grover, S. Grunewald, C. Guido, E. K. Gustafson, R. Gustafson, D. Hammer, G. Hammond, J. Hanks, C. Hanna, J. Hanson, K. Haris, J. Harms, G. M. Harry, I. W. Harry, E. D. Harstad, M. T. Hartman, K. Haughian, K. Hayama, J. Heefner, M. C. Heintze, M. A. Hendry, I. S. Heng, A. W. Heptonstall, M. Heurs, M. Hewitson, S. Hild, D. Hoak, K. A. Hodge, K. Holt, M. Holtrop, T. Hong, S. Hooper, J. Hough, E. J. Howell, V. Huang, E. A. Huerta, B. Hughey, S. H. Huttner, M. Huynh, T. Huynh-Dinh, D. R. Ingram, R. Inta, T. Isogai, A. Ivanov, B. R. Iyer, K. Izumi, M. Jacobson, E. James, H. Jang, Y. J. Jang, E. Jesse, W. W. Johnson, D. Jones, D. I. Jones, R. Jones, L. Ju, P. Kalmus, V. Kalogera, S. Kandhasamy, G. Kang, J. B. Kanner, R. Kasturi, E. Katsavounidis, W. Katzman, H. Kaufer, K. Kawabe, S. Kawamura, F. Kawazoe, D. Keitel, D. B. Kelley, W. Kells, D. G. Keppel, A. Khalaidovski, F. Y. Khalili, E. A. Khazanov, B. K. Kim, C. Kim, K. Kim, N. Kim, Y.-M. Kim, P. J. King, D. L. Kinzel, J. S. Kissel, S. Klimenko, J. Kline, K. Kokeyama, V. Kondrashov, S. Koranda, W. Z. Korth, D. Kozak, C. Kozameh, A. Kremin, V. Kringel, B. Krishnan, C. Kucharczyk, G. Kuehn, P. Kumar, R. Kumar, B. J. Kuper, R. Kurdyumov, P. Kwee, P. K. Lam, M. Landry, B. Lantz, P. D. Lasky, C. Lawrie, A. Lazzarini, A. Le Roux, P. Leaci, C.-H. Lee, H. K. Lee, H. M. Lee, J. Lee, J. R. Leong, B. Levine, V. Lhuillier, A. C. Lin, V. Litvine, Y. Liu, Z. Liu, N. A. Lockerbie, D. Lodhia, K. Loew, J. Logue, A. L. Lombardi, M. Lormand, J. Lough, M. Lubinski, H. Lück, A. P. Lundgren, J. Macarthur, E. Macdonald, B. Machenschalk, M. MacInnis, D. M. Macleod, F. Magaña-Sandoval, M. Mageswaran, K. Mailand, G. Manca, I. Mandel, V. Mandic, S. Márka, Z. Márka, A. S. Markosyan, E. Maros, I. W. Martin, R. M. Martin, D. Martinov, J. N. Marx, K. Mason, F. Matichard, L. Matone, R. A. Matzner, N. Mavalvala, G. May, G. Mazzolo, K. McAuley, R. McCarthy, D. E.

McClelland, S. C. McGuire, G. McIntyre, J. McIver, G. D. Meadors, M. Mehmet, T. Meier, A. Melatos, G. Mendell, R. A. Mercer, S. Meshkov, C. Messenger, M. S. Meyer, H. Miao, J. Miller, C. M. F. Mingarelli, S. Mitra, V. P. Mitrofanov, G. Mitselmakher, R. Mittleman, B. , *Enhanced sensitivity of the LIGO gravitational wave detector by using squeezed states of light*, *Nature Photonics* **7** (aug, 2013) 613–619.

[140] T. Ehara, N. Shibata, H. Ohta, T. Nukui, and T. Kazuno, *Contact Resistivity and Adhesion of Ni/AuGe/Ag/Au Ohmic Contact Directly to n-Type AlGaAs*, *Japanese Journal of Applied Physics* **34** (jun, 1995) 3051–3053.

[141] W. Y. Han, Y. Lu, H. S. Lee, M. W. Cole, L. M. Casas, A. DeAnni, K. A. Jones, and L. W. Yang, *Shallow ohmic contact to both n and p GaAs*, *Journal of Applied Physics* **74** (jul, 1993) 754–756.

[142] J. J. Finley, M. Skalitz, M. Arzberger, A. Zrenner, G. Böhm, and G. Abstreiter, *Electrical detection of optically induced charge storage in self-assembled InAs quantum dots*, *Applied Physics Letters* **73** (nov, 1998) 2618–2620.

[143] M. C. Löbl, I. Söllner, A. Javadi, T. Pregnolato, R. Schott, L. Midolo, A. V. Kuhlmann, S. Stobbe, A. D. Wieck, P. Lodahl, A. Ludwig, and R. J. Warburton, *Narrow optical linewidths and spin pumping on charge-tunable close-to-surface self-assembled quantum dots in an ultrathin diode*, *Physical Review B* **96** (oct, 2017) 165440.